

DESIGN, FABRICATION AND CHARACTERIZATION OF NOVEL METAMATERIALS
IN MICROWAVE AND TERAHERTZ REGIONS: MULTI-BAND,
FREQUENCY-TUNABLE AND MINIATURIZED STRUCTURES

A THESIS SUBMITTED TO
THE GRADUATE SCHOOL OF NATURAL AND APPLIED SCIENCES
OF
MIDDLE EAST TECHNICAL UNIVERSITY

BY

EVREN EKMEKÇİ

IN PARTIAL FULFILLMENT OF THE REQUIREMENTS
FOR
THE DEGREE OF DOCTOR OF PHILOSOPHY
IN
ELECTRICAL AND ELECTRONICS ENGINEERING

DECEMBER 2010

Approval of the thesis:

**DESIGN, FABRICATION AND CHARACTERIZATION OF NOVEL
METAMATERIALS IN MICROWAVE AND TERAHERTZ REGIONS: MULTI-BAND,
FREQUENCY-TUNABLE AND MINIATURIZED STRUCTURES**

submitted by **EVREN EKMEKÇİ** in partial fulfillment of the requirements for the degree of
**Doctor of Philosophy in Electrical and Electronics Engineering Department, Middle
East Technical University** by,

Prof. Dr. Canan Özgen _____
Dean, Graduate School of **Natural and Applied Sciences**

Prof. Dr. İsmet Erkmn _____
Head of Department, **Electrical and Electronics Engineering**

Prof. Dr. Gönül Turhan Sayan _____
Supervisor, **Electrical and Electronics Engineering Dept., METU**

Examining Committee Members:

Prof. Dr. Mustafa Kuzuoğlu _____
Electrical and Electronics Engineering Dept., METU

Prof. Dr. Gönül Turhan Sayan _____
Electrical and Electronics Engineering Dept., METU

Assist. Prof. Dr. Asım Egemen Yılmaz _____
Electronics Engineering Dept., Ankara University

Prof. Dr. Gülbin Dural _____
Electrical and Electronics Engineering Dept., METU

Prof. Dr. Özlem Aydın Çivi _____
Electrical and Electronics Engineering Dept., METU

Date: 22.12.2010

I hereby declare that all information in this document has been obtained and presented in accordance with academic rules and ethical conduct. I also declare that, as required by these rules and conduct, I have fully cited and referenced all material and results that are not original to this work.

Name, Last Name: EVREN EKMEKÇİ

Signature :

ABSTRACT

DESIGN, FABRICATION AND CHARACTERIZATION OF NOVEL METAMATERIALS IN MICROWAVE AND TERAHERTZ REGIONS: MULTI-BAND, FREQUENCY-TUNABLE AND MINIATURIZED STRUCTURES

Ekmekçi, Evren

Ph. D., Department of Electrical and Electronics Engineering

Supervisor : Prof. Dr. Gönül Turhan Sayan

December 2010, 133 pages

This dissertation is focused on the design, fabrication, and characterization of novel metamaterials in microwave and terahertz regions with the following outcomes:

A planar μ -negative metamaterial structure, called double-sided SRR (DSRR), is proposed in the first part of this study. DSRR combines the features of a conventional split ring resonator (SRR) and a broadside-coupled SRR (BC-SRR) to obtain much better miniaturization at microwave frequencies for a given physical cell size. In addition to DSRR, double-sided multiple SRR (DMSRR), double-sided spiral resonator (DSR), and double-sided U-spiral resonator (DUSR) have been shown to provide smaller electrical sizes than their single-sided versions under magnetic excitation.

In the second part of this dissertation, a novel multi-band tunable metamaterial topology, called micro-split SRR (MSSRR), is proposed. In addition to that, a novel magnetic resonator structure named single loop resonator (SLR) is suggested to provide two separate magnetic resonance frequencies in addition to an electric resonance in microwave region.

In the third part, two different frequency tunable metamaterial topologies called BC-SRR

and gap-to-gap SRR are designed, fabricated and characterized at terahertz frequencies with electrical excitation for the first time. In those designs, frequency tuning based on variations in near field coupling is obtained by in-plane horizontal or vertical displacements of the two SRR layers. The values of frequency shifts obtained for these tunable metamaterial structures are reported to be the highest values obtained in literature so far. Finally, in the last part of this dissertation, novel double-sided metamaterial based sensor topologies are suggested and their feasibility studies are presented.

Keywords: split ring resonator, frequency tunable metamaterials, multi-band metamaterials, electrically-small metamaterials, metamaterial based sensors

ÖZ

MİKRODALGA VE TERAHERTZ BÖLGESİ ÖZGÜN METAMALZEMELERİN TASARIMI, ÜRETİMİ VE KARAKTERİZASYONU: ÇOK-BANTLI, FREKANSI AYARLANABİLİR VE KÜÇÜLTÜLMÜŞ YAPILAR

Ekmekçi, Evren

Doktora, Elektrik ve Elektronik Mühendisliği Bölümü

Tez Yöneticisi : Prof. Dr. Gönül Turhan Sayan

Aralık 2010, 133 sayfa

Bu tez, mikrodalga ve terahertz bölgesinde çalışan özgün metamalzemelerin tasarımı, üretimi ve karakterizasyonu konularına yoğunlaşmış ve aşağıda sıralanan sonuçlar elde edilmiştir:

Bu çalışmanın ilk kısmında, çift taraflı ayırık halkalı rezonatör (ÇAHR) adı verilen düzlemsel bir μ -negatif metamalzeme yapısı önerilmiştir. Bu ÇAHR yapısı, alışılmış ayırık halkalı rezonatör (AHR) yapısı ve düzleme dik bağlanmış AHR (DB-AHR) yapılarının özelliklerini birleştirerek verilen bir fiziksel hücre boyutu için mikrodalga frekanslarında elektriksel olarak çok daha küçük yapıların tasarımını mümkün kılmaktadır. ÇAHR yapısına ek olarak, çift taraflı çoklu-halkalı AHR (ÇÇAHR), çift taraflı spiral rezonatör (ÇSR) ve çift taraflı U-spiral rezonatör (ÇUSR) yapılarının manyetik uyarım altında tek taraflı uyarlamalarına göre elektriksel olarak daha küçük oldukları gösterilmiştir.

Tezin ikinci kısmında, mikro-ayrıklı AHR (MAAHR) yapısı olarak adlandırılan çok bantlı frekansı ayarlanabilir özgün bir metamalzeme yapısı önerilmiştir. Ayrıca, tek döngülü rezonatör (TDR) olarak adlandırılan ve mikrodalga frekans bölgesinde iki ayrı manyetik rezonans frekansına ek olarak bir tane de elektriksel rezonans sergileyen özgün bir manyetik

metamalzeme yapısı sunulmuştur.

Tezin üçüncü kısmında, DB-AHR ve ayırık-ayrığa AHR olarak adlandırılan iki ayrı frekansı ayarlanabilir metamalzeme topolojisinin terahertz frekanslarında ve elektriksel uyarım altında tasarımı, üretimi ve karakterizasyonu yapılmıştır. Literatürde ilk kez önerilen bu tasarımlarda, yakın alan bağlaşmasındaki deęişimlere dayalı frekans ayarlaması paralel AHR düzlemleri arasındaki düşey ve yatay kaydırmalarla elde edilmiştir. Bu ayarlanabilir metamalzeme yapıları için elde edilen frekans kaydırmaları literatürde şimdiye kadar sunulan en yüksek deęerlerdir.

Tezin son kısmında ise, özgün çift taraflı metamalzeme bazlı algılayıcı topolojileri önerilmiş ve bunlara ait fizibilite çalışmaları sunulmuştur.

Anahtar Kelimeler: ayırık halkalı rezonatörler, frekansı ayarlanabilir metamalzemeler, çok-bantlı metamalzemeler, elektriksel küçük metamalzemeler, metamalzeme bazlı algılayıcılar

to my lovely wife Zeynep

ACKNOWLEDGMENTS

First, I would like to express my sincere gratitude to my supervisor, Prof. Dr. Gönül Turhan Sayan, for her guidance, patience and encouragement throughout my Ph.D. studies at METU. I greatly appreciate her share in every step taken in the development of the thesis.

I am also grateful to Assoc. Prof. Dr. Richard D. Averitt, for hosting me at Boston University for one year, and I deeply appreciate his guidance, invaluable comments and suggestions during my terahertz metamaterial studies.

I would also like to thank the members of my thesis committee, Prof. Dr. Mustafa Kuzuoğlu, Assist. Prof. Dr. Asım Egemen Yılmaz and my former thesis committee member Prof. Dr. Adnan Köksal for their support and suggestions which improved the quality of the thesis.

I am very grateful to Dr. İ. Yücel Özbek, who is my roommate, for his friendship, company and guidance, who made my times in the department enjoyable and worthy. He never hesitated to lend a hand whenever I needed.

I owe so much to my dear friend Dr. Kağan Topallı for his contributions to my thesis and also for his friendship. I enjoyed and learned too much while I am collaborating with him.

I also would like to thank to my dear friends Ahmet Hayrettin Yüzer, Oğuzhan Erdem, Umut Tilki, Sebahattin Topal, Yılmaz Kalkan, Barış Özyer, Akif Durdu, Dr. Tansu Filik, Atilla Dönük, Dr. Eren Akdemir, Dr. Emre Özkan, Turgay Koç for their support and friendship through these years.

I acknowledge TÜBİTAK for supporting me through Program 2214 during my Ph.D. studies in Boston University.

I also would like to thank to Andrew C. Strikwerda, Jingdi Zhang, Elsa Abreau, Kebin Fan, Mengkun Liu, Dr. Hu Tao, Mehmet S. Öztürk, Hüseyin Rahmi Seren, who are my fellows in Boston University, for their help and friendship.

I am also very grateful to my parents Cihangir Ekmekçi, Melek Ekmekçi and also to my sister

Dr. Dt. Ebru Ekmekçi for their sincere love and endless support during my life.

Lastly, but not the least, I am grateful to my dear wife Zeynep Ekmekçi. I could not have completed my thesis without her unlimited support and patience.

TABLE OF CONTENTS

ABSTRACT	iv
ÖZ	vi
ACKNOWLEDGMENTS	ix
TABLE OF CONTENTS	xi
LIST OF TABLES	xv
LIST OF FIGURES	xvi
CHAPTERS	
1 INTRODUCTION	1
1.1 Metamaterial Research Topics Studied in This Dissertation	2
1.1.1 Split Ring Resonators	2
1.1.2 Miniaturized Metamaterials	3
1.1.3 Circuit Modeling of Resonator Structures	4
1.1.4 Frequency Tunable Metamaterials	5
1.1.5 Terahertz Region Metamaterials	5
1.2 Novel Contributions of This Dissertation to Literature on Metamaterials	6
1.3 Organization of This Dissertation	7
2 THEORY OF METAMATERIALS	10
2.1 Characteristics of Metamaterials with Simultaneously Negative Values of Permittivity and Permeability	10
2.2 Methods of Obtaining Negative Permittivity, Negative Permeability and a Left-Handed Metamaterial	13
2.2.1 Negative Permittivity	14
2.2.1.1 Obtaining Negative Permittivity Using Thin Wire Arrays	14

	2.2.1.2	Obtaining Negative Permittivity with Special Resonator Structures	16
	2.2.2	Negative Permeability	17
	2.2.3	Realization of Left-Handed Metamaterials	18
2.3		Excitation Techniques for Metamaterial Resonator Structures	19
2.4		Describing an Effective Metamaterial Medium	20
2.5		Simulation Techniques and Boundary Conditions	21
3		NOVEL DOUBLE-SIDED TOPOLOGIES FOR ELECTRICALLY-SMALL, MAGNETIC RESONATOR TYPE METAMATERIALS	26
	3.1	Introduction	26
	3.2	Description of the Resonator Topologies, Structural Parameters and the Simulation Setup	27
	3.2.1	Definition of the Geometry, Simulation Setup and the Equivalent Circuit Model	27
	3.2.2	Equivalent Circuit Models	30
	3.3	Simulation of the Resonance Behaviors for the SRR, BC-SRR, and DSRR Type Metamaterial Structures	33
	3.3.1	Effects of the Substrate Thickness (d) on Resonance Parameters	33
	3.3.1.1	Variation of the Resonance Frequency (f_0) with Substrate Thickness d :	35
	3.3.1.2	Variation of the Half-Power Bandwidth ($HPBW$) with Substrate Thickness d :	37
	3.3.1.3	Variation of the Transmission Minimum (T_{min}) with Substrate Thickness d :	37
	3.3.2	Effects of the Relative Permittivity (ϵ_r) of the Substrate on Resonance Parameters	38
	3.3.2.1	Variation of the Resonance Frequency (f_0) with the Relative Permittivity ϵ_r of the Substrate:	41
	3.3.2.2	Variation of the Resonance Bandwidth ($HPBW$) with the Relative Permittivity ϵ_r of the Substrate:	41
	3.3.2.3	Variation of the Transmission Minimum (T_{min}) with the Relative Permittivity ϵ_r of the Substrate:	42
	3.3.3	Effects of the Loss Tangent ($\tan \delta_c$) of the Substrate on Resonance Parameters	42

3.4	Comparison of the Electrical Sizes of the SRR, BC-SRR, and DSRR Unit Cells	42
3.5	Verification of the Equivalent Circuit Model for DSRR	44
3.6	A Left Handed Medium with DSRR Structure	46
3.6.1	Extraction of Effective Medium Parameters	47
3.7	Alternative Topologies for Electrically-Small Magnetic Resonator Type Metamaterial Design	51
3.7.1	Design and Simulations	52
3.7.2	Results and Discussions	54
4	NOVEL TUNABLE AND MULTI-BAND METAMATERIAL DESIGNS . .	58
4.1	Introduction	58
4.2	A Tunable Multi-Band Metamaterial Design Using Micro-Split SRR Arrays	60
4.2.1	Design	60
4.2.2	Fabrication	61
4.2.3	Simulations and Experiments	63
4.2.3.1	Simulations	63
4.2.3.2	Experiments	64
4.2.4	Results	64
4.2.4.1	Single Layer Homogeneous SRR and MSSRR Arrays	65
4.2.4.2	Dual-Layer Homogeneous Super Cell Arrays of SRRs or MSSRRs	68
4.2.4.3	Double-Layer and Triple-Layer Inhomogeneous Super Cell Arrays of SRRs and MSSRRs . . .	68
4.2.4.4	Switching for Adaptive Tuning of Multi-Band Operation	70
4.2.5	An Alternative Triple-Band Metamaterial Design with Smaller Electrical Size	71
4.3	Single Loop Resonator: A Novel Dual-Band Magnetic Metamaterial Structure	72
4.3.1	Design and Simulations	74
4.3.2	Results	75

5	FREQUENCY-TUNABLE METAMATERIALS USING BROADSIDE COUPLED AND GAP TO GAP ORIENTED SPLIT RING RESONATORS: DESIGN, FABRICATION AND CHARACTERIZATION IN TERAHERTZ REGION	79
5.1	Introduction	79
5.2	Design, Fabrication, and Characterization	81
5.2.1	Design	81
5.2.2	Fabrication	82
5.2.3	Characterization	82
5.3	Effective Medium Parameters	83
5.3.1	Extraction of Effective Medium Parameters	84
5.3.2	An Approach For the Verification of Effective Medium Parameters	85
5.4	Results	86
5.5	Discussion	96
6	METAMATERIAL SENSOR APPLICATIONS USING BROADSIDE-COUPLED SRR AND V-SHAPED RESONATOR STRUCTURES	102
6.1	Introduction	102
6.2	BC-SRR Based Metamaterial Sensor Applications	103
6.2.1	Behavior of the Ordinary BC-SRR Structure Under Magnetic and Electric Excitation	103
6.2.2	Electromagnetic Response of BC-SRR Under Magnetic and Electric Excitation	106
6.2.3	BC-SRR Based Sensor Model	107
6.2.4	BC-SRR Based Sensor for Microwave Region Using Magnetic Excitation	108
6.2.5	BC-SRR Based Sensor for Terahertz Region Using Electric Excitation	110
6.3	A V-Shaped Resonator Based Pressure Sensor Application	110
6.4	Discussion	112
7	CONCLUSION AND FUTURE WORKS	114
	REFERENCES	118
	VITA	129

LIST OF TABLES

TABLES

Table 3.1	Resonance frequencies for the DSRR topology obtained from the HFSS simulations and from the equivalent circuit model for different values of relative substrate thickness (d) where $\epsilon_r = 4.4$ mm and $\tan \delta_c = 0.020$	45
Table 3.2	Resonance frequencies for the DSRR topology obtained from the HFSS simulations and from the equivalent circuit model for different values of relative substrate permittivity (ϵ_r) where $d = 1.52$ mm and $\tan \delta_c = 0.020$	47
Table 3.3	Resonance frequency and electrical size for N -ring MSRR topologies.	54
Table 3.4	Resonance frequency and electrical size for N -ring SR topologies.	54
Table 3.5	Resonance frequency and electrical size values for N -ring MSRR and Double-Sided MSRR (DMSRR) Topologies.	56
Table 3.6	Resonance frequency and electrical size values for the N -ring SR, USR topologies and their double-sided versions, DSR and DUSR topologies.	56

LIST OF FIGURES

FIGURES

Figure 1.1 Common split ring resonator (SRR) structures: (a) Conventional circular SRR, (b) single-ring SRR, (c) square-shape single ring SRR, (d) single ring SRR with two gaps, (e) single ring SRR with four gaps, (f) extended gap SRR.	3
Figure 2.1 Directions of vector \vec{S} , \vec{k} , \vec{E} , and \vec{H}	12
Figure 2.2 Passage of a ray through the boundary between mediums 1 and 2. 1) incident ray, 2) reflected ray, 3) refracted ray in the second medium is left handed, 4) refracted ray in the second medium is right handed.	13
Figure 2.3 μ vs ϵ chart.	14
Figure 2.4 A periodic thin wire array used to obtain negative values of effective permittivity.	15
Figure 2.5 A typical permittivity vs frequency plot with plasma frequency $\omega_p = 10 \times 10^9$ rad/sec based on plasma theory. $a = 23.7 \times 10^{-3}$ m and $r = 1 \times 10^{-6}$ m	16
Figure 2.6 Schematic views of the split ring resonator (SRR) and the electric field coupled (ELC) resonator structures.	17
Figure 2.7 Schematic views of the split ring resonator (SRR), the spiral resonator (SR), the U-shaped resonator (USR) structure, and the labyrinth resonator structure.	18
Figure 2.8 A composite left-handed medium. (a) Front and (b) back view.	19
Figure 2.9 Excitation techniques for the SRR structure. (a) Only magnetic excitation. (b) Electric and magnetic excitation. (c) Only electric excitation. (d) No excitation.	20
Figure 2.10 SRR array and the free-space wavelength at resonance frequency.	21
Figure 2.11 Implementation of perfect electric conductor (PEC) and perfect magnetic conductor (PMC) boundary condition pairs under normal incidence.	23

Figure 2.12 Implementation of periodic boundary conditions (PBC) under normal incidence.	24
Figure 3.1 Unit cell geometries for the SRR, BC-SRR, and DSRR type metamaterials and the excitation.	28
Figure 3.2 Resonance parameters (i.e. f_0 , $HPBW$, and T_{min}) defined on the transmission versus frequency curve.	29
Figure 3.3 Setup for HFSS simulations.	30
Figure 3.4 The conventional SRR topology together with its symmetry line and its basic equivalent circuit model.	31
Figure 3.5 A simple equivalent circuit model proposed for the DSRR unit cell.	31
Figure 3.6 Transmission spectra of the SRR, BC-SRR, and DSRR structures for different substrate thicknesses using $L = 5$ mm, $l = 4$ mm, $h = 3$ mm, $g = 0.5$ mm, $w = 0.3$ mm, $s = 0.5$ mm, $\epsilon_r = 4.4$ and $\tan \delta_c = 0.020$	34
Figure 3.7 Variation of the resonance frequency (f_0) and electrical size (u) with substrate thickness (d) for the SRR, BC-SRR, and DSRR structures using $L = 5$ mm, $l = 4$ mm, $h = 3$ mm, $g = 0.5$ mm, $w = 0.3$ mm, $s = 0.5$ mm, $\epsilon_r = 4.4$ and $\tan \delta_c = 0.020$	36
Figure 3.8 Variation of the resonance bandwidth ($HPBW$) with substrate thickness (d) for the SRR, BC-SRR, and DSRR structures using $L = 5$ mm, $l = 4$ mm, $h = 3$ mm, $g = 0.5$ mm, $w = 0.3$ mm, $s = 0.5$ mm, $\epsilon_r = 4.4$ and $\tan \delta_c = 0.020$	36
Figure 3.9 Variation of the transmission minimum (T_{min}) with substrate thickness (d) for the SRR, BC-SRR, and DSRR unit cells using $L = 5$ mm, $l = 4$ mm, $h = 3$ mm, $g = 0.5$ mm, $w = 0.3$ mm, $s = 0.5$ mm, $\epsilon_r = 4.4$ and $\tan \delta_c = 0.020$	38
Figure 3.10 Transmission spectra of the SRR, BC-SRR, and DSRR structures for different substrate permittivity values using $L = 5$ mm, $l = 4$ mm, $h = 3$ mm, $g = 0.5$ mm, $w = 0.3$ mm, $s = 0.5$ mm, $d = 1.52$ and $\tan \delta_c = 0.020$	39
Figure 3.11 Variation of the resonance frequency (f_0) and electrical size (u) with relative substrate permittivity (ϵ_r) for the SRR, BC-SRR, and DSRR structures using $L = 5$ mm, $l = 4$ mm, $h = 3$ mm, $g = 0.5$ mm, $w = 0.3$ mm, $d = 1.52$ mm and $\tan \delta_c = 0.020$	40

Figure 3.12 Variation of the resonance bandwidth (<i>HPBW</i>) with relative substrate permittivity (ϵ_r) for the SRR, BC-SRR, and DSRR structures using $L = 5$ mm, $l = 4$ mm, $h = 3$ mm, $g = 0.5$ mm, $w = 0.3$ mm, $d = 1.52$ mm and $\tan \delta_c = 0.020$	40
Figure 3.13 Variation of the transmission minimum (T_{min}) with relative substrate permittivity (ϵ_r) for the SRR, BC-SRR, and DSRR structures using $L = 5$ mm, $l = 4$ mm, $h = 3$ mm, $g = 0.5$ mm, $w = 0.3$ mm, $d = 1.52$ mm and $\tan \delta_c = 0.020$	41
Figure 3.14 Transmission spectra of the SRR, BC-SRR, and DSRR structures for different loss tangent values of substrate using $L = 5$ mm, $l = 4$ mm, $h = 3$ mm, $g = 0.5$ mm, $w = 0.3$ mm, $s = 0.5$ mm, $\epsilon_r = 4.4$ and $d = 1.52$ mm.	43
Figure 3.15 Resonance frequencies obtained from HFSS simulations and from the equivalent circuit model for different substrate thicknesses where $\epsilon_r = 4.4$ and $\tan \delta_c = 0.020$	46
Figure 3.16 Resonance frequencies obtained from HFSS simulations and from the equivalent circuit model for different values of substrate relative permittivity where $d = 1.52$ mm and $\tan \delta_c = 0.020$	46
Figure 3.17 Left-handed unit-cell composed of a DSRR and a conducting strip.	48
Figure 3.18 Complex effective medium parameters of the structure given in Figure 3.17. $\epsilon_{eff} = \epsilon'_{eff} - \epsilon''_{eff}$ and $\mu_{eff} = \mu'_{eff} - \mu''_{eff}$ using $e^{j\omega t}$ time dependence.	48
Figure 3.19 Top views of single- and double-sided structures with $N = 6$	53
Figure 3.20 Directions of vector fields on the DSR structure.	53
Figure 3.21 Resonance frequency and electrical size for N -ring MSRR topologies.	55
Figure 3.22 Resonance frequency and electrical size for N -ring SR topologies.	55
Figure 3.23 Resonance frequency and electrical size values for N -ring MSRR and Double-Sided MSRR (DMSRR) Topologies.	56
Figure 3.24 Resonance frequency and electrical size values for the N -ring SR, USR topologies and their double-sided versions, DSR and DUSR topologies.	57
Figure 4.1 Schematic views of (a) unit cell A, (b) unit cell B, (c) unit cell C	61
Figure 4.2 Wafer mask layout for fabrication.	62
Figure 4.3 Dicing instructions for main pieces.	62
Figure 4.4 Dicing instructions for sub-pieces.	63

Figure 4.5 (a) Schematic of simulation and experimental setup, (photograph of experimental setup.)	64
Figure 4.6 Agilent 8720D vector network analyzer	65
Figure 4.7 (a) Transmission characteristics of the type A SRR array. (b) Photograph of the actual resonator's unit cell.	66
Figure 4.8 (a) Transmission characteristics of the type B MSSRR array. (b) Photograph of the actual resonator's unit cell.	66
Figure 4.9 (a) Transmission characteristics of the type C MSSRR array. (b) Photograph of the actual resonator's unit cell.	66
Figure 4.10 (a) Transmission characteristics of the resonator array composed of 2×2 super cells having type A unit cells. (b) Photograph of the actual resonator's super cell.	67
Figure 4.11 (a) Transmission characteristics of the resonator array composed of 2×2 super cells having type B unit cells. (b) Photograph of the actual resonator's super cell.	67
Figure 4.12 (a) Transmission characteristics of the resonator array composed of 2×2 super cells having type C unit cells. (b) Photograph of the actual resonator's super cell.	67
Figure 4.13 (a) Transmission characteristics of the dual band resonator array composed of 2×2 inhomogeneous super cells having type A (in column 2) and type B (in column 1) unit cells. (b) Photograph of the actual resonator's super cell.	69
Figure 4.14 (a) Transmission characteristics of the dual band resonator array composed of 2×2 inhomogeneous super cells having type A (in column 2) and type B in (column 1) unit cells. (b) Photograph of the actual resonator's super cell.	69
Figure 4.15 (a) Transmission characteristics of the triple-band resonator array of 3×2 inhomogeneous super cells having type A (in column 1), type B (in column 2) and type C (in column 3) unit cells. (b) Photograph of the actual resonator's super cell.	70
Figure 4.16 Schematic view of the switching representation for type C resonator.	71
Figure 4.17 Schematic representation and dimensions for the alternative electrically small composite unit cell providing three-band operation.	73

Figure 4.18 Transmission and reflection characteristics for the composite cell shown in Figure 4.17. (a) Magnitude plots, (b) phase plots.	73
Figure 4.19 Effective medium parameters for the metamaterial resonator array composed of the composite cell shown in Figure 4.17 using $e^{j\omega t}$ time dependence. (a) Complex effective permittivity $\epsilon_{eff} = \epsilon'_{eff} - \epsilon''_{eff}$, (b) complex effective permeability $\mu_{eff} = \mu'_{eff} - \mu''_{eff}$	74
Figure 4.20 Schematic view of Single Loop Resonator unit cell	74
Figure 4.21 Simulation setup	75
Figure 4.22 Transmission and reflection characteristics of the SLR array.	76
Figure 4.23 Current distribution on the SLR unit cell at each resonance frequency. (a) At 7.72 GHz, (b) at 8.60 GHz, (c) at 9.86 GHz.	77
Figure 4.24 Complex effective medium parameters of the SLR structure. $\mu_{eff} = \mu'_{eff} - \mu''_{eff}$ and $\epsilon_{eff} = \epsilon'_{eff} - \epsilon''_{eff}$ using $e^{j\omega t}$ time dependence.	78
Figure 5.1 Schematic views of (a) BC-SRR and (b) gap-to-gap oriented structures. . .	81
Figure 5.2 Schematic view, dimensions, and excitation for a single SRR, which forms BC-SRR or gap-to-gap oriented structure. $P = 58 \mu\text{m}$, $l = 40 \mu\text{m}$, $w = 11 \mu\text{m}$, $g = 5 \mu\text{m}$, substrate thickness (t_{sub}) = $5 \mu\text{m}$, and superstrate thickness (t_{super}) = $5 \mu\text{m}$. (a) Top view. (b) Transparent perspective view for the BC-SRR case with no-shift.	82
Figure 5.3 A photograph of the fabricated metamaterial arrays.	83
Figure 5.4 THz-TDS setup for metamaterial experimental characterization.	84
Figure 5.5 Flow chart for the verification of effective medium parameters.	86
Figure 5.6 Optical microscope pictures of BC-SRR structures shifted along vertical direction for $0 \mu\text{m}$ (no-shift), $5 \mu\text{m}$, $10 \mu\text{m}$, $15 \mu\text{m}$, $20 \mu\text{m}$, $25 \mu\text{m}$, and $30 \mu\text{m}$. . .	87
Figure 5.7 Transmission magnitudes vs frequency of BC-SRR structures shifted along vertical direction for $0 \mu\text{m}$, $5 \mu\text{m}$, $10 \mu\text{m}$, $15 \mu\text{m}$, $20 \mu\text{m}$, $25 \mu\text{m}$, and $30 \mu\text{m}$. (a) Simulation and (b) experimental results.	87
Figure 5.8 Effective permittivity ϵ_{eff} and effective permeability μ_{eff} graphs of BC-SRR structure shifted along vertical direction for $0 \mu\text{m}$, $10 \mu\text{m}$, $20 \mu\text{m}$, and $30 \mu\text{m}$	89

Figure 5.9 Effective average permittivity ϵ_{av} and effective average permeability μ_{eff} graphs of BC-SRR structure shifted along vertical direction for 20 μm and 30 μm as the demonstrations of the anti-resonant effects removal.	90
Figure 5.10 Extracted and fitted effective permittivity values of vertically shifted BC-SRR structure for μm , 10 μm , 20 μm , and 30 μm shifts. (a) Real and (b) imaginary parts.	90
Figure 5.11 Verification of effective medium parameters for vertically shifted BC-SRR structure. (a) Experimental transmission characteristics. (b) Transmission characteristics obtained through fitted effective medium parameters.	91
Figure 5.12 Optical microscope pictures of BC-SRR structures shifted along horizontal direction for 0 μm (no-shift), 5 μm , 10 μm , 15 μm , 20 μm , 25 μm , and 30 μm	92
Figure 5.13 Transmission magnitudes vs frequency of BC-SRR structures shifted along horizontal direction for 0 μm , 5 μm , 10 μm , 15 μm , 20 μm , 25 μm , and 30 μm . (a) Simulation and (b) experimental results.	92
Figure 5.14 Effective permittivity ϵ_{eff} and effective permeability μ_{eff} graphs of BC-SRR structure shifted along horizontal direction for 0 μm , 10 μm , 20 μm , and 30 μm	93
Figure 5.15 Extracted and fitted effective permittivity values of vertically shifted BC-SRR structure for μm , 10 μm , 20 μm , and 30 μm shifts. (a) Real and (b) imaginary parts.	94
Figure 5.16 Verification of effective medium parameters for horizontally shifted BC-SRR structure. (a) Experimental transmission characteristics. (b) Transmission characteristics obtained through fitted effective medium parameters.	95
Figure 5.17 Optical microscope pictures of some specific gap-to-gap oriented structures shifted along vertical direction for 0 μm (no-shift), 5 μm , 10 μm , 15 μm , 20 μm , 25 μm , and 30 μm	95
Figure 5.18 Transmission magnitudes vs frequency for gap-to-gap oriented structures shifted along vertical direction for 0 μm , 5 μm , 10 μm , 15 μm , 20 μm , 25 μm , and 30 μm . (a) Simulation and (b) experimental results.	96

Figure 5.19 Effective permittivity ϵ_{eff} and effective permeability μ_{eff} graphs of gap-to-gap SRR structure shifted along vertical direction for $0 \mu\text{m}$, $10 \mu\text{m}$, $20 \mu\text{m}$, and $30 \mu\text{m}$	97
Figure 5.20 Extracted and fitted effective permittivity values of vertically shifted gap-to-gap oriented SRR structure for μm , $10 \mu\text{m}$, $20 \mu\text{m}$, and $30 \mu\text{m}$ shifts. (a) Real and (b) imaginary parts.	98
Figure 5.21 Verification of effective medium parameters for horizontally shifted BC-SRR structure. (a) Experimental transmission characteristics. (b) Transmission characteristics obtained through fitted effective medium parameters.	98
Figure 5.22 Schematic views of the surface charge distributions and their associated surface current distributions for (a) BC-SRR and (b) gap-to-gap oriented SRR structures.	99
Figure 5.23 (a) Optical microscope picture of fabricated BC-SRR structure horizontally shifted for $5 \mu\text{m}$. (b) Schematic view of BC-SRR structure horizontally shifted in opposite direction for $5 \mu\text{m}$. (c) Simulation results for BC-SRR structures horizontally shifted in opposite direction for $0 \mu\text{m}$, $5 \mu\text{m}$, $10 \mu\text{m}$, $15 \mu\text{m}$, $20 \mu\text{m}$, $25 \mu\text{m}$, and $30 \mu\text{m}$	101
Figure 6.1 Schematic views of BC-SRR structure. (a) Top view with design parameters. (b) Magnetic excitation. (c) Electric excitation.	104
Figure 6.2 Effects of substrate thickness t_{sub} on the resonance frequency of BC-SRR under (a) magnetic and (b) electric excitations.	105
Figure 6.3 Effects of relative permittivity of substrate ϵ_r on the resonance frequency of BC-SRR under (a) magnetic and (b) electric excitations.	106
Figure 6.4 Schematic views of the surface charge distributions and their corresponding surface current distributions for (a) magnetically and (b) electrically excited BC-SRR structures. The top and bottom layers are shown displaced for clarity.	107
Figure 6.5 Schematic view of BC-SRR based sensor. (a) Perspective view and the directions of the vector fields for magnetic and electric excitations. (b) Side view.	108
Figure 6.6 Effects of the interlayer thickness (d_i) and permittivity (ϵ_{int}) on the resonance frequency of BC-SRR based metamaterial sensor under magnetic excitation in microwave region.	109

Figure 6.7 Effects of the interlayer thickness (d_i) and permittivity (ϵ_{int}) on the resonance frequency of BC-SRR based metamaterial sensor under electric excitation in terahertz region.	111
Figure 6.8 Schematic representation for the mechanism of V-shaped resonator based sensor application.	111
Figure 6.9 Design parameters of the V-shaped unit cell structure.	112
Figure 6.10 Transmission spectra of the V-sensor for different shift values.	113
Figure 6.11 V-Sensor topologies for different lateral shift amounts.	113

CHAPTER 1

INTRODUCTION

In 1968, Veselago's proposal of an artificial medium having simultaneously negative values of permittivity (ϵ) and permeability (μ) was the starting point for the research on left-handed metamaterials [1]. It was claimed that unlike the ordinary (i.e. right-handed) materials, wave vector \vec{k} , electric field vector \vec{E} , and magnetic field vector \vec{H} of such materials would form a left-handed triplet, hence they were called "left-handed" materials. Besides, a left-handed medium was expected to exhibit some extra-ordinary properties which were not observed in naturally existing materials. These were backward propagation, reverse Doppler effect, reverse Vavilov-Cerenkov effect and negative index of refraction [1]. Possibility of designing artificial materials with such unique properties was very exciting. However, the problem was the realization. In fact, realization of ϵ -negative (ENG) media was known to be possible by using the thin-wire array structures, based on the plasma theory [2, 3]. Therefore, the limiting issue was the realization of μ -negative (MNG) media. Due to the lack of free magnetic charges in the nature, the use of plasma-like behavior was not possible to obtain MNG regions. Fortunately, in 1999, Pendry et al. broke the peace and they proposed the use of Swiss rolls or split ring resonator (SRR) structures to obtain MNG spectrum [4]. As the follow-up, Smith et al. proposed the use of a composite medium consisting of periodic SRR arrays and thin-wire structures, to obtain simultaneously negative values of ϵ and μ [5]. In 2001 finally the dream came true when, Shelby et al. demonstrated the first physical left-handed medium (LHM) [6]. This realization was the starting point of so many new frontiers in metamaterial applications, within the last decade.

The number of metamaterial related journal papers, which have been indexed by ISI Web of Knowledge since 2000, is over 2200. It looks that there has been an almost exponential increase in the number of published metamaterial work over the last decade. There are var-

ious research topics related to the theory and applications of metamaterial structures. The most popular of those are the investigation of fundamental properties of the negative index metamaterials [7, 8, 9, 10], designing miniaturized (i.e. electrically small) metamaterials [11, 12, 13, 14, 15, 16, 17, 18], circuit modeling for metamaterials [12, 13, 14, 19, 20, 21, 22], frequency tunable metamaterials [23, 24, 25, 26, 27, 28, 29, 30], investigation of anisotropy and bianisotropy in metamaterial structures [11, 31, 32, 33, 34], extraction of effective medium parameters [35, 36, 37, 38, 39, 40], coordinate transformations/invisibility cloaks [41, 42, 43, 44, 45, 46, 47], imaging / perfect lens designs [10, 48, 49, 50, 51, 52, 53], use of metamaterials in the design of antennas [54, 55, 56], and transmission line models of metamaterials [49, 57, 58, 59].

1.1 Metamaterial Research Topics Studied in This Dissertation

In the following sub-sections, the research topics studied within the context of this dissertation will be briefly introduced.

1.1.1 Split Ring Resonators

Split ring resonator (SRR) is one of the most common metamaterial resonator structures reported in literature. The schematic view of the conventional SRR and its well-known variants are given in Figure 1.1. When a time-varying magnetic field \vec{H} applied perpendicularly to the SRR plane, a MNG region is provided around its resonance frequency [4]. SRR also promises ENG regions, when it is excited electrically [60, 61]. This type of excitation is commonly preferred by the terahertz (THz) metamaterial community due to the difficulties in performing experiments by using magnetic excitation. Detailed information on the excitation types of SRR structure will be given in Section 2.3.

Effects of fundamental SRR design parameters (i.e. unit cell size, width of the metal strips and gap, separation distance between the neighboring rings, etc.) on the resonance frequency of the structure were thoroughly studied in literature [13, 31, 62, 63, 64, 65, 66]. In 2002, electromagnetic polarizabilities of the conventional SRR were investigated by Marqués et al. to figure out its bianisotropic behavior. Since bianisotropy is not a desired feature for many

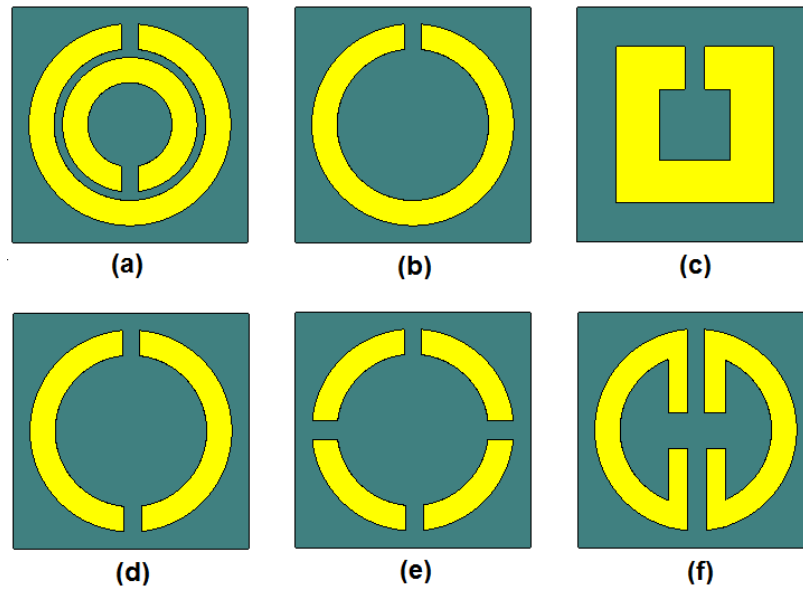


Figure 1.1: Common split ring resonator (SRR) structures: (a) Conventional circular SRR, (b) single-ring SRR, (c) square-shape single ring SRR, (d) single ring SRR with two gaps, (e) single ring SRR with four gaps, (f) extended gap SRR.

applications, an alternative double-sided SRR topology called BC-SRR was also proposed to avoid bianisotropic behavior [11, 31].

Magnetic metamaterial designs different than the conventional SRR and BC-SRR have also been proposed in literature. They are; spiral resonators (SR) [14, 16], V-shaped resonators [67], labyrinth resonators [68, 69], S-shaped resonator [70, 71, 72], Ω -shaped resonator [72, 73], single loop resonator (SLR) [74] and double-sided SR (DSR) [16, 75], broadside-coupled SR (BC-SR) [17, 18], double-sided SRR (DSRR) [13, 64, 76].

1.1.2 Miniaturized Metamaterials

The theory of metamaterials is based on the effective medium approach [11, 31] that assumes the presence of an approximately homogeneous medium which consist of unit cells whose physical dimensions are much smaller than the free space wavelength. In other words, smaller the electrical size of the unit cells, better the homogenization will be. Thus, the studies on miniaturized (i.e. electrically-small) metamaterials become very important.

The typical electrical size of an SRR is about one tenth of the free space wavelength [11, 31].

Moreover, it has been demonstrated that the BC-SRR, multiple SRR (MSRR) and DSRR structures have the advantage of being electrically smaller as compared to the conventional SRR structure [11, 12, 13, 20, 31]. Among all of these *SRR based* topologies, double-sided MSRR (DMSRR) has promised the best miniaturization results [13].

Conventional spiral resonator (SR) topology and its variants, double-sided SR (DSR), broadside-coupled SR (BC-SR), U-spiral resonator (USR) and double-sided USR (DUSR) have been shown to have much smaller electrical sizes as compared to the conventional SRR topology [12, 14, 15, 16, 17, 18].

Moreover, Aznar et al. showed that electrical sizes of the metamaterial resonator structures could be reduced by combining spiral topologies together with the broadside coupled topologies [17]. Based on this idea, some novel BC-SR structures was introduced by using two resonator layers connected each other by conducting vias [18]. It was also shown in [18] that the resonance frequency hence the electrical size can be significantly reduced for smaller values of the substrate thickness in either SR topology or in BC-SR topology.

1.1.3 Circuit Modeling of Resonator Structures

The characteristics of complicated metamaterial structures can be investigated accurately and efficiently with the use of commercial full-wave electromagnetic solvers such as Ansoft HFSS and CST Microwave Studio. However, the use of proper equivalent circuit models for metamaterial structures would certainly simplify the analysis and design studies with an appreciable savings on computational time and memory requirements. In 2004 and 2005, an equivalent circuit model for the SRR unit cell was proposed and validated where the small capacitive effects coming from splits and also the effects of dielectric losses were neglected [14, 19]. In 2006, an equivalent circuit model for the three-dimensional array composed of magnetically excited ring structures was presented [77]. In that study, the coupling effects between individual columns of rings were included in the model. Recently, the effects of dielectric and conductor losses were demonstrated in the equivalent circuit models proposed by Bilotti et al. for multiple SRRs (MSRRs), SRs, and labyrinth type resonators [12, 20]. In addition, a symmetrical circuit model describing all kinds of circuit metamaterials was suggested by Cui et al. [21]. In 2009 Ekmekci et al. proposed an approximate circuit model for the BC-SRR and double-sided SRR (DSRR) structures [13]. Also in 2010, an equivalent circuit model for

SRR arrays was given by Yasar-Orten et al. [22].

1.1.4 Frequency Tunable Metamaterials

Left-handed metamaterials are commonly constructed by a combined use of thin wire arrays and magnetic resonator arrays [6]. The frequency bandwidth of MNG operation provided by magnetic resonator arrays is usually a small fraction of the ENG region bandwidth provided by periodic thin wire arrays. Therefore, tuning the left-handed operation bandwidth of the composite material essentially requires the tuning of the resonance frequency of the magnetic resonator array.

In literature, there are various approaches reported for tuning the resonance frequency of magnetic resonators. A common approach is to change the design parameters of the metallic inclusions (i.e. metal strip width, separation between the rings, gap widths, unit cell dimension, etc.) [63] or to play with the thickness and dielectric constant of the substrate [13, 78]. Obviously, it is not possible to change the geometrical parameters of an already printed metallic inclusion or the parameters of the substrate. Instead, some sophisticated techniques needed to be used for real-time tuning. The use of liquid crystals [25, 79, 80, 81, 82], lumped capacitors or varactors [26, 83, 84, 85, 86, 87], ferromagnetic [27, 88, 89, 90] and ferroelectric [91, 92] techniques, semiconductors [29, 30, 93, 94], and microelectromechanical (MEMS) switches [16, 23, 28, 95, 96] have been suggested in literature for tuning metamaterial devices in various applications.

1.1.5 Terahertz Region Metamaterials

Terahertz (THz) region of the electromagnetic spectrum extends from 300 GHz to 3 THz ($1 \text{ THz} = 10^{12} \text{ Hz}$) which is alternatively called the far-infrared region (FIR). While operation of electromagnetic devices are described by the principles of RF electronics in microwave region or at lower frequencies, most of the devices operating in the infrared region and beyond are photon-based devices. The THz gap is considered to be a transition region between the areas of electronics and photonics [97, 98, 99].

The metamaterial structures are frequency scalable, thus they can be easily scaled from microwave to THz region. However, in usual THz time domain spectroscopy (THz-TDS) setups,

the electromagnetic waves are sent with normal incidence onto the SRR plane. In this case, the magnetic field vector \vec{H} lies parallel to the SRR plane, and hence the magnetic excitation is not possible [99]. In other words, metamaterial resonators are usually excited electrically in terahertz region although there are rare examples in literature which report the magnetic excitation of THz metamaterials with the use of some sophisticated experimental techniques. In THz region, the most common THz region metamaterial structures are the single ring SRR and the electric field coupled (ELC) resonator [100, 101, 102]. More information about these resonator structures will be presented in Section 2.2.1.2.

1.2 Novel Contributions of This Dissertation to Literature on Metamaterials

Three international journal papers [13, 23, 74], eight international conference papers [16, 66, 67, 64, 103, 104, 105, 106], and six national conference papers [76, 107, 108, 109, 110, 111] have been already published based on the novel outcomes of this dissertation study. There is one international journal manuscript in peer-review process and its basic content is available as an internet archive file [24]. There are three more manuscripts in preparation to be submitted to international journals. All of the publications mentioned above contain the original outcomes of this dissertation and their contents are included in various chapters to follow by the permissions of the co-authors. Collaboration with other authors at METU and at Boston University have been needed especially in the fabrication phase of designed metamaterial structures.

Novel outcomes of this dissertation can be summarized under the following categories:

MNG Structures / Miniaturization:

- The double-sided SRR (DSRR) structure [13, 64, 76, 104] as well as the double-sided multiple SRR (DMSRR), and double-sided U-spiral resonator (DUSR) [16] are introduced and simulated as to be mentioned in Chapter 3 in detail. Also, a simplified equivalent circuit model is given for the BC-SRR and DSRR structures.
- Electrical sizes of the SRR, BC-SRR, MSRR, DMSRR, SR, DSR, USR, and DUSR unit cell topologies are investigated in detail. The DUSR topology is demonstrated to

have the highest level of miniaturization as to be shown in Chapter 3.

Frequency Tunable and Multi-Band Metamaterial Structures in Microwave Frequencies:

- Novel multi-band metamaterial structures are designed, fabricated and experimentally demonstrated in X-band using micro-split SRR super cells [23, 106, 110]. A MEMS based switching technique is proposed for adaptive tuning of operation bands of this metamaterial as discussed in Chapter 4.
- Also, a novel dual band magnetic resonator called single ring resonator (SLR) is designed in microwave frequencies [74, 105] as to be presented in Chapter 4.

Frequency Tunable and Multi-Band Metamaterial Structures in Terahertz Frequencies:

- The highest frequency tuning rate in metamaterial literature up-to-date, which is 51 percent in experiments and 53 percent in simulations, based on near field coupled SRR structures has been achieved, and the results are presented in Chapter 5 [24].
- Tunability of near field coupled SRR structures under electrical excitation [24] is investigated in terahertz regime as discussed in Chapter 5.

Metamaterial Sensor Applications:

- BC-SRR metamaterial sensor topologies are suggested for pressure, temperature, humidity, and concentration sensor applications [109]. Feasibility of such sensors are demonstrated by numerical simulations in Chapter 6.
- Also, the V-Shaped resonator structure [67, 107, 111] is introduced and its use as a pressure sensor is suggested as to be given in Chapter 6.
- Two different journal papers are in preparation to report the results of metamaterial sensor applications.

1.3 Organization of This Dissertation

Organization of this dissertation can be summarized as follows:

In Chapter 2, the basic theoretical aspects of metamaterials are outlined.

In Chapter 3, a novel planar magnetic metamaterial structure, called double-sided split ring resonator (DSRR) is proposed. This structure combines the characteristics of a conventional SRR and a broadside-coupled SRR (BC-SRR) to provide much better miniaturization at microwave frequencies for a given physical unit cell size. Herein, electromagnetic transmission characteristics of conventional SRR, BC-SRR, and DSRR are investigated and the results are compared for varying values of substrate parameters which are thickness, permittivity, and dielectric loss tangent. In addition to the DSRR structure, three other novel electrically-small metamaterial resonator topologies are introduced in this chapter, which are the U-spiral resonator (USR), double-sided USR (DUSR), double-sided multiple SRR (DMSRR) metamaterial structures.

In Chapter 4, a feasibility study for the design of a novel tunable multi-band metamaterials based on the use of micro-split SRR (MSSRR) structures is presented. In this study, in addition to conventional SRR (type A) structure, two modified SRR unit cells (type B and type C) having the same design topology and parameters except the additional micro-splits on the outer square ring (along the arm having the main split) are proposed. Herein, type B and type C structures (i.e. MSSRRs) are designed to have two and four additional micro-splits, respectively. Transmission characteristics of the resulting MSSRR arrays are obtained both numerically and experimentally and compared to those of the ordinary SRR unit cell. Finally, 2×2 and 3×2 inhomogeneous super cells which contain columns of different types of metamaterial unit cells are designed and fabricated. It has been shown that the resulting arrays provide two or three different frequency bands of operations due to the use of different magnetic resonators together. In addition to the MSSRR structure, another novel magnetic resonator structure called SLR (single loop resonator) showing two separate magnetic resonance frequencies and also an electric resonance in microwave region is presented.

In Chapter 5, three novel frequency tunable metamaterial designs are presented at terahertz (THz) frequencies using broadside-coupled SRR (BC-SRR) and gap-to-gap SRR arrays. In those designs, frequency tuning is obtained by in-plane horizontal or vertical displacements of the two SRR array layers, which lead to changes in near field coupling.

In Chapter 6, a BC-SRR based sensor topology is suggested which would be useful to monitor measurands like pressure, temperature, humidity or concentration. Also a V-shaped resonator

based pressure sensor is introduced. Feasibility of these novel sensor applications is demonstrated by numerical simulations.

Finally, the content, conclusions and the novel outcomes of this doctoral research study are summarized in Chapter 7, suggesting also several important problems as future work.

CHAPTER 2

THEORY OF METAMATERIALS

2.1 Characteristics of Metamaterials with Simultaneously Negative Values of Permittivity and Permeability

The permittivity ϵ and the permeability μ are the fundamental parameters of a medium which determine the propagation of electromagnetic waves since they both appear in the dispersion equation. For an isotropic medium, the dispersion relation can be defined as:

$$k^2 - \frac{\omega^2}{c^2}n^2 = 0 \quad (2.1)$$

where k is the wavenumber, ω is the angular frequency, c is the velocity of light in vacuum, and n is the refractive index of the substance. Here, n is given by

$$n = \sqrt{\mu_r \epsilon_r} \quad (2.2)$$

where μ_r is the relative permeability and ϵ_r is the relative permittivity of the substance. In general, for natural materials, μ_r , ϵ_r and n take positive numbers. However, setting μ_r and/or ϵ_r to negative numbers will result in extraordinary material properties which will be discussed in the first part of this chapter.

Since ϵ and μ appear in product form in Equations (2.1) and (2.2), these equations are not affected by the simultaneous change of the signs for ϵ and μ . On the other hand, the Faraday's law, Ampere's law and the constitutive relations, where ϵ or μ appear by itself, are good points to start to examine the effects of having simultaneously negative permittivity and permeability

(i.e. $\epsilon < 0$ and $\mu < 0$) values [1].

Differential forms of time-domain Faraday's induction law and Ampere's circuital law are given in equations 2.3 and 2.4 for a lossless ($\sigma = 0$) medium.

$$\vec{\nabla} \times \vec{E} = -\frac{\partial \vec{B}}{\partial t} \quad (2.3)$$

$$\vec{\nabla} \times \vec{H} = \frac{\partial \vec{D}}{\partial t} \quad (2.4)$$

Here, \vec{E} and \vec{H} are the electric field and magnetic field intensity vectors. Also, Equations (2.5) and (2.6) define the constitutive relations in a simple (i.e. homogeneous, linear, isotropic, and non-dispersive) medium.

$$\vec{B} = \mu \vec{H} \quad (2.5)$$

$$\vec{D} = \epsilon \vec{E} \quad (2.6)$$

For a monochromatic plane wave using $e^{j\omega t}$ convention, Faraday's law and Ampere's law can be expressed in phasor domain as

$$\vec{k} \times \vec{E} = \omega \mu \vec{H} \quad (2.7)$$

$$\vec{k} \times \vec{H} = -\omega \epsilon \vec{E} \quad (2.8)$$

where \vec{k} is the wave vector. If both ϵ and μ are positive, Equations (2.7) and (2.8) imply that the vectors \vec{k} , \vec{E} and \vec{H} form a right-handed triplet. On the other hand, if they both take negative values, then \vec{k} , \vec{E} and \vec{H} form a left-handed set. Accordingly, in 1968, Veselago called those materials as left-handed materials [1]. Directions of the vector fields, wave vector and the power flow density vector are shown in Figure 2.1 both for right-handed and left-handed media. Where the power flow density vector \vec{S} (i.e. the complex Poynting's vector) is given by

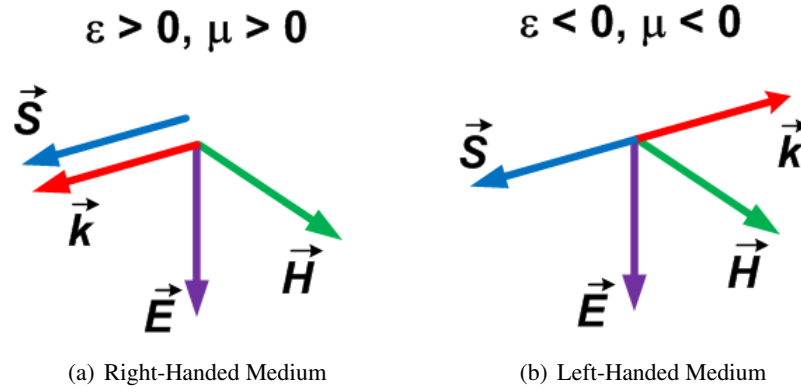


Figure 2.1: Directions of vector \vec{S} , \vec{k} , \vec{E} , and \vec{H} .

$$\vec{S} = \vec{E} \times \vec{H}^* \quad (2.9)$$

in phasor domain.

Using Equations (2.7), (2.8) and (2.9), the following additional observations can be made:

- For right-handed materials, the vectors \vec{S} and \vec{k} have the same direction, however, for left-handed materials they are in opposite directions.
- \vec{k} is in same the direction as the phase velocity. Thus, in left-handed media, phase velocity is in the opposite direction of the group velocity, which is known to be in the same direction as power flow [1].

Negative Index of Refraction

Graphical representation of passage of a ray through the boundary between two media is shown in Figure 2.2. If both *medium 1* and *medium 2* are right handed, the usual Snell's law given in Equation (2.10) is valid. The incident ray coming through path 1 is refracted through path 4 and reflected through path 2. However, if the rightness of the two medium are different a more precise form of the Snell's law given in (2.11) is used.

$$\frac{\sin \theta}{\sin \phi} = \frac{n_2}{n_1} = \sqrt{\frac{\mu_2 \epsilon_2}{\mu_1 \epsilon_1}} \quad (2.10)$$

$$\frac{\sin \theta}{\sin \phi} = \frac{n_2}{n_1} = \frac{p_2}{p_1} \left| \sqrt{\frac{\mu_2 \epsilon_2}{\mu_1 \epsilon_1}} \right| \quad (2.11)$$

where p_1 and p_2 are the rightness of the first and second medium respectively. For a right-handed medium p is set to be +1, for a left-handed medium it is set to be -1.

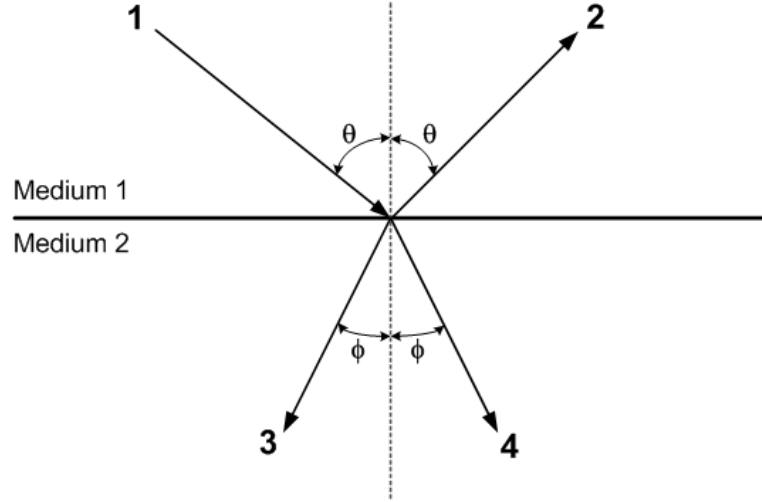


Figure 2.2: Passage of a ray through the boundary between mediums 1 and 2. 1) incident ray, 2) reflected ray, 3) refracted ray in the second medium is left handed, 4) refracted ray in the second medium is right handed.

It is significant to note that the electromagnetic waves defined by Equations (2.7) and (2.8) will propagate in a lossless medium only if this medium has a real refractive index. If either ϵ or μ is negative, then n becomes imaginary as it follows from Equation (2.2). In the case of imaginary n , wavenumber k will also be imaginary and there will be no transmission through a thick sample. If, however, ϵ and μ are both positive or both negative, electromagnetic waves will propagate through the medium. This discussion is summarized in Figure 2.3.

2.2 Methods of Obtaining Negative Permittivity, Negative Permeability and a Left-Handed Metamaterial

In this subsection, the common physical approaches to obtain negative values of permittivity and negative values permeability will be presented. Furthermore, the usefulness of these approaches in the construction of a left-handed metamaterial will be presented.

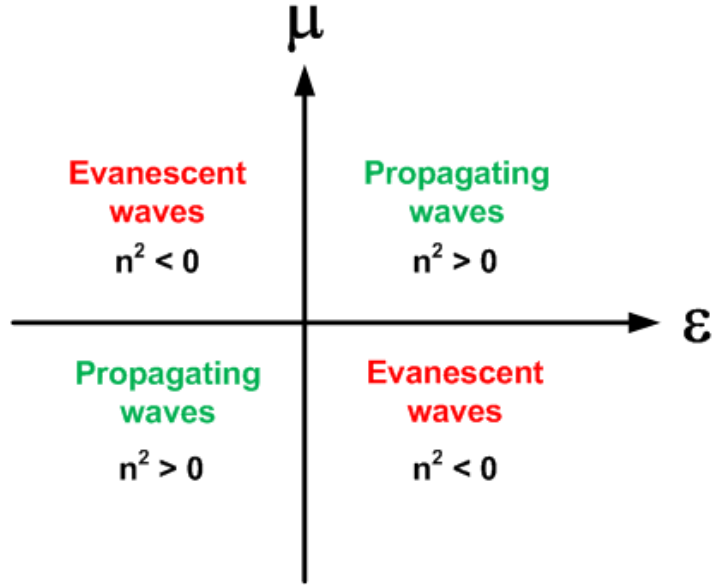


Figure 2.3: μ vs ϵ chart.

2.2.1 Negative Permittivity

2.2.1.1 Obtaining Negative Permittivity Using Thin Wire Arrays

In optical region, metals such as silver behave like a plasma of free electrons. This behavior provides negative values of permittivity, below the plasma frequency [2, 3, 5, 112]. The resulting permittivity function is given as

$$\epsilon_{metal}(\omega) = 1 - \frac{\omega_p^2}{\omega^2} \quad (2.12)$$

where ω_p is the plasma frequency and it is given in Equation (2.13) in terms of electron density n , electron mass m_e , and charge e . In microwave region, a periodic array of the thin wires shown in Figure 2.4 can be modeled as an effective medium with its permittivity function given by Equation (2.12) [2, 3, 5, 6, 113]. It is clear that such a medium shows negative values of permittivity below the plasma frequency which can be adjusted at a desired value by properly selecting array parameters. A typical permittivity versus frequency plot is produced using Equation (2.12) for $\omega_p = 10 \times 10^9$ rad/sec as shown in Figure 2.5.

$$\omega_p^2 = \frac{ne^2}{\epsilon_0 m_e} \quad (2.13)$$

For the thin wire medium described in Figure 2.4, the plasma frequency can be calculated simply by using Equation (2.14) stated below

$$\omega_p^2 = \frac{2\pi c_0^2}{a^2 \ln(a/r)} \quad (2.14)$$

where c_0 is the speed of light in vacuum, a is the lattice constant and r is the radius of the cylindrical thin wires.

To account for the resistance of normal metals, a damping term γ is introduced into Equation (2.12) and the resultant form of permittivity function is given in Equation (2.15) [3].

$$\epsilon_{metal}(\omega) = 1 - \frac{\omega_p^2}{\omega(\omega - j\gamma)} \quad (2.15)$$

In literature, Equations (2.12) and (2.15) are also known to be the Drude dispersion model for permittivity [114].

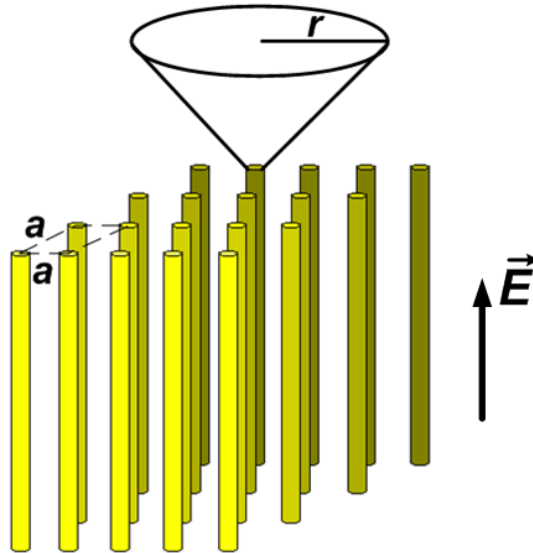


Figure 2.4: A periodic thin wire array used to obtain negative values of effective permittivity.

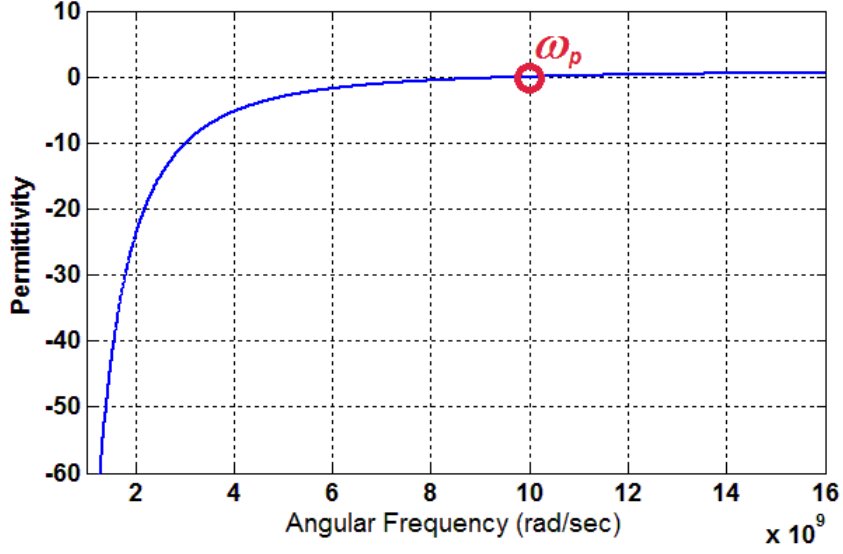


Figure 2.5: A typical permittivity vs frequency plot with plasma frequency $\omega_p = 10 \times 10^9$ rad/sec based on plasma theory. $a = 23.7 \times 10^{-3}$ m and $r = 1 \times 10^{-6}$ m

2.2.1.2 Obtaining Negative Permittivity with Special Resonator Structures

Negative values of permittivity can also be obtained by using special resonator structures which are excited electrically. The excitation techniques for the metamaterial resonator structures will be discussed in Section 2.3. The most common examples for electrical resonator topologies are the single ring split ring resonator (single ring SRR) and the electric field coupled resonator (ELC) whose schematic views and electrical excitations are shown in Figure 2.6 [60, 61, 100, 101, 102, 115, 116, 117]. Under quasi-static assumption, when we excite the SRR and ELC electrically by applying an external electric field perpendicular to their gap, they behave as an *LC* resonator circuit whose radial resonance frequency is ω_0 . Since these structures are brought to resonance electrically by the externally applied electric field, their effective permittivity functions can be explained by the Lorentz dispersion model, which is given in Equation (2.16).

$$\epsilon_{eff}(\omega) = \epsilon_{\infty} + \frac{(\epsilon_{static} - \epsilon_{\infty})\omega_0^2}{(\omega_0^2 - \omega^2) + j\omega\Gamma} \quad (2.16)$$

where $\epsilon_{static} / \epsilon_{\infty}$ are the permittivity at low / high frequency limits, ω_0 is the angular resonance frequency, and Γ is the damping frequency.

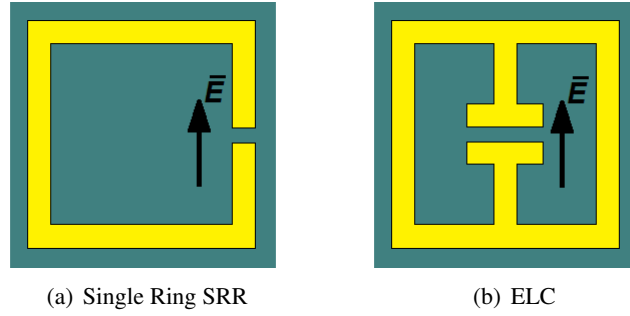


Figure 2.6: Schematic views of the split ring resonator (SRR) and the electric field coupled (ELC) resonator structures.

As a result, both structures show relatively narrow ϵ -negative (ENG) regions just above ω_0 .

The electric and magnetic excitation techniques for the metamaterial resonators will be discussed in Section 2.3 in more detail.

2.2.2 Negative Permeability

Negative values of permeability have a key role to obtain left-handedness. It is known that there is no naturally occurring material or medium showing negative values of permeability or negative refractive index [5, 6, 112]. However, it is significant to note that the existence of negative refractive index does not violate Maxwell's equations. Due to the lack of free magnetic charges in nature, the benefits of plasma-like behavior, which can be realized by the use of thin wire arrays, can not be used to obtain μ -negative (MNG) regions [11]. Thus, the artificially engineered magnetic resonator structures are the only means to obtain MNG materials. The most common metamaterial magnetic resonator structures are the SRR [5, 6, 72, 113, 118, 119], spiral resonator, labyrinth resonator (LR) [68] and the U-shaped resonator structures shown in Figure 2.7.

When a time varying magnetic field \vec{H} is applied perpendicularly to the plane of the resonator, these structures are excited magnetically. The effective permeability function of the resulting metamaterial is well described by the Lorentz dispersion model, which is given in Equation (2.17) [4, 114].

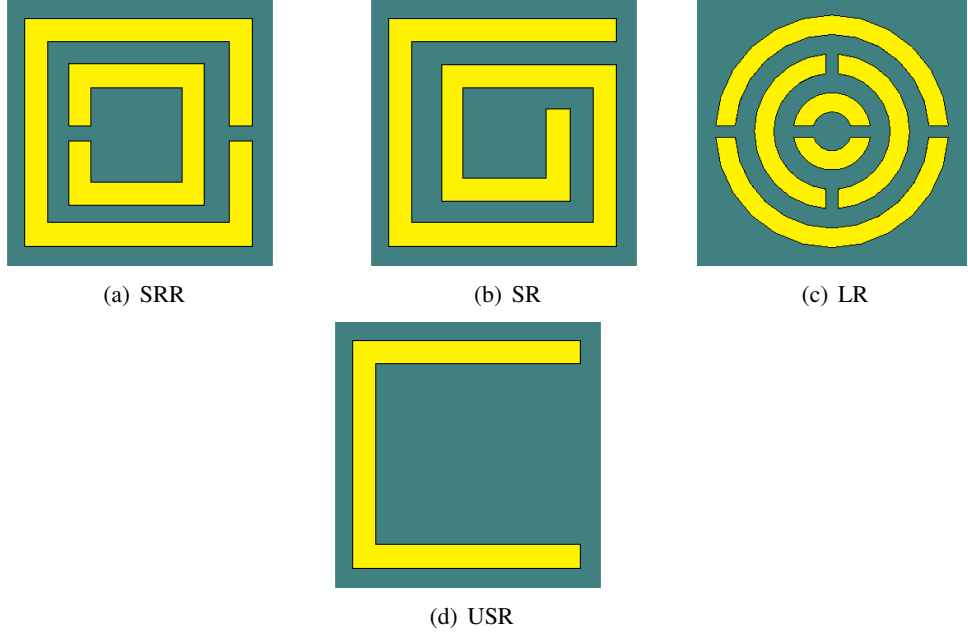


Figure 2.7: Schematic views of the split ring resonator (SRR), the spiral resonator (SR), the U-shaped resonator (USR) structure, and the labyrinth resonator structure.

$$\mu_{eff}(\omega) = \mu_{\infty} + \frac{(\mu_{static} - \mu_{\infty})\omega_0^2}{(\omega_0^2 - \omega^2) + j\omega\Gamma} \quad (2.17)$$

where $\mu_{static} / \mu_{\infty}$ are the permeability values at low / high frequency limits, ω_0 is the angular resonance frequency, and Γ is the damping frequency.

2.2.3 Realization of Left-Handed Metamaterials

In literature, left-handed metamaterials are commonly constructed as a composite effective medium which consists of a periodic magnetic resonator array and a periodic thin wire array [5, 6, 7, 120, 121, 122] designed under proper constraints. The schematic view for such a composite medium together with its excitation is shown in Figure 2.8. In this configuration, the SRR array and the thin wire array are responsible for creating the MNG and ENG regions, respectively [117, 121, 122, 123, 124]. Around the resonance frequency of the SRR array, individual transmission measurements of the wire-only (i.e. $\epsilon(\omega) < 0$ and $\mu(\omega) > 0$) and SRR-only arrays (i.e. $\epsilon(\omega) > 0$ and $\mu(\omega) < 0$) show stop-band effects. However, the composite medium (with $\epsilon(\omega) < 0$ and $\mu(\omega) < 0$) shows a transmission band called “true left-handed behavior” [121, 125, 126].

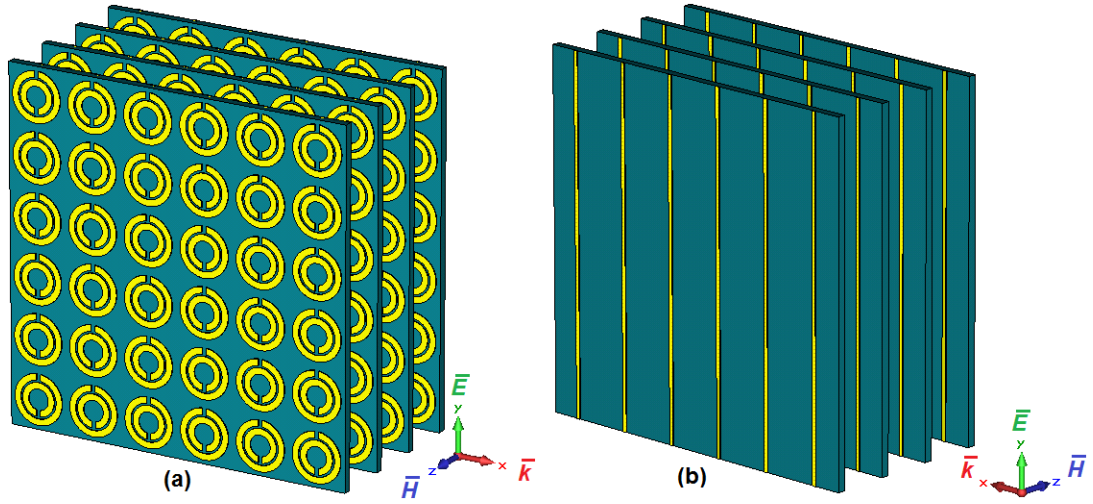


Figure 2.8: A composite left-handed medium. (a) Front and (b) back view.

Although the thin-wire array structure provides relatively broad ENG regions and it is commonly used in literature to realize a left-handed medium, a composite medium consisting of electrically and magnetically excited resonators (e.g. ELC and SRR, respectively) is also applicable [117].

2.3 Excitation Techniques for Metamaterial Resonator Structures

There are three types of excitations for metamaterial resonator structures. These are; electrical excitation, magnetic excitation, and both electrical and magnetic excitation [19, 104, 127, 128]. The choice of excitation type highly depends on the specific application. For example, if MNG regions are desired, the structure has to be excited magnetically or it has to be excited electrically in order to obtain ENG regions. However, the choice of the resonator is also very important, as well as the choice of excitation type. For instance, spiral resonators are designed only for magnetic excitations and ELC resonators are designed only for electrical excitations. Since, the SRR topology is suitable for both excitations, it will be our test structure.

Figure 2.9 summarizes excitation techniques for the SRR structure. In Figures 2.9(a) and 2.9(b), the magnetic field \vec{B} is perpendicular to the SRR plane. Therefore, it can excite the SRR's magnetic resonances based on the Faraday's law of induction. On the contrary, a magnetic field parallel to the SRR plane does not excite a magnetic resonance. Moreover, in

Figures 2.9(b) and 2.9(c), electric field \vec{E} is perpendicular to the gap of the rings. This kind of excitation technique excites electrical resonances. Hence, the structure in Figure 2.9(b) is excited both electrically and magnetically while the structure in Figure 2.9(d) is not excited at all in the LC -sense. It is significant to note here that, since the SRR is known to be a bianisotropic structure, electromagnetic couplings are expected [11, 31, 127].

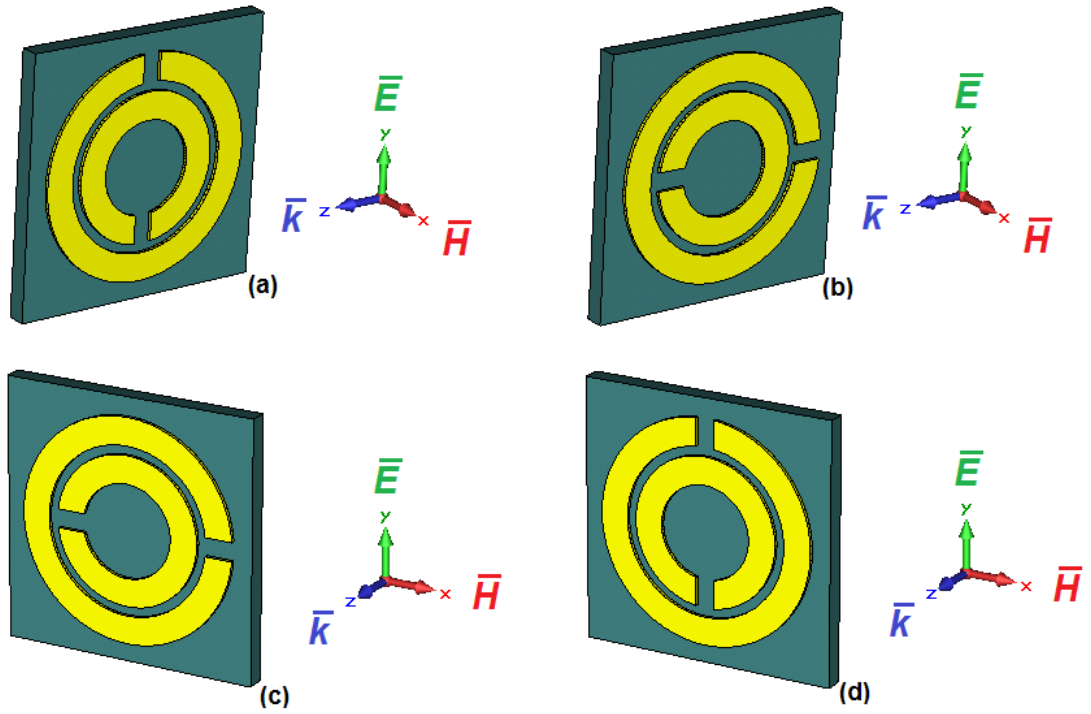


Figure 2.9: Excitation techniques for the SRR structure. (a) Only magnetic excitation. (b) Electric and magnetic excitation. (c) Only electric excitation. (d) No excitation.

2.4 Describing an Effective Metamaterial Medium

Theory of metamaterials is based on the effective medium approach that implies a homogeneous medium which consists of unit cells whose physical dimensions are much smaller than the free space wavelength. The experimental studies report that a unit cell size which is approximately equal or smaller than one-tenth of the free space wavelength at resonance satisfies the homogenization assumption [11, 31]. For a better visualization, an SRR structure which is one tenth of the free space wavelength, is shown in Figure 2.10.

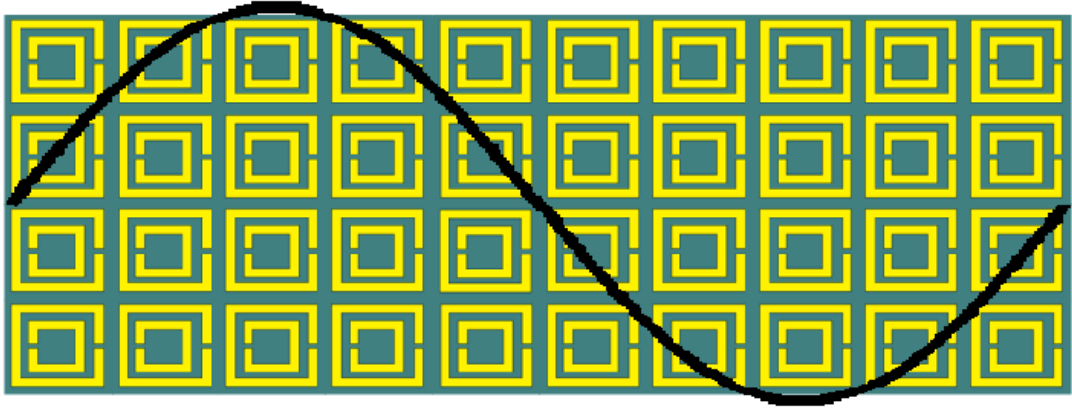


Figure 2.10: SRR array and the free-space wavelength at resonance frequency.

2.5 Simulation Techniques and Boundary Conditions

In literature, simulations of metamaterial arrays are commonly performed by commercially available full wave electromagnetic solvers where an infinitely large array is simulated using a unit cell structure and imposing proper boundary conditions. The most common boundary conditions (BC) applied to the unit cell structure are the perfect electric conductor (PEC) / perfect magnetic conductor (PMC) boundary condition pair and the periodic boundary conditions (PBC) [62, 72]. These two types of boundary conditions both simulate infinitely large arrays in two dimensions. However, there may be some differences in the simulated array topologies caused by the choice of BC type. In this part, we will illustrate the implementation of PEC/PMC BC and PBC under \vec{k} perpendicular excitation case (normal incidence) as an example.

Figure 2.11 shows the implementation of PEC/PMC BC pair under normal incidence where the PEC boundaries are imposed on the surfaces of the unit cell which are perpendicular to the incident \vec{E} -field, and the PMC boundaries are imposed on these surfaces which are perpendicular to the incident \vec{H} -field. It is well known that if a current element flows parallel to a PEC plane, its image has the same amplitude but the opposite flow direction. In other words, use of the PEC boundary condition implies the “mirror image” effect between neighboring unit cells of the simulated SRR array along the direction which is normal to the PEC boundary. Therefore, the neighboring metal arms of the original and imaged SRR unit cells, which are parallel to the PEC boundary, must carry oppositely directed currents as shown in

Figure 2.11. The resulting cell, current directions and the associated induced charge polarities of SRR cells are shown in this figure.

Implementation of the PMC boundary condition, on the other hand, requires the flow of parallel currents with the same amplitude and the same direction along the neighboring metal arms of the original and mirror cells of the SRR array along the direction normal to the PMC boundaries. The resulting current directions and the associated charge polarities are also shown in Figure 2.11.

Considering the combined effect of the PEC and PMC boundary conditions, the simulated array is actually formed of super cells composed of two SRR cells, the original and its mirror image along the vertical (normal to the PEC) direction as indicated in Figure 2.11.

Figure 2.12, on the other hand shows the implementation of periodic boundary conditions under normal incidence. Being different than the PEC/PMC BC pair, the PBC implements a completely periodic array composed of the designated unit cells as the name implies. The induced charge polarities and current directions of the image cells are the same as those in the original SRR cell.

Although the PBC implementation is the more realistic one, application of PEC/PMC BC pair has two important advantages over PBC:

- A setup which use PEC/PMC BC pair needs less simulation time.
- In CST Microwave Studio, PBC or Unit-Cell BC (i.e. a version of PBC) is not allowed in time domain solver.

When the simulated SRR arrays of Figure 2.11 and Figure 2.12 are compared, it is easily seen that they do not have the same array topology unless the original SRR array (defined in the HFSS or CST MWS softwares) is perfectly symmetrical along the direction of external \vec{E} field. The exact topology of the simulated arrays, or equivalently the current directions or charge polarities of the individual unit cells, become important while modeling the capacitive and inductive coupling effects between the unit cells of a given SRR array. All these effects are of course taken into account during the computations performed by full-wave electromagnetic solvers like HFSS and CST MWS. However, knowing the nature of such coupling effects

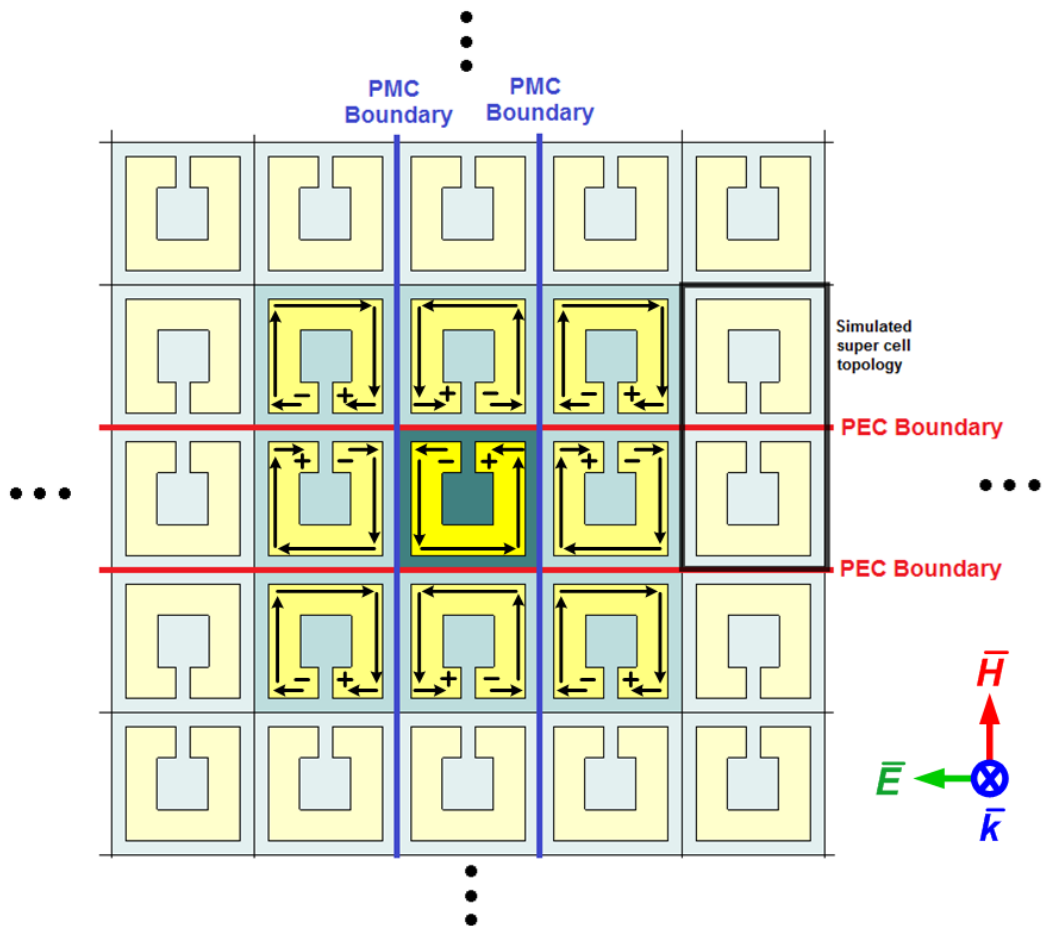


Figure 2.11: Implementation of perfect electric conductor (PEC) and perfect magnetic conductor (PMC) boundary condition pairs under normal incidence.

become critical in circuit modeling problems.

Needless to say, the full-wave simulators are efficient computational tools in metamaterial design problems estimating the electromagnetic behavior of the SRR arrays before the actual manufacturing and measurement phases. Using the boundary conditions properly and being aware of their implications is important to correctly simulate and properly model the desired array topologies.

CHAPTER 3

NOVEL DOUBLE-SIDED TOPOLOGIES FOR ELECTRICALLY-SMALL, MAGNETIC RESONATOR TYPE METAMATERIALS

3.1 Introduction

In the first part of this chapter, we describe a novel μ -negative magnetic resonator by combining the conventional SRR and the BC-SRR topologies to compose the double-sided SRR (DSRR) structure. For this kind of metamaterial topology, the early research outputs (regarding the variation of resonance frequency with the substrate parameters) were presented in a conference paper by Ekmekci et al. [64]. In this study, transmission characteristics of the DSRR, BC-SRR and SRR are investigated in a comparative manner using full-wave electromagnetic analysis to figure out the advantages of this newly suggested magnetic resonator, the DSRR, over its parent topologies, the conventional SRR and BC-SRR. For each structure, the resonance parameters, i.e. the resonance frequency (f_0), half power bandwidth (HPBW) and the transmission minimum (T_{min}), are obtained from the S -parameter spectra S_{21} for different values of substrate parameters which are the thickness of substrate (d), real part of relative permittivity (ϵ_r) and dielectric loss-tangent ($\tan \delta_c$). Numerical computations are obtained by using the Ansoft HFSS software which makes use of finite elements method. It will be shown that among these three structures, all having the same unit cell dimensions, the newly suggested DSRR is shown to reach the lowest resonance frequency, hence the smallest electrical size. It is significant to stress here that, designing a metamaterial structure with a smallest possible electrical size is a very important task to obtain a much better effective medium approach and also it is important to achieve a higher degree of device miniaturiza-

tion in microwave, terahertz and optics. Another important concern in metamaterial resonator design is the bandwidth of resonance. It will be presented that the BC-SRR promises the largest resonance bandwidth which is almost three times that of the SRR. On the other hand, the bandwidth of the DSRR approaches to the bandwidth of the BC-SRR as the planar separation distance between the inner and outer rings increases. The particular aim of this study is to investigate the resonance characteristics of the DSRR and compare them with those of the SRR and the BC-SRR designs to demonstrate the benefits (in terms of controlling resonance parameters) of using broadside coupling mechanism together with the ordinary SRR structure.

In the second part of the chapter, usefulness of the alternative multi-ring magnetic resonator topologies such as the multiple split ring resonator (MSRR), spiral resonator (SR), and U-spiral resonator (USR) for larger ring/turn numbers (N) are demonstrated [16]. The double-sided versions of these structures (i.e. DMSRR, DSR and DUSR) are suggested. Herein, the double-sided topologies do not have any conductive connection between the metallic inclusions printed on opposing faces of the substrate. For $N = 6$, the electrical size of the DSR is about 10% of the electrical size of the conventional SRR. This ratio is even smaller, 9%, for the DUSR. Even smaller electrical sizes are anticipated with the DSR and DUSR topologies for $N > 6$. However, it should be mentioned that reduction rate in resonance frequency is known to slow down and finally becomes almost zero as the turn number keeps increasing as reported by Bilotti et al. for conventional (single-sided) spiral resonators in [15].

3.2 Description of the Resonator Topologies, Structural Parameters and the Simulation Setup

3.2.1 Definition of the Geometry, Simulation Setup and the Equivalent Circuit Model

The unit cell geometries for the SRR, BC-SRR, and DSRR structures are defined in Figure 3.1(a), 3.1(b) and 3.1(c), respectively. Herein, each unit cell has the same overall size as well as the same metalization dimensions for a fair comparison in characterization. All three structures shown in Figure 3.1 have the following structural parameters: $L = 5$ mm (side length of the square shaped substrate surface), $l = 4$ mm and $h = 3$ mm (side lengths of the rectangular shaped outer ring), $g = 0.5$ mm (gap width) and $w = 0.3$ mm (width of the metal

rings). These metal rings are made of copper with the metal thickness $t_m = 0.03$ mm and conductivity $\sigma_{cu} = 58 \times 10^6$ S/m. The parameter s refers to the planar separation distance between the inner and outer rings of the SRR and DSRR structures in Figures 3.1(a) and 3.1(c), respectively. In this study simulation results are generated for two different values $s = 0.2$ and $s = 0.5$. As shown in Figure 3.1(b), the BC-SRR structure consists of two identical rings, which are the same as the outer ring of the SRR, aligned over the opposite faces of the substrate in an inverted fashion. As the BC-SRR has no inner ring, the separation parameter s is not applicable here. However, the DSRR unit cell shown in Figure 3.1(c) consists of two identical SRR structures aligned over the opposite faces of the substrate in an inverted position. In the simulation stage, use of the same lossy dielectric substrate with the relative permeability $\mu_r = 1$ is assumed for all these resonators. The other substrate parameters, i.e. the substrate thickness (d), real part of relative substrate permittivity (ϵ_r), and dielectric loss tangent ($\tan \delta_c$) will be chosen as variables during the simulations.

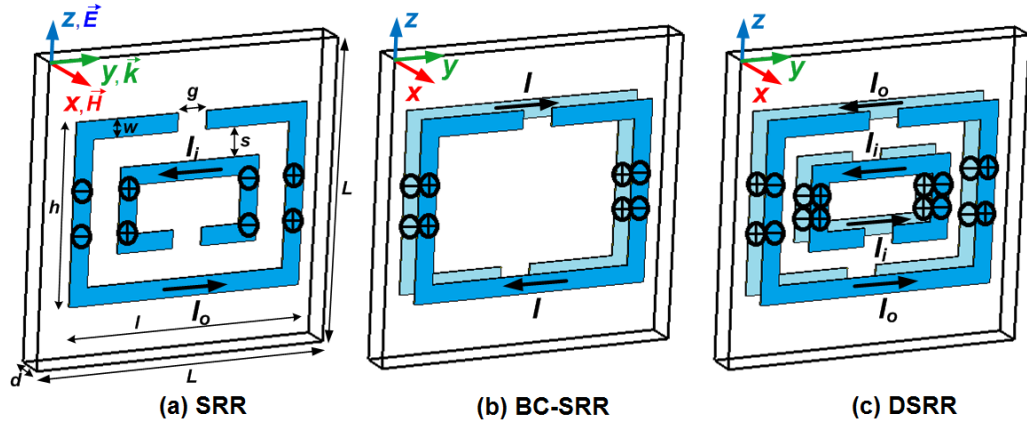


Figure 3.1: Unit cell geometries for the SRR, BC-SRR, and DSRR type metamaterials and the excitation.

Figure 3.1 also shows the directions of the surface currents induced on the rings and the associated charge distributions due to an externally applied time varying electromagnetic excitation whose magnetic field is perpendicular to the resonator planes. For the SRR case, there will be a non-zero electric polarization (along y direction) due to the applied magnetic field as implied by the polarities of induced charge distributions in Figure 3.1(a). However, there will be no electric polarization due to applied external magnetic field in the BC-SRR and DSRR topologies. Therefore, while the SRR topology is bianisotropic [11], the BC-SRR and DSRR topologies are non-bianisotropic.

Resonance characteristics of the SRR, BC-SRR and DSRR structures can be easily investigated using their transmission spectra i.e. the magnitude of the complex S_{21} parameter. A typical transmission versus frequency characteristic is given in Figure 3.2 where the definitions of resonance characteristics f_0 , $HPBW$ and T_{min} are shown. However, the complex scattering parameters S_{21} and S_{11} have to be simultaneously known for the extraction of the effective medium parameters ϵ_{eff} and μ_{eff} for the simulated metamaterial array [35]. In this study, the complex S -parameters are computed by using the Ansoft HFSS software which is based on the finite elements method.

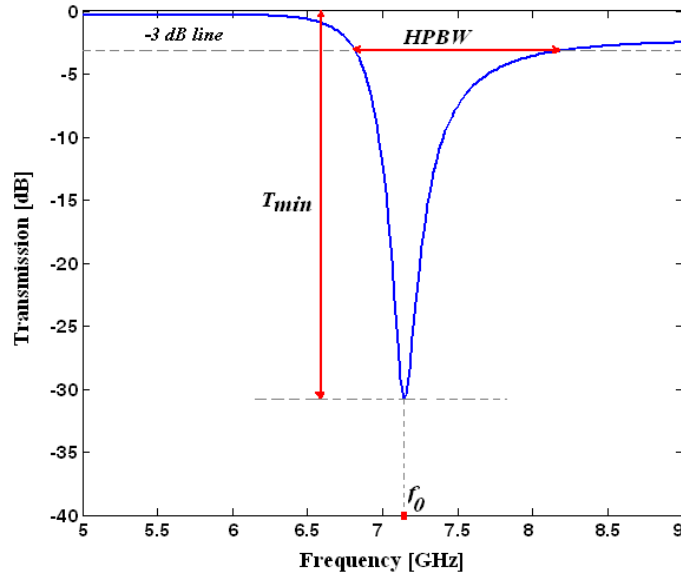


Figure 3.2: Resonance parameters (i.e. f_0 , $HPBW$, and T_{min}) defined on the transmission versus frequency curve.

Figure 3.3 shows the HFSS simulation setup where the unit cell is surrounded by an air medium. The structure is excited by an electromagnetic wave which has the propagation vector along the y axis, the electric field intensity vector (\vec{E}) along the z axis, and the magnetic field intensity vector (\vec{H}) is along the x axis. Therefore, perfect electric conductor (PEC) boundary conditions (BCs) are applied at the boundaries perpendicular to the z axis and perfect magnetic conductor (PMC) BCs are applied at the boundaries perpendicular to the x axis. The remaining two boundaries are modeled as the input-output ports. In this study, HFSS simulations are performed with 0.02 GHz incremental steps. It is significant to note that using setup shown in Figure 3.3, together with the boundary conditions, an infinitely large periodic

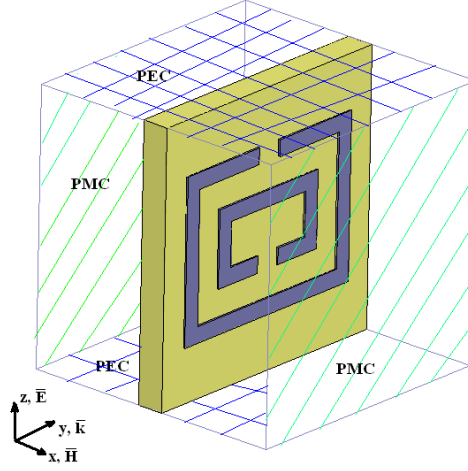


Figure 3.3: Setup for HFSS simulations.

array (in x and z directions) is simulated as indicated in literature [62, 129].

3.2.2 Equivalent Circuit Models

In the previous studies on conventional SRR structure, it has been demonstrated that the SRR structure acts as an LC resonator circuit with the angular resonance frequency of $\omega_0 = 2\pi f_0 = 1/\sqrt{LC}$ under quasi-static assumption. The calculation method for the equivalent inductance L and the equivalent capacitance C of the SRR structure printed over a dielectric substrate were suggested in [31].

Also, in [14, 19] the total distributed capacitance C between inner and outer rings of the SRR was modeled as the series connection of two equal valued capacitances ($C_s/2$) associated with each symmetrical half of the structure by Baena et al. As shown in Figure 3.4(a), the symmetry line of the SRR is drawn through the inner and outer ring gap locations. Therefore, the simplest equivalent circuit model for the SRR unit cell is shown in Figure 3.4(b) where $C = C_s/4$. In this configuration the conductor and dielectric losses are neglected. In addition to references [14, 31], calculation of the equivalent parameters L and C_s in the presence of a dielectric substrate is also discussed in [12] by Bilotti et al.

In the present study, the simple equivalent circuit model shown in Figure 3.5 is proposed for the newly suggested DSRR unit cell in order to explain the variation of the resonance

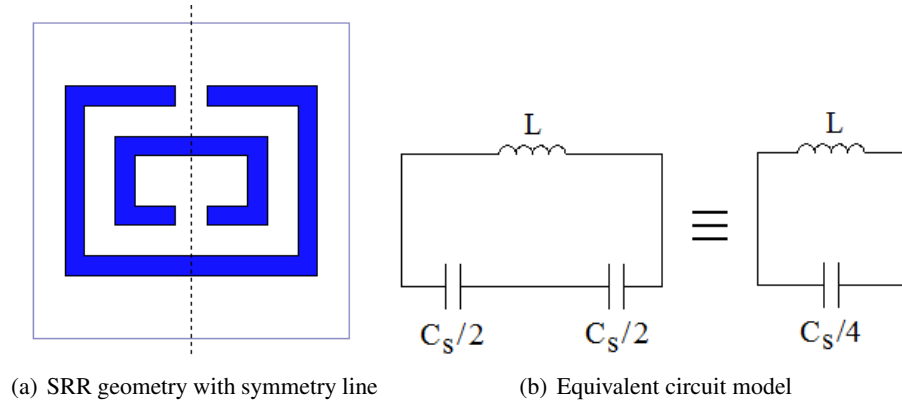


Figure 3.4: The conventional SRR topology together with its symmetry line and its basic equivalent circuit model.

frequency f_0 with the substrate parameters ϵ_r and d by neglecting the conductor and dielectric losses, the inductive coupling effects between the two SRR parts of the DSRR cell and the coupling effects between the neighboring DSRR cells of the simulated array.

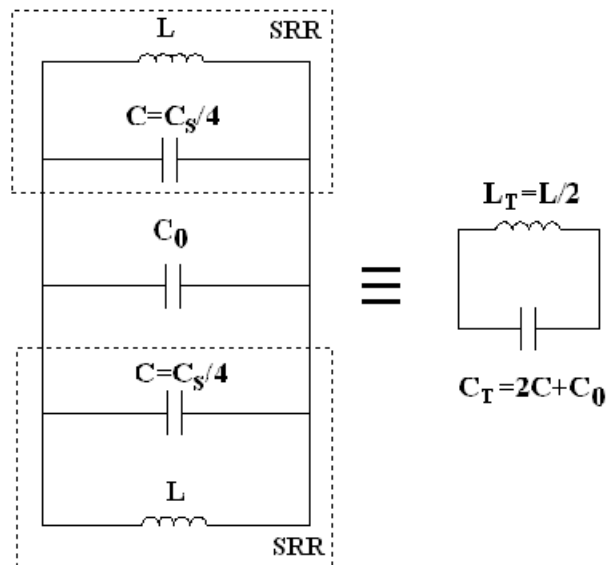


Figure 3.5: A simple equivalent circuit model proposed for the DSRR unit cell.

This DSRR equivalent circuit model is indeed composed of two identical SRR equivalent circuits and a dominant coupling capacitor C_0 where all three blocks are connected in parallel. The capacitor C_0 represents the capacitive cross coupling effect due to the oppositely polarized

conducting strips printed on the lower and upper faces of the substrate. Value of C_0 can be calculated by using the approximate formula given in (3.1).

$$C_0 = \frac{\epsilon_0 \epsilon_r A}{8d} \quad (3.1)$$

where ϵ_r and d are the real part of relative permittivity and the thickness of the substrate, respectively. Moreover, A is the total overlapping metallic strip area between two SRR structures printed over the opposite faces of the substrate. Except an empirically determined factor (1/8), this expression is basically the approximate form of the parallel-plate capacitance formula used in [77] to calculate the broadside capacitance of the BC-SRR structure. Then, because of the parallel connections, the total capacitance C_T and the total inductance L_T of the DSRR's equivalent circuit model become

$$C_T = 2C + C_0 \quad (3.2)$$

and

$$L_T = L/2 \quad (3.3)$$

Then, the resonance frequency of the DSRR unit cell can be computed by using the well-known equation

$$f_0 = \frac{1}{2\pi \sqrt{L_T C_T}} \quad (3.4)$$

The equivalent circuit model proposed for the DSRR cell can also be used to model the BC-SRR cell if the absence of the inner SRR ring is taken into account in the computation of the L and C terms. In more detail, in the absence of the inner ring, the SRR capacitance C must be composed of the gap capacitance C_g only. It is significant to note that C_g is negligibly small as compared to the capacitance between the inner and outer rings of the SRR. It is also negligible in comparison to C_0 which is the dominating capacitance term unless the substrate thickness becomes too large. The value of C_0 is expected to be smaller in the BC-SRR model due to a smaller overlapping strip area A .

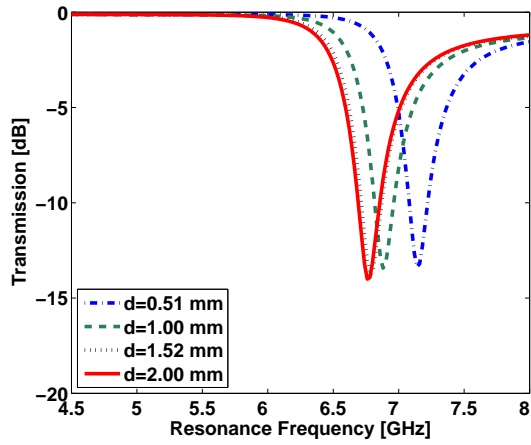
Verification of the proposed equivalent circuit model will be presented in Section 3.5 after obtaining the required HFSS simulation results for various substrate parameters in Section 3.3.

3.3 Simulation of the Resonance Behaviors for the SRR, BC-SRR, and DSRR Type Metamaterial Structures

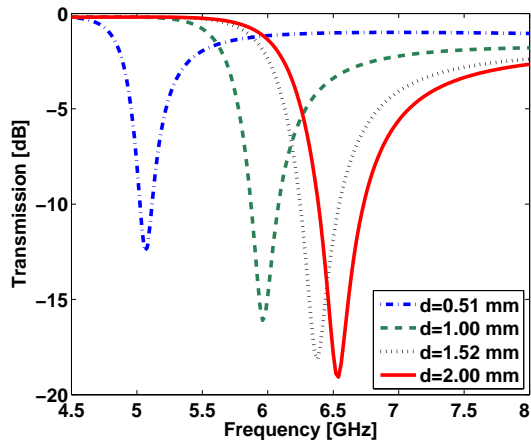
Earlier studies on the conventional SRR and BC-SRR structures [11, 31] inspired us to suggest the DSRR type magnetic resonator topology with better miniaturization [64]. Due to the presence of double-sided SRR rings, the DSRR topology provides an additional flexibility to obtain even lower resonance frequencies using the same overall physical size. A detailed comparison of the conventional SRR, BC-SRR and DSRR type metamaterials will be presented in this section regarding the effects of substrate parameters on the resonance characteristics of these closely related structures.

3.3.1 Effects of the Substrate Thickness (d) on Resonance Parameters

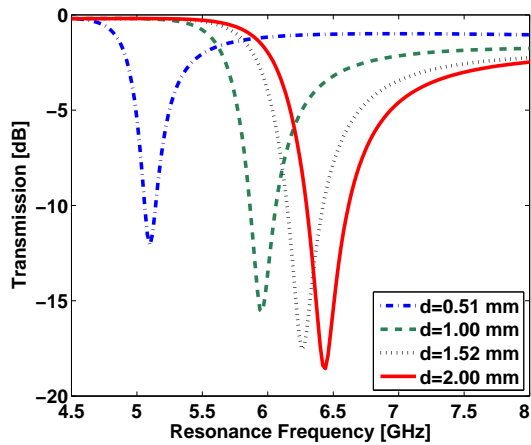
Transmission spectra of the SRR, BC-SRR and DSRR structures are numerically computed by the HFSS software. For the design, the geometrical parameters described in section 3.2.1 are used with $s = 0.5$ mm, for various substrate thicknesses $d = 0.51, 1.00, 1.52, 2.00$. In the meantime, the other substrate parameters are kept constant at values $\epsilon_r = 4.4$ and $\tan \delta_c = 0.020$. These simulations are also repeated for $s = 0.2$ mm case for the SRR and DSRR structures to observe the effects of ring separation distance. The resulting parametric curves of transmission versus frequency are shown in Figures 3.6(a), 3.6(b) and 3.6(c) for the SRR, BC-SRR and DSRR cells, respectively. The resonance frequency (f_0), half-power resonance bandwidth (*HPBW*) and transmission minimum (T_{min}) values are obtained from each of the transmission curves presented in Figure 3.6. Then, these values are sorted and plotted in Figures 3.7, 3.8 and 3.9 as f_0 versus d , *HPBW* versus d and T_{min} versus d curves, respectively. Based on the simulation results given in Figures 3.6 through 3.9, we made the following observations:



(a) SRR case



(b) BC-SRR case



(c) DSRR case

Figure 3.6: Transmission spectra of the SRR, BC-SRR, and DSRR structures for different substrate thicknesses using $L = 5$ mm, $l = 4$ mm, $h = 3$ mm, $g = 0.5$ mm, $w = 0.3$ mm, $s = 0.5$ mm, $\epsilon_r = 4.4$ and $\tan \delta_c = 0.020$.

3.3.1.1 Variation of the Resonance Frequency (f_0) with Substrate Thickness d :

- As d increases from 0.51 to 2 mm, f_0 of the SRR decreases slowly from 7.13 GHz to 6.74 GHz for $s = 0.5$ mm as seen in Figure 3.6(a) and Figure 3.7. Indeed, this behavior of f_0 is expected as the C_s term in the SRR model (see Figure 3.4(b)) increases as d gets larger [12] due to the increase in the effective permittivity of the substrate.
- On the other hand, the f_0 versus d curves of BC-SRR and DSRR structures display a totally different behavior. They both increase strongly with increasing d as seen in Figures 3.6(b), 3.6(c) and 3.7. As d increases from 0.51 to 2 mm, f_0 of the BC-SRR cell increases from 5.06 to 6.54 GHz almost exponentially. For $s = 0.5$ mm case, the f_0 versus d curve of the DSRR is very similar to that of the BC-SRR as shown in Figure 3.7. This behavior can be explained as follows: If we compare the equivalent circuit models in Figures 3.4(b) and 3.5, we can observe that increasing d only affects C in the SRR case; however it has effects on both C and C_0 in BC-SRR and DSRR models. For an increase in d , the value of C increases, but C_0 decreases (see Equation (3.1)). However, as C_0 is more dominant than C , the total capacitance C_T in Equation (3.2) decreases and hence f_0 of the BC-SRR and DSRR cells increases.
- The resonance frequencies of the SRR and DSRR structures can be decreased by reducing the planar separation distance, s . As it is obvious in Figure 3.7, for $s = 0.2$ mm case, f_0 of the SRR decreases from 6.16 to 5.96 GHz and f_0 of the DSRR increases from 4.72 to 5.62 GHz as d increases from 0.51 to 2 mm. In fact, reducing s while keeping all the other parameters (including d) fixed leads to higher C_s values [12]. Therefore, the total capacitance $C = C_s / 4$ in the SRR model and the total capacitance $C_0 + (C_s / 2)$ in the DSRR model both increase leading to smaller f_0 values. It is significant that the BC-SRR is much better than the SRR cell in terms of miniaturization, however it cannot use the tuning advantage of the parameter s . The DSRR structure, on the other hand, can have much smaller values of f_0 than those of the BC-SRR just by reducing the s parameter.

Conclusion 1: The novel DSRR structure is better than the SRR and BC-SRR structures in terms of miniaturization as it can provide much smaller f_0 values. The amount of miniaturization can be adjusted by tuning d and s when all the other parameters are constant. For

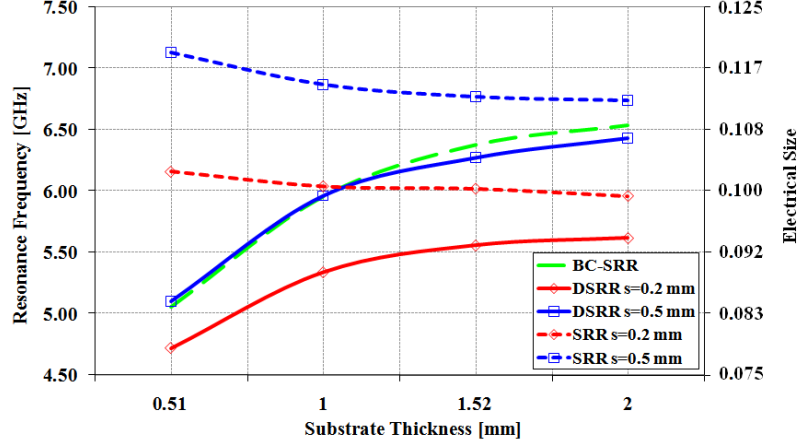


Figure 3.7: Variation of the resonance frequency (f_0) and electrical size (u) with substrate thickness (d) for the SRR, BC-SRR, and DSRR structures using $L = 5$ mm, $l = 4$ mm, $h = 3$ mm, $g = 0.5$ mm, $w = 0.3$ mm, $s = 0.5$ mm, $\epsilon_r = 4.4$ and $\tan \delta_c = 0.020$.

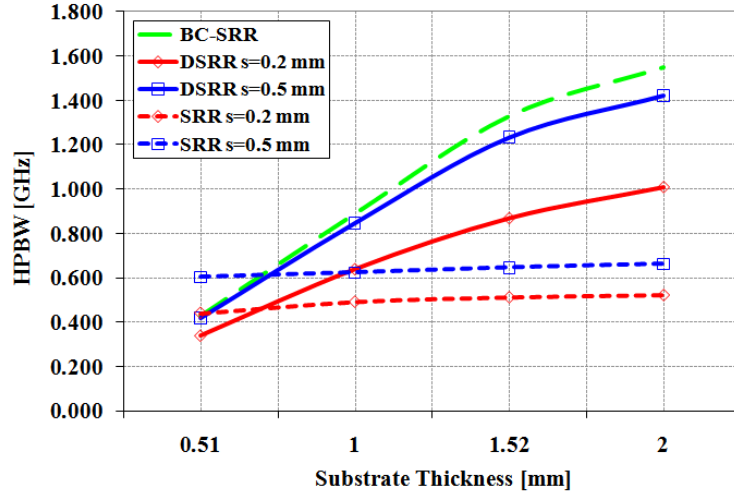


Figure 3.8: Variation of the resonance bandwidth ($HPBW$) with substrate thickness (d) for the SRR, BC-SRR, and DSRR structures using $L = 5$ mm, $l = 4$ mm, $h = 3$ mm, $g = 0.5$ mm, $w = 0.3$ mm, $s = 0.5$ mm, $\epsilon_r = 4.4$ and $\tan \delta_c = 0.020$.

example, a reduction of 28.5 % is obtained in f_0 (reduction from 7.13 GHz to 5.10 GHz) for $d = 0.51$ mm and $s = 0.5$ mm by using DSRR instead of SRR. Reduction in f_0 becomes 23.4 % (from 6.16 GHz to 4.72 GHz) if $s = 0.2$ mm is used instead. Also, reduction in f_0 is more significant for smaller s and larger d values when the BC-SRR and DSRR structures are compared. For example, the reduction in f_0 is almost zero when $s = 0.5$ mm, however it is 14 % for $s = 0.2$ mm at $d = 2$ mm and it is only 6.7 % for $s = 0.2$ at $d = 0.51$ mm.

3.3.1.2 Variation of the Half-Power Bandwidth (*HPBW*) with Substrate Thickness *d*:

- As *d* increases from 0.51 to 2 mm, the *HPBW* of the SRR increases very slightly. Practically, we can assume that the *HPBW* versus *d* curve of the SRR remains almost constant at about 0.6 GHz for *s* = 0.5 mm and at about 0.45 GHz for *s* = 0.2 mm (see Figure 3.8).
- The largest increase in *HPBW* with respect to *d* is observed for the BC-SRR structure, from 0.43 to 1.55 GHz, as shown in Figure 3.8.
- The *HPBW* versus *d* curve of the DSRR shows a similar behavior as that of the BC-SRR. For small *s* values, the *HPBW* of the DSRR becomes much smaller than that of the BC-SRR. For *s* = 0.2 mm, for instance, the *HPBW* of the DSRR increases from 0.34 to 1.01 GHz. As *s* increases, on the other hand, the *HPBW* versus *d* curve of the DSRR starts to converge to that of the BC-SRR as shown in Figure 3.8.

Conclusion 2: The BC-SRR structure is better than the SRR and DSRR structures in terms of having a larger resonance bandwidth. However, the bandwidth performance of the novel DSRR cell gets very close to that of the BC-SRR for larger ring separation, *s*. In fact *HPBW* is one of the most important parameters in metamaterial structures, because an increase in *HPBW* increases the frequency band with negative permeability for magnetic excitation, hence helps to increase the left-handed operational region.

3.3.1.3 Variation of the Transmission Minimum (T_{min}) with Substrate Thickness *d*:

- As *d* increases from 0.51 to 2 mm, T_{min} of the SRR decreases very slightly from -13.33 to -14 dB for *s* = 0.5 mm, and from -12.18 to -13.41 dB for *s* = 0.2 mm (see Figure 3.6(a) and Figure 3.9).
- The T_{min} versus *d* curves of the DSRR and BC-SRR cells, however, decrease sharply by more than 6 dB (roughly from -12 dB to -18 dB) as *d* increases from 0.51 to 2 mm as demonstrated in Figures 3.6(b), 3.6(c) and Figure 3.9.

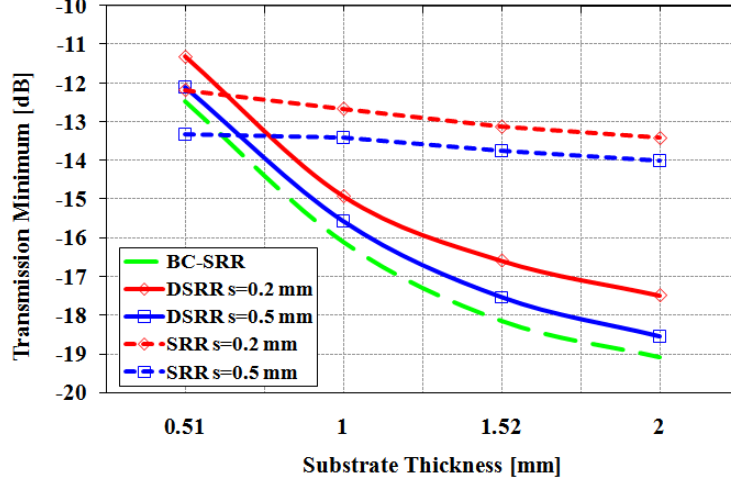
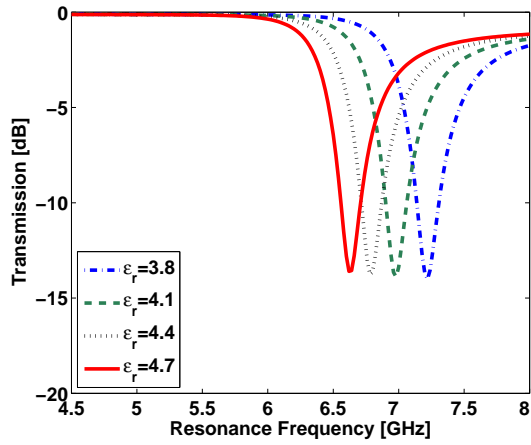


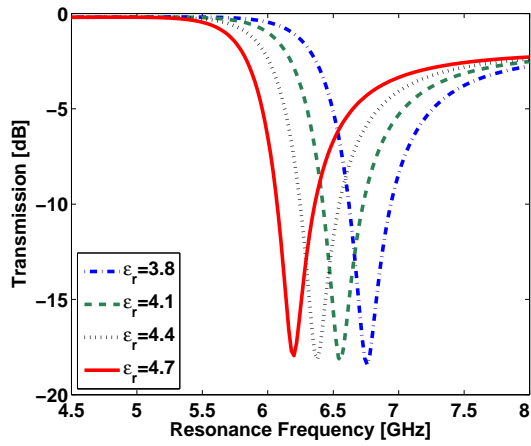
Figure 3.9: Variation of the transmission minimum (T_{min}) with substrate thickness (d) for the SRR, BC-SRR, and DSRR unit cells using $L = 5$ mm, $l = 4$ mm, $h = 3$ mm, $g = 0.5$ mm, $w = 0.3$ mm, $s = 0.5$ mm, $\epsilon_r = 4.4$ and $\tan \delta_c = 0.020$.

3.3.2 Effects of the Relative Permittivity (ϵ_r) of the Substrate on Resonance Parameters

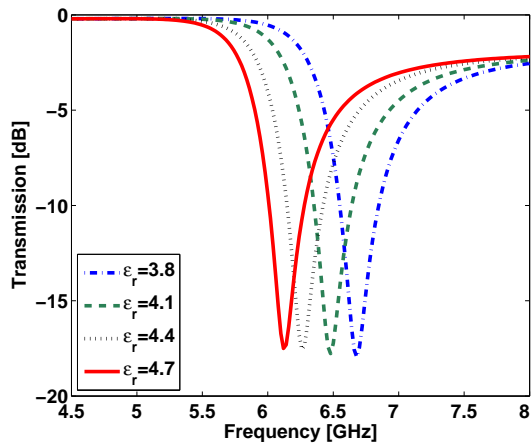
Transmission spectra of the SRR, BC-SRR and DSRR structures are numerically computed by the HFSS software, using the design parameters described in Section 3.2 with $s = 0.5$ mm, for various substrate permittivity values. The simulations are performed for $\epsilon_r = 3.8, 4.1, 4.4$ and 4.7 values while the other substrate parameters are kept constant at $d = 1.52$ mm and $\tan \delta_c = 0.020$. These simulations are also repeated for the SRR and DSRR structures with $s = 0.2$ mm. The resulting parametric curves of transmission versus frequency are plotted in Figures 3.10(a), 3.10(b) and 3.10(c) for the SRR, BC-SRR and DSRR cells, respectively. The resonance frequency (f_0), half-power resonance bandwidth ($HPBW$) and transmission minimum (T_{min}) values are obtained from each of the transmission curves presented in Figure 3.10. Then, these values are sorted and plotted in Figures 3.11, 3.12 and 3.13 as f_0 versus ϵ_r , $HPBW$ versus ϵ_r and T_{min} versus ϵ_r curves, respectively. As the range of variation for ϵ_r (from 3.8 to 4.7) is quite small, the nonlinear relations between the substrate permittivity and resonance parameters are not revealed in Figure 3.10. Additional simulations are run for $\epsilon_r = 1.0, 2.5$ and 6.15 , and these results are included in Figures 3.11, 3.12 and 3.13 to cover a wider range for (ϵ_r) from 1.0 to 6.15. Based on the simulation results presented in Figures 3.10 through 3.13, we make the following observations:



(a) SRR case



(b) BC-SRR case



(c) DSRR case

Figure 3.10: Transmission spectra of the SRR, BC-SRR, and DSRR structures for different substrate permittivity values using $L = 5$ mm, $l = 4$ mm, $h = 3$ mm, $g = 0.5$ mm, $w = 0.3$ mm, $s = 0.5$ mm, $d = 1.52$ and $\tan \delta_c = 0.020$.

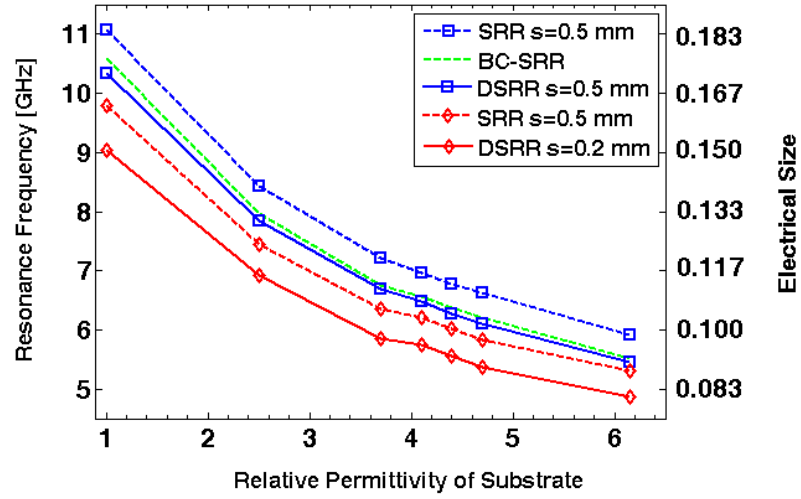


Figure 3.11: Variation of the resonance frequency (f_0) and electrical size (u) with relative substrate permittivity (ϵ_r) for the SRR, BC-SRR, and DSRR structures using $L = 5$ mm, $l = 4$ mm, $h = 3$ mm, $g = 0.5$ mm, $w = 0.3$ mm, $d = 1.52$ mm and $\tan \delta_c = 0.020$.

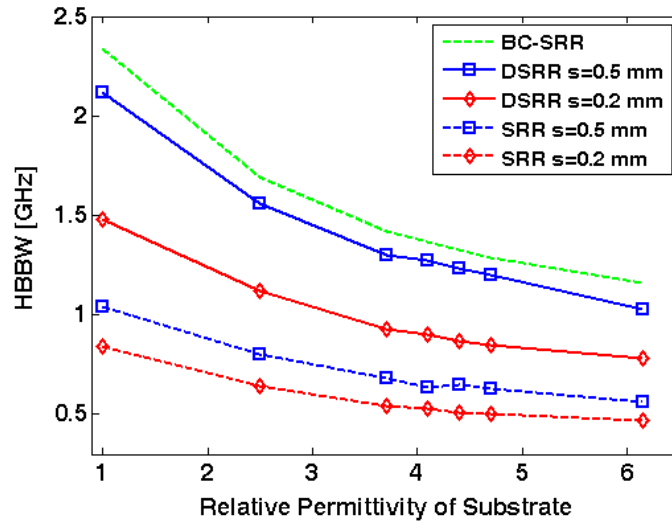


Figure 3.12: Variation of the resonance bandwidth ($HPBW$) with relative substrate permittivity (ϵ_r) for the SRR, BC-SRR, and DSRR structures using $L = 5$ mm, $l = 4$ mm, $h = 3$ mm, $g = 0.5$ mm, $w = 0.3$ mm, $d = 1.52$ mm and $\tan \delta_c = 0.020$.

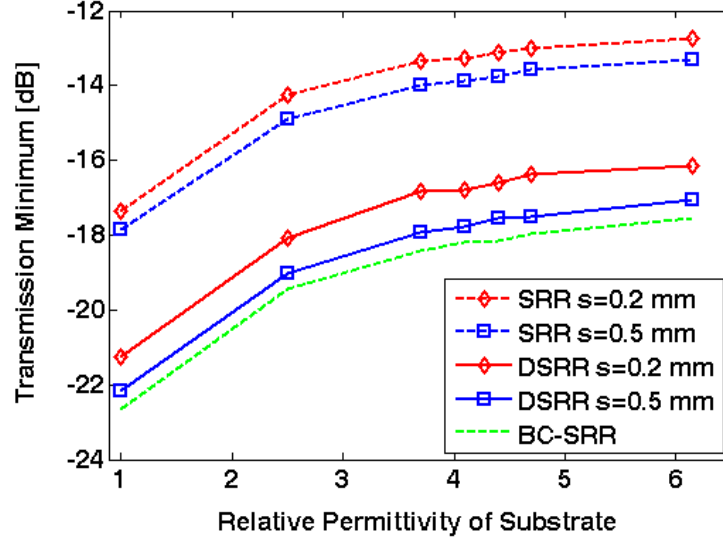


Figure 3.13: Variation of the transmission minimum (T_{min}) with relative substrate permittivity (ϵ_r) for the SRR, BC-SRR, and DSRR structures using $L = 5$ mm, $l = 4$ mm, $h = 3$ mm, $g = 0.5$ mm, $w = 0.3$ mm, $d = 1.52$ mm and $\tan \delta_c = 0.020$.

3.3.2.1 Variation of the Resonance Frequency (f_0) with the Relative Permittivity ϵ_r of the Substrate:

As the substrate relative permittivity ϵ_r increases from 3.8 to 4.7, f_0 decreases almost linearly and with almost the same slope for all three resonator structures under investigation as seen in Figures 3.10 and 3.11. When the ϵ_r range is extended from 1.0 to 6.15 with some additional simulation results, the nonlinearly decreasing behavior in f_0 versus ϵ_r curves of SRR, BC-SRR and DSRR structures is observed as expected from the circuit models. Within this ϵ_r range, for the given set of fixed parameter values, the DSRR structure with $s = 0.2$ mm has the lowest curve of f_0 versus ϵ_r . That means, DSRR structure provides the smallest electrical size (i.e. the best miniaturization) under this condition.

3.3.2.2 Variation of the Resonance Bandwidth ($HPBW$) with the Relative Permittivity ϵ_r of the Substrate:

As shown in Figures 3.10 and 3.12, the $HPBW$ versus ϵ_r curves of all three resonator structures decrease almost exponentially as ϵ_r increases. The BC-SRR demonstrates the largest $HPBW$ values in this substrate permittivity range changing from 2.3 to 1.2 GHz. The $HPBW$ versus

ϵ_r curve of the DSRR with $s = 0.5$ mm is the second best in providing large *HPBW* values changing from 2.1 to 1.0 GHz. The SRR cell with $s = 0.2$ mm has the lowest *HPBW* values changing from 0.8 to 0.5 GHz. *HPBW* values of the BC-SRR is almost three times the *HPBW* values of the SRR under these simulation conditions.

3.3.2.3 Variation of the Transmission Minimum (T_{min}) with the Relative Permittivity ϵ_r of the Substrate:

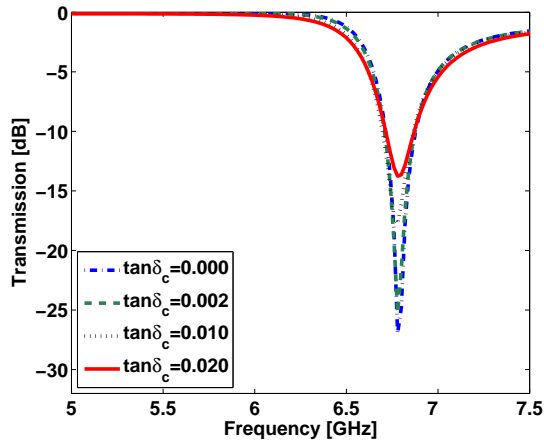
As seen in Figures 3.10 and 3.13, the T_{min} versus ϵ_r curves of all three resonator structures increase almost exponentially as ϵ_r increase from 1.0 to 6.15. Transmission minimums at the resonance for the BC-SRR and DSRR cells are smaller by about 4 dB as compared to those of the SRR structure for all ϵ_r values. Smaller T_{min} at resonance leads to higher unloaded quality factor [18], hence it is the indication of smaller losses.

3.3.3 Effects of the Loss Tangent ($\tan \delta_c$) of the Substrate on Resonance Parameters

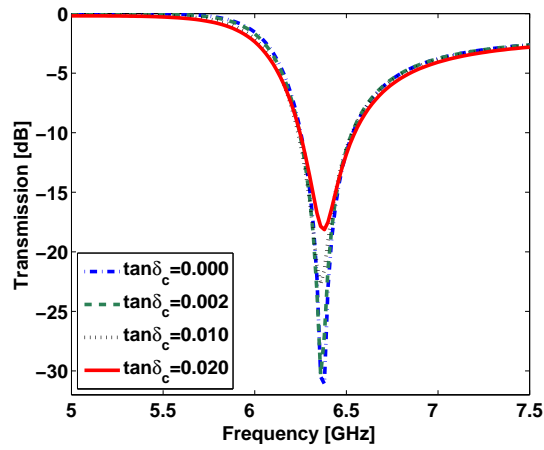
Transmission spectra of the SRR, BC-SRR and DSRR structures are numerically computed by the HFSS software using the geometrical parameters described in Section 3.2.1 with $s = 0.5$ mm and for various substrate loss tangent values which are $\tan \delta_c = 0, 0.002, 0.010, 0.020$. In the meantime, the other substrate parameters are kept constant at values $d = 1.52$ mm and $\epsilon_r = 4.4$. The resulting parametric curves of transmission versus frequency are plotted in Figures 3.14(a), 3.14(b) and 3.14(c) for the SRR, BC-SRR and DSRR structures, respectively. It is seen in Figure 3.14(a) that f_0 and the *HPBW* of SRR do not change much by $\tan \delta_c$. Only T_{min} changes from about -26.99 to -13.75 dB as $\tan \delta_c$ changes from 0 to 0.020. In other words, the resonance curve becomes shallower as the losses of the dielectric substrate increases. The similar behavior is observed for BC-SRR and DSRR cells also as seen in Figures 3.14(b) and 3.14(c), respectively.

3.4 Comparison of the Electrical Sizes of the SRR, BC-SRR, and DSRR Unit Cells

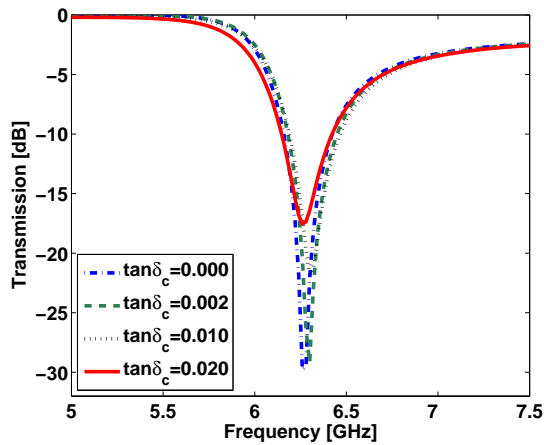
Electrical size of a resonator cell is defined as



(a) SRR case



(b) BC-SRR case



(c) DSRR case

Figure 3.14: Transmission spectra of the SRR, BC-SRR, and DSRR structures for different loss tangent values of substrate using $L = 5$ mm, $l = 4$ mm, $h = 3$ mm, $g = 0.5$ mm, $w = 0.3$ mm, $s = 0.5$ mm, $\epsilon_r = 4.4$ and $d = 1.52$ mm.

$$u = \frac{D}{\lambda_0} = \frac{D}{c/f_0} = f_0 \frac{D}{c} \quad (3.5)$$

where D is the maximum linear dimension of the resonator, which is spatial diagonal $\sqrt{h^2 + l^2} = \sqrt{3^2 + 4^2} = 5$ mm for all the rectangular unit cells investigated in this study, c is the velocity of light in vacuum and λ_0 is the free space wavelength at f_0 [15]. Electrical size of a meta-material unit cell is a very important property because of two reasons: First of all, smaller electrical size yields a better effective medium approximation and thus more accurate results from the quasi-static analysis [75]. Moreover, electrically smaller structures are preferred in most of the microwave applications for miniaturization purposes [15]. Using Equation (3.5) and the simulation results at f_0 in Figures 3.7 and 3.11, it is easy to obtain u versus d and u versus ϵ_r curves for the SRR, BC-SRR and DSRR unit cells. As u is proportional to f_0 as seen in Equation (3.5), the resulting electrical size curves are the same as the f_0 versus d and f_0 versus ϵ_r curves plotted in Figure 3.7 and Figure 3.11, apart from the proportionality constant (D/c). The proper scale for the electrical size is indicated on the right vertical axis of those figures. It is obvious from these results that, the electrically smallest resonator structure for all d and ϵ_r values is the DSRR structure with $s = 0.2$ mm. It is also seen in Figure 3.7 that the DSRR topology with $s = 0.5$ mm provides a reduction of 29 % in f_0 as compared to the SRR topology with $s = 0.5$ mm for $d = 0.51$ mm case. In the case of $s = 0.2$, the reduction in f_0 provided by the use of DSRR cell instead of SRR cell is 23 % again for $d = 0.51$ mm.

3.5 Verification of the Equivalent Circuit Model for DSRR

A simple equivalent circuit model for the DSRR unit cell is suggested in Section 3.2.2. In the present section, we will verify that model using the already completed full wave electromagnetic simulation results. The equivalent circuits for the SRR structures used in our simulations have the inductance values of $L = 14.4$ nH and $L = 19$ nH for the cases of $s = 0.5$ mm and $s = 0.2$ mm, respectively, which are calculated using the inductance expression 3.6 provided in [12].

$$L = 4\mu_0[l_{outer} - (s + w)] \left[\ln \left(\frac{0.98}{\rho} \right) + 1.84\rho \right] \quad (3.6)$$

In this equation l_{outer} is the one side-length of the square shaped outer ring, s is the separation distance between adjacent strips, w is the strip width, and ρ is the filling ratio defined in (3.7) where l_{inner} is the one side-length of the square shaped inner ring. As seen in Equation (3.6), the SRR's inductance value is independent of the substrate thickness and permittivity.

$$\rho = \frac{l_{outer} - l_{inner}}{l_{outer} + l_{inner}} = \frac{w + s}{l_{outer} - (w + s)} \quad (3.7)$$

The corresponding C values appearing in the SRR circuit blocks, on the other hand, are computed from the knowledge of L and f_0 (of the SRR) for each set of substrate parameters. Finally, the parameters L_T , C_0 , C_T and the resonance frequency f_0 of the DSRR structure are computed using Equations (3.1) through (3.4). The model-based f_0 values extracted for the DSRR structure for $d = 0.51, 1.00, 1.52, 2.00$ mm with the fixed parameter values of $L = 5$ mm, $l = 4$ mm, $h = 3$ mm, $g = 0.5$ mm, $w = 0.3$ mm, $s = 0.5$ mm, $\epsilon_r = 4.4$ and $\tan \delta_c = 0.020$ are listed in Table 3.1 together with the corresponding HFSS-based f_0 values. The HFSS-based and model-based f_0 values of Table 3.1 are plotted in Figure 3.15. Similarly, Table 3.2 lists the f_0 values of the DSRR cell obtained by using the HFSS software for $\epsilon_r = 1, 2.5, 3.8, 4.1, 4.4, 4.7, 6.15$ with the fixed parameter values $L = 5$ mm, $l = 4$ mm, $h = 3$ mm, $g = 0.5$ mm, $w = 0.3$ mm, $s = 0.5$ mm, $d = 1.52$ mm and $\tan \delta_c = 0.020$. The corresponding model-based f_0 values are also listed in Table 3.2. Again the HFSS-based and model-based f_0 values of Table 3.2 are plotted in Figure 3.16. As it is seen in Table 3.1, Table 3.2 and Figures 3.15 and 3.16, results of equivalent circuit model are found in very good agreement with the results of the HFSS simulations.

Table 3.1: Resonance frequencies for the DSRR topology obtained from the HFSS simulations and from the equivalent circuit model for different values of relative substrate thickness (d) where $\epsilon_r = 4.4$ mm and $\tan \delta_c = 0.020$.

d [mm]	s = 0.5 mm				s = 0.2 mm			
	f_0 [GHz] HFSS	f_0 [GHz] Model	% error	$C=C_s/4$ [pF]	f_0 [GHz] HFSS	f_0 [GHz] Model	% error	$C=C_s/4$ [pF]
0.51	5.10	5.68	11.4	0.030	4.72	4.71	0.2	0.032
1.00	5.96	6.08	2.0	0.035	5.34	5.20	2.6	0.035
1.52	6.27	6.30	0.5	0.036	5.56	5.42	2.5	0.036
2.00	6.43	6.38	0.8	0.037	5.62	5.50	2.1	0.037

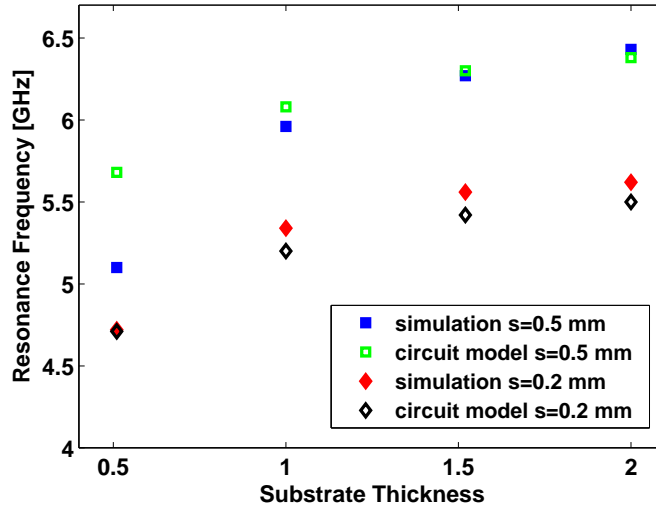


Figure 3.15: Resonance frequencies obtained from HFSS simulations and from the equivalent circuit model for different substrate thicknesses where $\epsilon_r = 4.4$ and $\tan \delta_c = 0.020$.

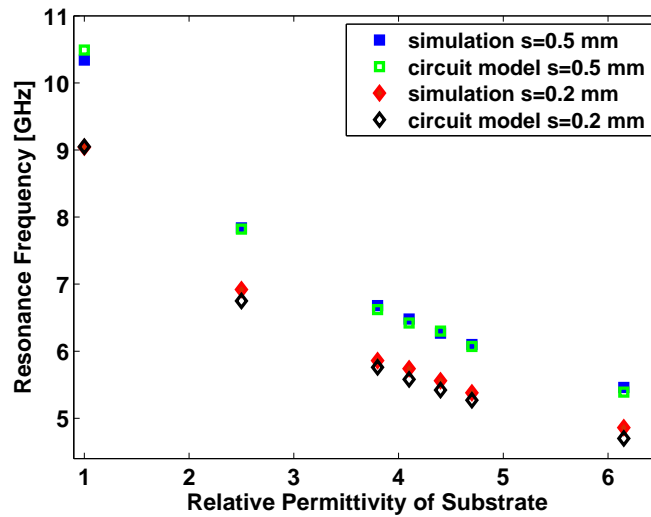


Figure 3.16: Resonance frequencies obtained from HFSS simulations and from the equivalent circuit model for different values of substrate relative permittivity where $d = 1.52$ mm and $\tan \delta_c = 0.020$.

3.6 A Left Handed Medium with DSRR Structure

In this part, the DSRR unit cell is combined with a conducting strip having the length of 5 mm, width of 0.5 mm, and thickness of 0.03 mm as shown in Figure 3.17 to obtain left hand-

Table 3.2: Resonance frequencies for the DSRR topology obtained from the HFSS simulations and from the equivalent circuit model for different values of relative substrate permittivity (ϵ_r) where $d = 1.52$ mm and $\tan \delta_c = 0.020$.

ϵ_r	s = 0.5 mm				s = 0.2 mm			
	f_0 [GHz] HFSS	f_0 [GHz] Model	% error	$C=C_s/4$ [pF]	f_0 [GHz] HFSS	f_0 [GHz] Model	% error	$C=C_s/4$ [pF]
1	10.34	10.49	1.5	0.014	9.04	9.05	0.1	0.014
2.5	7.84	7.82	0.3	0.024	6.92	6.75	2.5	0.024
3.8	6.68	6.62	0.9	0.033	5.86	5.76	1.7	0.032
4.1	6.48	6.42	0.9	0.035	5.74	5.58	2.8	0.034
4.4	6.27	6.30	0.5	0.036	5.56	5.42	2.5	0.036
4.7	6.1	6.07	0.5	0.039	5.38	5.27	2.0	0.038
6.15	5.45	5.39	1.3	0.049	4.86	4.7	3.2	0.047

edness. Herein, the DSRR unit cell parameters are the same as those mentioned in Section 3.2.1 which were $l = 4$ mm, $h = 3$ mm, $g = 0.5$ mm, $w = 0.3$ mm, $s = 0.5$ mm and the substrate parameters are taken as $L = 5$ mm, $d = 1.52$ mm, $\epsilon_r = 4.4$ and $\tan \delta_c = 0.020$. In the left-handed metamaterial unit cells, the cell combination is composed of the ordinary SRR structure pointed on one side and the conducting strip is printed over the back side of the substrate. Obviously, this composition is not suitable for the BC-SRR or DSRR structures as both sides of the substrate are used for printing SRR structures. For these double sided cases, embedding the conducting strip inside the substrate is feasible during the fabrication using a high resolution LPKF milling machine. With this convenient and inexpensive manufacturing technique, it is possible to combine two substrates with SRR patterns printed on their outer faces and anti-symmetrically aligned with respect to each other while only one of the substrates has the conducting strip printed on its inner side facing the second substrate. In other words, manufacturing the metamaterial structure shown in Figure 3.17 is not too complicated but quite feasible indeed.

3.6.1 Extraction of Effective Medium Parameters

In metamaterial design, use of unit cells with sufficiently small electrical sizes is essential while forming periodic array structures. If the maximum linear dimension of the unit cell is much smaller than the free space wavelength of operation, then the resulting structure can be considered as an “effective” material and “effective permittivity” and “effective permeability” definitions can be made. From the electromagnetic analysis point of view, the quasi-static

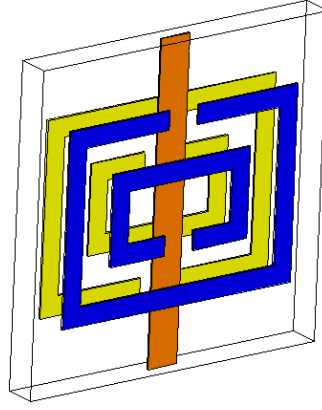


Figure 3.17: Left-handed unit-cell composed of a DSRR and a conducting strip.

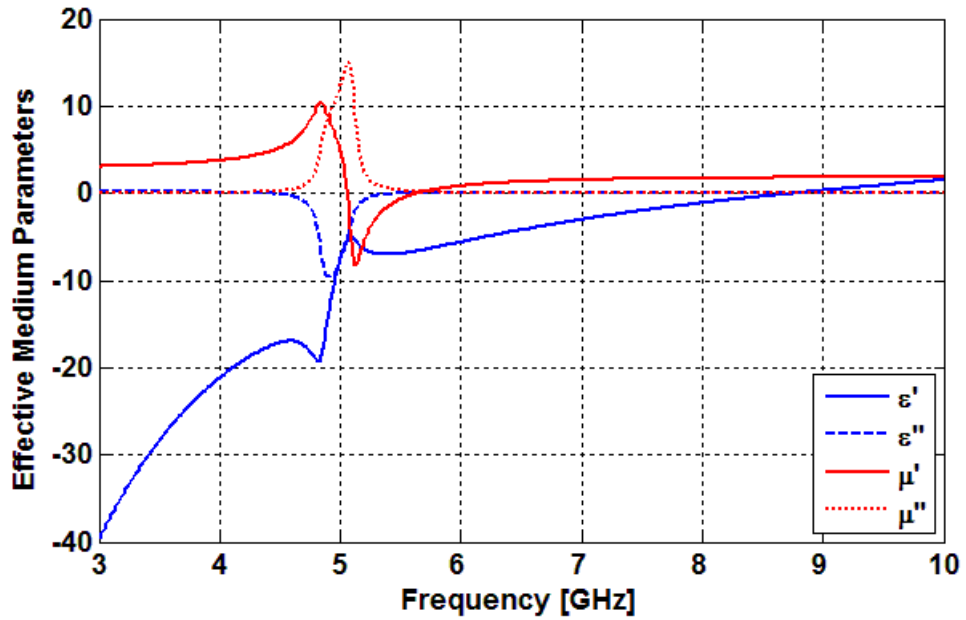


Figure 3.18: Complex effective medium parameters of the structure given in Figure 3.17. $\epsilon_{eff} = \epsilon'_{eff} - \epsilon''_{eff}$ and $\mu_{eff} = \mu'_{eff} - \mu''_{eff}$ using $e^{j\omega t}$ time dependence.

approach used in the analysis of metamaterials will be more accurate as the electrical size of metamaterial unit cells get smaller. Typically, the maximum linear dimension of the unit cell needs to be at least one tenth of the wavelength to be electrically small. However, in some references larger ratios up to one fifth are considered to be sufficiently small.

The complex S_{11} and S_{21} spectra of the simulated periodic metamaterial array are used to extract the complex effective medium parameters (ϵ_{eff}) and (μ_{eff}) over the frequency band

of simulation [72]. There are various parameter retrieval methods reported in literature. In this study, we follow the procedure given in [35] by Ghodgaonkar et al. where the complex S -parameters S_{11} and S_{21} can be expressed as

$$S_{11} = \frac{\Gamma(1 - T^2)}{1 - \Gamma^2 T^2} \quad (3.8)$$

and

$$S_{21} = \frac{T(1 - \Gamma^2)}{1 - \Gamma^2 T^2} \quad (3.9)$$

for a metamaterial slab having the thickness d in the direction of incident plane wave propagation. For magnetic excitation (i.e. for \vec{H} perpendicular to the SRR plane) case, d is the length of the SRR unit cell along the propagation direction. However, for electrical excitation (i.e. for \vec{k} perpendicular to the SRR plane) case, d is the thickness of the substrate plus thickness of the metal for single layer arrays. The Γ and T seen Equations (3.8) and (3.9) are given as follows:

$$\Gamma = \frac{(Z_{sn} - 1)}{(Z_{sn} + 1)} \quad (3.10)$$

is the reflection coefficient of air-sample interface, and

$$T = e^{-\gamma d} \quad (3.11)$$

Z_{sn} and γ are the normalized characteristic impedance and the propagation constant of the metamaterial sample, respectively. These parameters can be related to relative permeability $\mu = \mu' - j\mu''$ and relative permittivity $\epsilon = \epsilon' - j\epsilon''$ as follows:

$$\gamma = \gamma_0 \sqrt{\mu\epsilon} \quad (3.12)$$

and

$$Z_{sn} = \sqrt{\frac{\mu}{\epsilon}} \quad (3.13)$$

where $\gamma_0 = j2\pi / \lambda_0$ is the propagation constant of free space and λ_0 is the free space wavelength.

Using (3.8) and (3.9), Γ and T can be expressed in terms of S parameters as follows:

$$\Gamma = K \pm \sqrt{K^2 - 1} \quad (3.14)$$

where

$$K = \frac{S_{11}^2 - S_{21}^2 + 1}{2S_{11}} \quad (3.15)$$

and

$$T = \left(\frac{S_{11} + S_{21} - \Gamma}{1 - (S_{11} + S_{21})\Gamma} \right) \quad (3.16)$$

In Equation (3.14), there is an ambiguity with the plus or minus sign. The sign is chosen such that $|\Gamma| < 1$. Using (3.11), one can obtain the complex propagation constant as

$$\gamma = \frac{\left[\ln\left(\frac{1}{T}\right) \right]}{d} \quad (3.17)$$

From (3.10) and (3.13), we can get

$$\sqrt{\frac{\mu}{\epsilon}} = \left(\frac{1 + \Gamma}{1 - \Gamma} \right) \quad (3.18)$$

and from (3.12) and (3.18), expressions for ϵ and μ follows as

$$\epsilon = \frac{\gamma}{\gamma_0} \left(\frac{1 - \Gamma}{1 + \Gamma} \right) \quad (3.19)$$

$$\mu = \frac{\gamma}{\gamma_0} \left(\frac{1 + \Gamma}{1 - \Gamma} \right) \quad (3.20)$$

As the parameter T in 3.17 is a complex number, γ may assume multiple values. If T is defined as

$$T = |T|e^{j\phi} \quad (3.21)$$

then, γ is given by

$$\gamma = \frac{\left[\ln \left(\frac{1}{|T|} \right) \right]}{d} + j \left[\frac{2\pi n - \phi}{d} \right] \quad (3.22)$$

where $n = 0, \pm 1, \pm 2, \dots$

For most cases (where $d < \lambda_m$) n is set to 0. In some cases, d may be greater than λ_m . In that case, the ambiguity on the choice of n can be solved by taking two measurement on two different sample thicknesses d .

Using the procedure given above, the real and imaginary parts of μ_{eff} and ϵ_{eff} are plotted in Figure 3.18 to demonstrate that the suggested DSRR with conducting strip structure has simultaneously negative permittivity and negative permeability over the frequency band from 5.05 GHz to 5.64 GHz. In other words, the suggested DSRR resonator topology is also useful to design a left handed metamaterial, if needed.

3.7 Alternative Topologies for Electrically-Small Magnetic Resonator Type Metamaterial Design

As discussed previously, having electrically-small unit cell is a necessity in metamaterial design. Furthermore, design of smaller size devices may be advantageous in many applications in the RF range. Therefore, the search for alternative topologies to design electrically-small metamaterial unit cells has been popular in recent years.

The effects of ring number (N) on the resonance frequency f_0 and on the electrical size (u) have already been investigated for multiple split-ring resonators (MSRR) and for spiral res-

onators (SR) [15, 20]. In this dissertation, in addition to effects of N , the effects of “doubling the metamaterial structure” (i.e., making the resonator structures as double-sided by printing metal inclusions on both sides of the substrate) on f_0 and u are also investigated. For this purpose, the MSRR, double-sided MSRR (DMSRR), SR, double-sided SR (DSR), U-spiral resonator (USR) and double-sided USR (DUSR) structures are examined.

3.7.1 Design and Simulations

Figure 3.19 shows the top views of the resonator structures that will be studied in this subsection. These structures are MSRR, DMSRR, SR, DSR, USR, and DUSR type resonators having turn numbers, $N > 2$, in general. In double-sided structures, the basic conducting strip patterns (i.e. the conventional SRR, SR, USR patterns) are printed on both faces of the substrate such that the patterns on the back face are the 180 degrees rotated version of those on the front page. In Figure 3.20, a perspective view for the DSR structure is shown as an example for a better visualization. For fair comparison, the geometrical parameters of all these resonators are chosen to be same the same or very similar such that, within a unit cell, they all have the same copper strip width $w = 0.1$ mm, the same gap width $g = 0.1$ mm, and the same unit cell side length $l = 8$ mm. The common substrate used in all three structures has the relative permittivity $\epsilon_r = 2$, dielectric loss tangent $\tan \delta_c = 0.0009$, and substrate thickness $t_{subs} = 0.254$ mm.

The same simulation setup is used in the Ansoft HFSS software to compute the scattering parameters of each type of N -turn resonator arrays. In the simulation setup, the unit cell is surrounded by an air medium as seen in Figure 3.20 where the directions of the \vec{E} , \vec{H} , and \vec{k} vectors of the excitation are also shown. Perfect electric conductor BCs are applied at the boundaries perpendicular to y axis and perfect magnetic conductor BCs are applied at the boundaries perpendicular to the z axis [16, 67, 114]. Different values of $N \geq 2$ are considered in simulations. The maximum N chosen for MSRR and DMSRR simulations is 8 as allowed by the memory capacity of the computer used in simulations. The maximum ring number $N = 6$ is used in the simulations for the SR, USR, DSR, and DUSR structures for the same reason. In simulations, to improve the computational speed and provide some memory reduction, thickness of the copper lines are chosen to be zero for all structures under investigation. It is

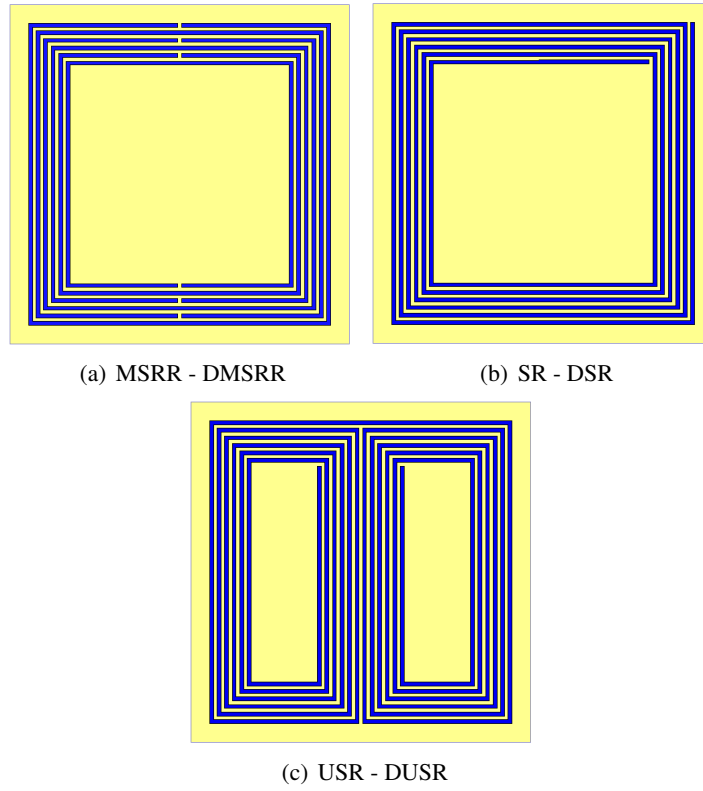


Figure 3.19: Top views of single- and double-sided structures with $N = 6$.

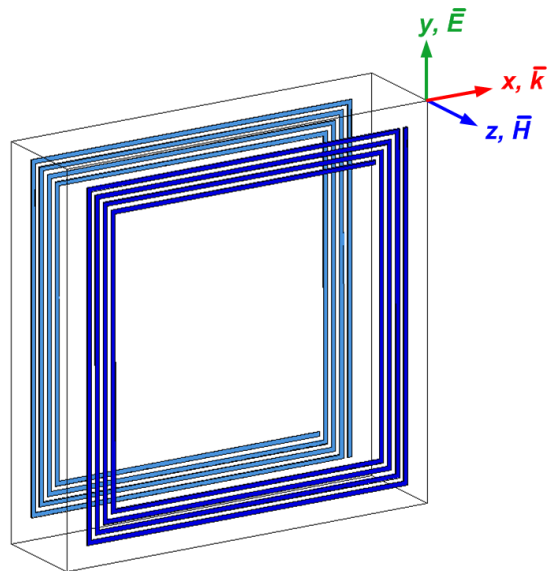


Figure 3.20: Directions of vector fields on the DSR structure.

important to note here that, setting the copper line thickness to zero does not effect the results significantly. Simulation results for resonators with various N numbers are obtained and from the minimum points of the $|S_{21}|$ spectra, the resonance frequency values, f_0 are determined for all resonator topologies. Then, using the formula, $u = D / \lambda_0$, we can find the electrical size (u) of a given structure. Herein, D is the maximum linear dimension of the structure and λ_0 is the wavelength at f_0 [15].

3.7.2 Results and Discussions

The simulation results obtained by the CST Microwave Studio software as well as the experimental results were already reported in [15] for MSRR and SR structures which have the same design parameters as we used in this section. Since we used a different software, Ansoft HFSS, for the simulations, we first validated our own simulation results for the MSRR and SR structures as shown in Tables 3.3 and 3.4; and in Figures 3.21 and 3.22. Our results are found in very good agreement with the results given in [15].

Table 3.3: Resonance frequency and electrical size for N -ring MSRR topologies.

N	MSRR f_0 [GHz] - u Experimental (Ref. [15])	MSRR f_0 [GHz] - u CST (Ref. [15])	MSRR f_0 [GHz] - u HFSS (this study)
2	$2.27 - \lambda_0 / 12$	$2.20 - \lambda_0 / 12$	$2.24 - \lambda_0 / 12$
3	$1.98 - \lambda_0 / 13$	$1.94 - \lambda_0 / 14$	$1.94 - \lambda_0 / 14$
4	$1.79 - \lambda_0 / 15$	$1.74 - \lambda_0 / 15$	$1.80 - \lambda_0 / 15$
6	$1.65 - \lambda_0 / 16$	$1.58 - \lambda_0 / 17$	$1.68 - \lambda_0 / 16$
8	$1.61 - \lambda_0 / 16$	$1.53 - \lambda_0 / 17$	$1.60 - \lambda_0 / 17$

Table 3.4: Resonance frequency and electrical size for N -ring SR topologies.

N	SR f_0 [GHz] - u Exp. (Ref. [15])	SR f_0 [GHz] - u CST (Ref. [15])	SR f_0 [GHz] - u HFSS (this study)
2	$1.13 - \lambda_0 / 23$	$1.13 - \lambda_0 / 23$	$1.12 - \lambda_0 / 24$
3	$0.76 - \lambda_0 / 35$	$0.73 - \lambda_0 / 36$	$0.76 - \lambda_0 / 35$
4	$0.60 - \lambda_0 / 44$	$0.58 - \lambda_0 / 46$	$0.60 - \lambda_0 / 44$
6	$0.45 - \lambda_0 / 59$	$0.45 - \lambda_0 / 59$	$0.42 - \lambda_0 / 63$

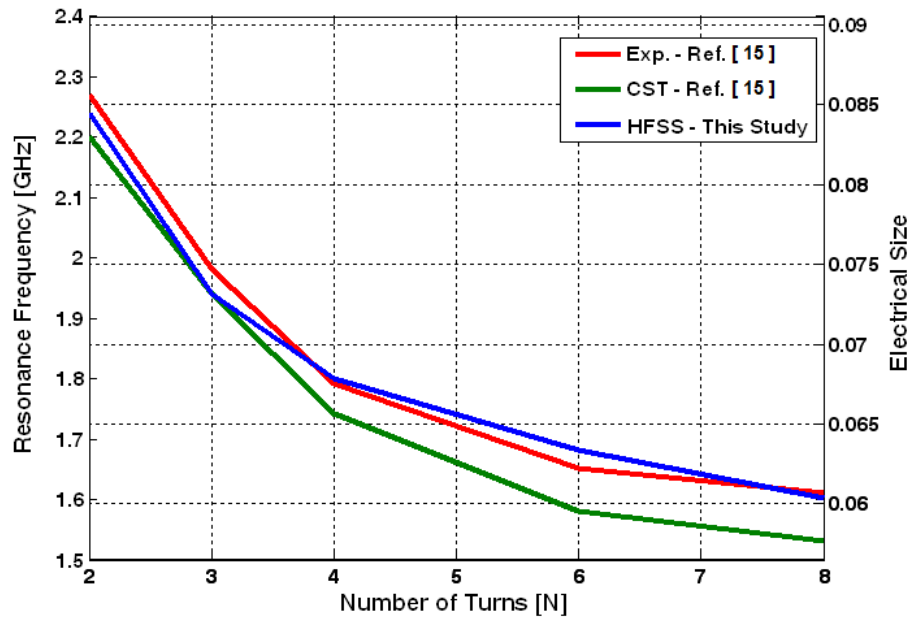


Figure 3.21: Resonance frequency and electrical size for N -ring MSRR topologies.

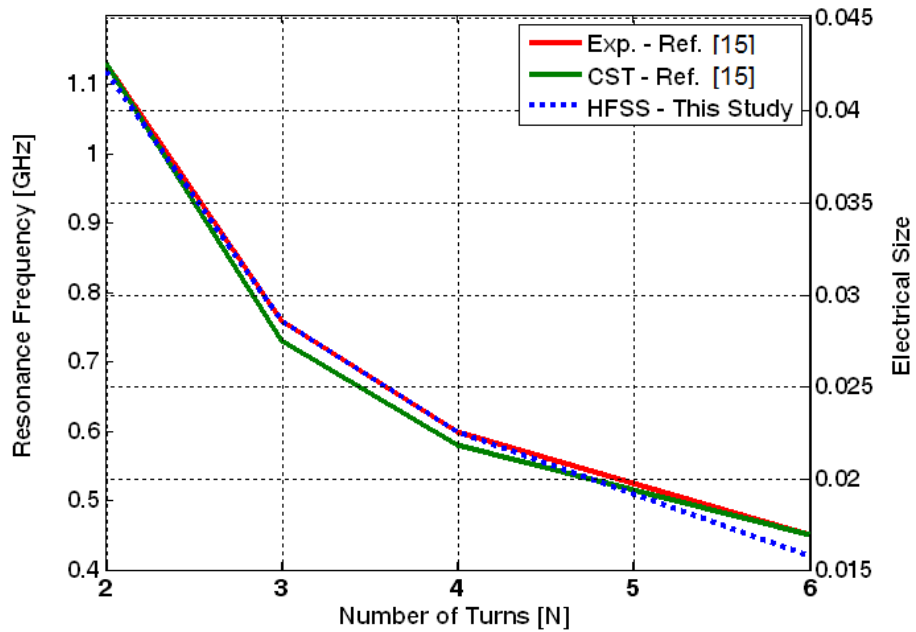


Figure 3.22: Resonance frequency and electrical size for N -ring SR topologies.

Table 3.5: Resonance frequency and electrical size values for N -ring MSRR and Double-Sided MSRR (DMSRR) Topologies.

N	MSRR	DMSRR
	f_0 [GHz] - u HFSS	f_0 [GHz] - u HFSS
2	$2.24 - \lambda_0 / 12$	$1.66 - \lambda_0 / 16$
3	$1.94 - \lambda_0 / 14$	$1.44 - \lambda_0 / 19$
4	$1.80 - \lambda_0 / 15$	$1.34 - \lambda_0 / 20$
6	$1.68 - \lambda_0 / 16$	$1.24 - \lambda_0 / 21$
8	$1.60 - \lambda_0 / 17$	$1.18 - \lambda_0 / 22$

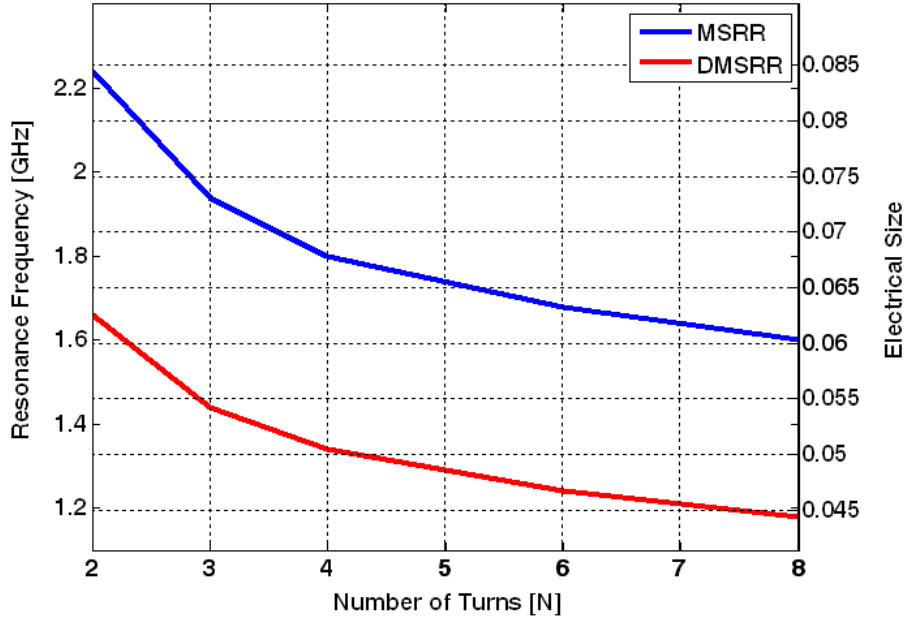


Figure 3.23: Resonance frequency and electrical size values for N -ring MSRR and Double-Sided MSRR (DMSRR) Topologies.

Table 3.6: Resonance frequency and electrical size values for the N -ring SR, USR topologies and their double-sided versions, DSR and DUSR topologies.

N	SR	USR	DSR	DUSR
	f_0 [GHz] - u HFSS	f_0 [GHz] - u HFSS	f_0 [GHz] - u HFSS	f_0 [GHz] - u HFSS
2	$1.12 - \lambda_0 / 24$	$1.12 - \lambda_0 / 24$	$0.80 - \lambda_0 / 33$	$0.64 - \lambda_0 / 41$
3	$0.76 - \lambda_0 / 35$	$0.84 - \lambda_0 / 32$	$0.50 - \lambda_0 / 53$	$0.42 - \lambda_0 / 63$
4	$0.60 - \lambda_0 / 44$	$0.70 - \lambda_0 / 38$	$0.32 - \lambda_0 / 83$	$0.30 - \lambda_0 / 88$
6	$0.42 - \lambda_0 / 63$	$0.58 - \lambda_0 / 46$	$0.22 - \lambda_0 / 121$	$0.20 - \lambda_0 / 133$

Using the design parameters specified in subsection 3.7.1, the electrical size for a six-turn MSRR is calculated to be $\lambda_0 / 17$ while it is calculated to be $\lambda_0 / 63$ for a six-turn SR. As shown

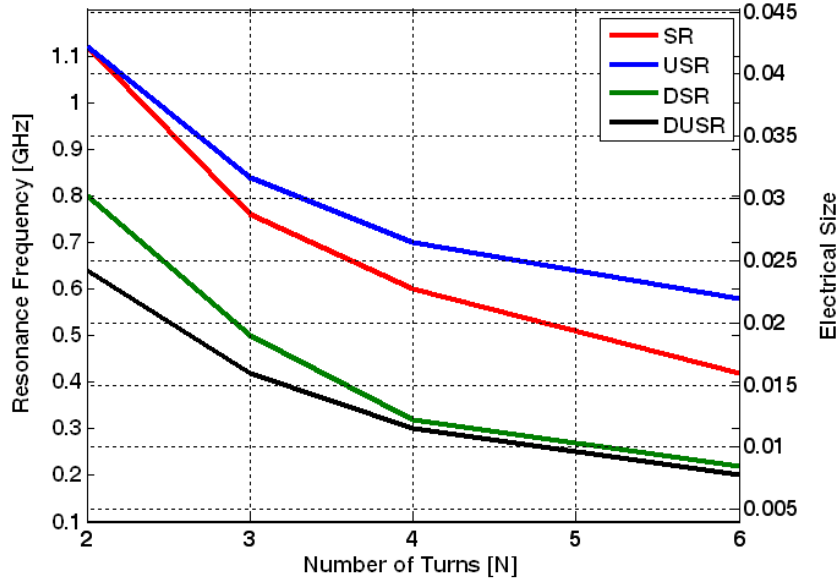


Figure 3.24: Resonance frequency and electrical size values for the N -ring SR, USR topologies and their double-sided versions, DSR and DUSR topologies.

in Table 3.5 and Figure 3.23, doubling a six-turn MSRR reduces the resonance frequency from 1.68 to 1.24 GHz, and hence reduces the electrical size from $\lambda_0 / 16$ to $\lambda_0 / 21$. On the other hand, the effect of doubling is more pronounced in the SR structure. For example, Table 3.6 and Figure 3.24 show that doubling a six-turn SR reduces f_0 from 0.42 to 0.22 GHz, and changes u from $\lambda_0 / 63$ to $\lambda_0 / 121$. As the alternatives of SR and DSR, we also investigated the USR and double USR (DUSR) structures. Table 3.6 and Figure 3.24 show that six-turn DSR has an electrical size of $\lambda_0 / 121$, however for the six-turn DUSR the electrical size drops to $\lambda_0 / 133$. We should note here that, the f_0 (and hence u) of SR is lower than those of USR having the same N . However, this relation between DSR and DUSR is just the opposite. In fact, this is not surprising, because doubling these structures produces a dominant distributed capacitance effect which increases by the overlapping conducting strip area just as in parallel plate capacitors. As the overlapping conducting strip area in DUSR is much greater than that of DSR, the DUSR becomes electrically smaller than DSR.

CHAPTER 4

NOVEL TUNABLE AND MULTI-BAND METAMATERIAL DESIGNS

4.1 Introduction

As the first novel metamaterial design of this chapter, we suggest a multiple split ring resonator topology that provides not only multi-band operation at two or more resonance frequencies but also lends itself to adaptive tuning. As the first step of this approach, a uniform array of identical micro-split SRR (MSSRR) cells is designed and fabricated such that each MSSRR cell has N pairs of very narrow (in the order of tens of micrometers for X-band designs) additional splits etched on both sides of the main split along the external ring. A maximum possible resonance frequency f_N is realized with this homogeneous array because the equivalent capacitance of each unit cell is minimized due to the series capacitances introduced by each micro-split. Since the gap width of the additional micro-splits (g_{ms}) is designed to be much smaller than the width of the main split (g), their “ON/OFF” states can be conveniently changed by electrostatically actuated RF MEMS switches [28, 95] that should be implemented during the fabrication of the MSSRR array. If all of the micro-splits in the array are closed by setting the MEMS switches to their “ON” state, a homogeneous array of traditional SRRs (having their main gaps only) is obtained providing the minimum available resonance frequency f_1 . In principle, any combination out of N possible resonance frequencies f_1, f_2, \dots, f_N can be realized by controlling the switching states associated with the micro-splits in properly chosen columns of the MSSRR array. The maximum value of N is basically limited by the condition that the dimensions of the composite unit cell (formed as a collection of N individual MSSRR cells) must be a small fraction of the wavelength even at the highest resonance frequency. In the case of $N = 3$ for instance, the single and multi-band

operations having the sets of resonance frequencies $\{f_1\}$, $\{f_2\}$, $\{f_3\}$, $\{f_1, f_2\}$, $\{f_1, f_3\}$, $\{f_2, f_3\}$ and $\{f_1, f_2, f_3\}$ can be provided by a single MSSRR array topology. In addition to demonstrating the possibility of actual multi-band operation in inhomogeneous MSSRR arrays, another contribution of this work is to suggest a feasible approach for adaptive tuning of the MSSRR arrays based on the well established MEMS technology. As the actual implementation of RF MEMS switches in large MSSRR arrays has not been accomplished yet, we have followed a proof-of-concept approach and printed copper strips across the micro-splits to simulate the “ON” states of the ideal switches both in our numerical simulations and experiments [23].

At this point, we need to emphasize a few important issues to clarify the original aspects of this multi-band metamaterial design. First of all, controlling the resonance frequency of an SRR by using additional distributed gaps is a well known approach studied in various papers [63, 68, 69, 130, 131]. In most of those studies, however, multiple gaps of equal widths have been employed leading to very large increase in resonance frequency. For example, resonance frequencies of the single-gap, double-gap and four-gap SRR (single ring) cells are reported to be about 4.5 GHz, 8 GHz and 13 GHz, respectively in [63]. On the other hand, use of conventional SRR cells (without any additional small splits) with varying main gap widths was suggested but not found as a proper solution due to the following reasons: Varying the width of the main gap produces quite small changes in resonance frequency (for example, an increase from 3.6 GHz to 3.8 GHz is reported in [63] for a change of gap width from 0.2 mm to 0.5 mm), and closing the one and only gap of an SRR cell by a switching mechanism (for the purpose of adaptive tuning) completely annihilates the associated resonance. Controlling the state of the main gap by a single RF MEMS switch operating as a varactor could be another alternative but this approach is not considered to be useful either as this method is known to provide only a small range of frequency tuning [132]. Therefore, to obtain intermediate size shifts (about one GHz in X-band, for instance) in resonance frequency, it is found that the combination of a main gap and a number of narrower gaps in the outer ring of an SRR cell is definitely more useful. Also, adaptive control of the states of such narrower micro-gaps is known to be easier with technologies like MEMS switching.

Secondly, metamaterial design studies with dual-band operation are already reported [133, 134] in THz and near-infrared regions. Each of these recent studies successfully demonstrates the realization of two distinct operational bandwidths using an array of composite-cells which are composed of two individual resonators of different physical dimensions and hence they

have different resonance frequencies. However, the dual-band metamaterial topologies reported in these references are not suitable for adaptive frequency tuning as their resonance frequencies are fixed permanently during the fabrication process. In the suggested design, on the other hand, the composite unit cells are composed of two or more micro-split SRR cells whose resonance frequencies can be externally adjusted after the fabrication of the metamaterial array by means of suitable switching techniques.

Finally, the suggested MSSRR-based multi-band metamaterial design approach is expected to be still useful in millimeter wave and terahertz regions with proper scaling of the unit cell dimensions. As the wavelength gets smaller, the geometrical shapes of these sub-wavelength structures should be made simpler for easier fabrication. Single ring SRR unit cells with additional nano-splits may be suitable at higher frequencies. Nano-switching techniques [135] would possibly be needed to control the switching states of nano-splits if adaptive tunability is required.

4.2 A Tunable Multi-Band Metamaterial Design Using Micro-Split SRR Arrays

4.2.1 Design

The schematic representations of the unit cells proposed in this micro-split SRR design are given in Figure 4.1. A conventional SRR structure (unit cell A), an SRR with two additional micro-splits (unit cell B) and an SRR with four additional micro-splits (unit cell C) are demonstrated in parts (a), (b) and (c) of Figure 4.1, respectively. All these square shaped unit cells have the same side length $l = 2.8$ mm, main split width $g = 0.3$ mm, metal strip width $w = 0.3$ mm and inner/outer strip separation length $s = 0.3$ mm. For the unit cell B, the additional design parameters shown in Figure 4.1(b) are chosen to be $l_1 = 0.85$ mm, $l_2 = 0.35$ mm and $l_3 = 1.25$ mm. Similarly for the unit cell C, the additional design parameters are chosen as $l_1 = 0.45$ mm, $l_2 = 0.35$ mm, $l_3 = 0.35$ mm and $l_4 = 1.25$ mm. The width of each additional micro-split gap (g_{ms}) is set to be $50 \mu\text{m}$.

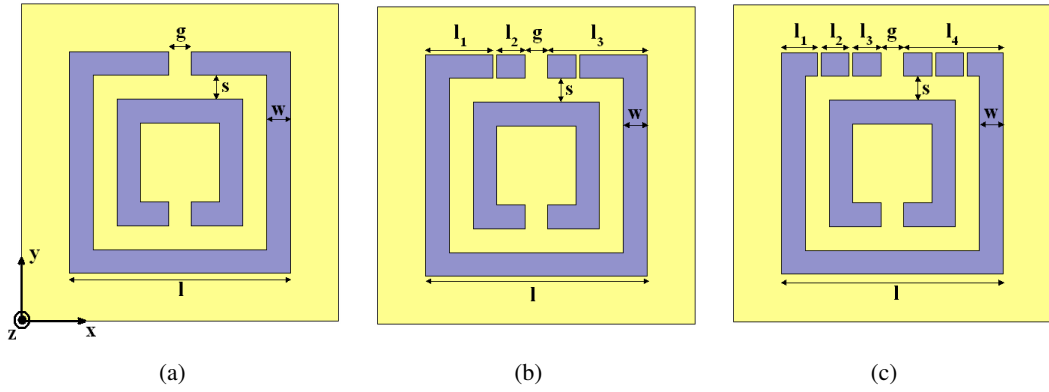


Figure 4.1: Schematic views of (a) unit cell A, (b) unit cell B, (c) unit cell C

4.2.2 Fabrication

The type A, type B, and type C MSSRR magnetic resonator unit cells and their arrays are fabricated at Middle East Technical University (METU) MEMS Center Fabrication Facilities with $100 \text{ \AA}/0.5 \mu\text{m}$ Ti/Au patterned lithography on a 4 inch glass substrate having a thickness of $500 \mu\text{m}$, relative permittivity of 4.6 and loss tangent of 0.01. The unit cell structures are diced from glass substrate to obtain a total unit cell dimension of $4 \text{ mm} \times 4 \text{ mm}$ including the blank glass areas outside the borders of the SRRs. While Figure 4.2 is showing the wafer mask layout for the fabrication, Figures 4.3 and 4.4 are showing the pictures for dicing instructions. In other words, Figures 4.3 and 4.4 describe the operator how to dice the glass wafer into pieces in order to obtain the final forms of the designed metamaterial structures. In these figures, part 1A contains 2×2 homogeneous/inhomogeneous super cells consist of square shaped unit cells having 5 mm side length, part 1B again contains 2×2 homogeneous/inhomogeneous super cells consist of square shaped unit cells having 4 mm side length, parts 2A and 2B contains both 2×2 and 3×2 homogeneous/inhomogeneous super cells consist of square shaped unit cells having 4 mm side length, finally parts 3A and 3B consists of only unit cells having 5 mm and 4 mm side lengths, respectively. Besides, the remaining 10×10 SRR array in the middle of the wafer mask layout in Figure 4.3 is type A SRR array with 4 mm unit cell side length. In this part of dissertation we make use of only the structures shown in parts 1B, 2A, and 3B. The remaining parts will be used in another study. For the sake of faster process and saving money, the metamaterial designs for two different projects have been fabricated at once on the same wafer.

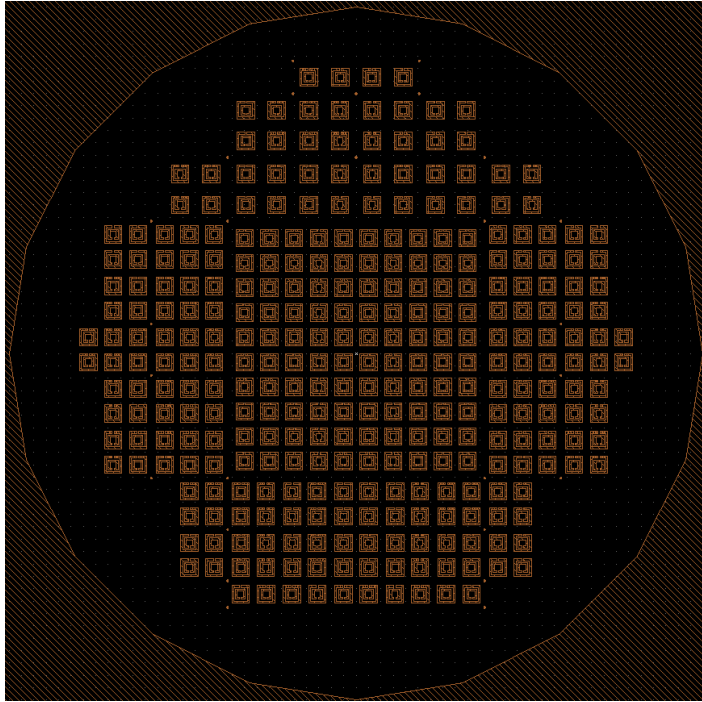


Figure 4.2: Wafer mask layout for fabrication.

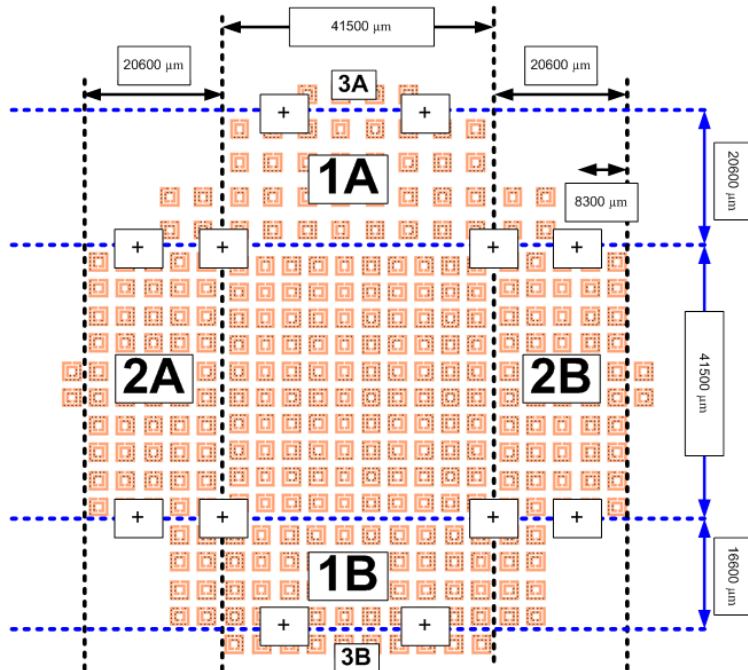


Figure 4.3: Dicing instructions for main pieces.

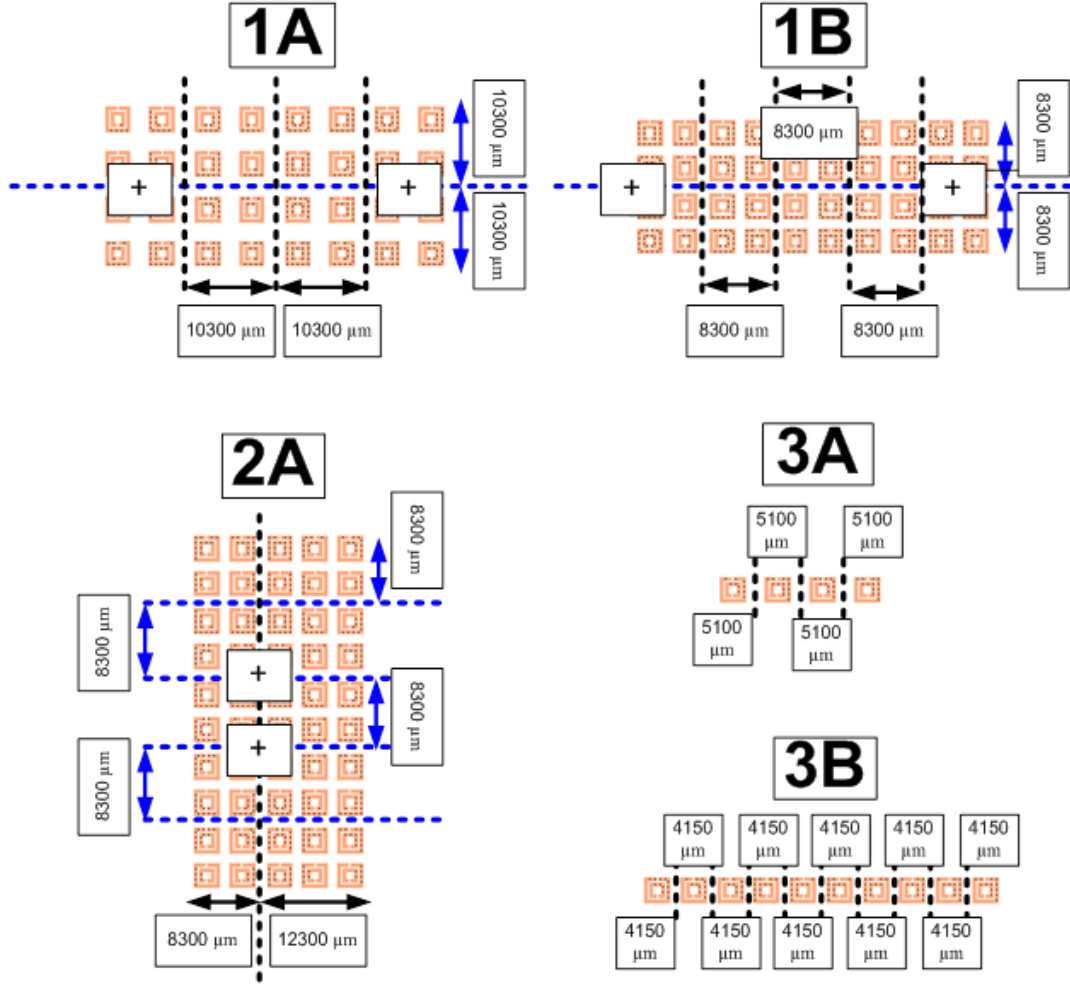


Figure 4.4: Dicing instructions for sub-pieces.

4.2.3 Simulations and Experiments

4.2.3.1 Simulations

The transmission and reflection spectra (i.e. S_{21} and S_{11}) of all homogeneous and inhomogeneous metamaterial arrays composed of type A, type B, and type C unit cells numerically simulated using the Ansoft HFSS software. Exactly the same set of geometrical and material parameters are used in both numerical simulations and in fabrication of the sample structures. Furthermore, the experimental measurement setup that will be described in Section 4.2.3.2 is identically simulated in HFSS simulations for a fair comparison of numerical and experimen-

tal results. Accordingly, planar faces of the computational volume, which are perpendicular to both y and z axes, are modeled to be perfect electric conductor (PEC) boundaries as they represent the metallic walls of the rectangular waveguide shown in Figure 4.5. The faces perpendicular to the x axis are modeled as the input/output ports of the waveguide. The sample metamaterial structures placed in the X-band waveguide setup are excited by TE_{10} mode.

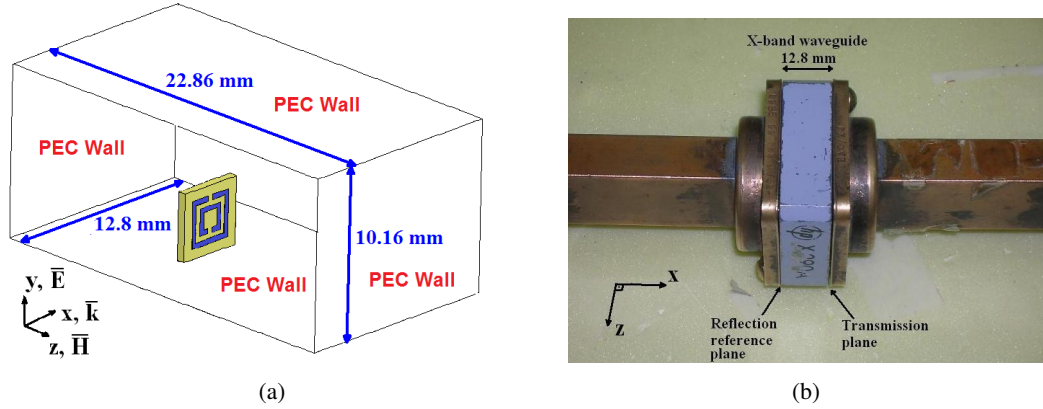


Figure 4.5: (a) Schematic of simulation and experimental setup, (photograph of experimental setup.)

4.2.3.2 Experiments

In this study, the measurements are performed by using Agilent 8720D vector network analyzer using through, reflect, line (TRL) calibration. The picture of the 8720D network analyzer is given in 4.6. For the characterization of transmission, the sample structure under investigation is placed in the middle of a rectangular air-filled X-band waveguide having the dimensions of $22.86 \text{ mm} \times 10.16 \text{ mm} \times 12.8 \text{ mm}$ as shown in Figure 4.5(a). The experimental results are measured over the frequency range from 8 GHz to 12 GHz. While the schematic demonstration of the experimental/simulation setup is given in Figure 4.5(a), a photograph of the actual experimental setup is shown in Figure 4.5(b).

4.2.4 Results

In this section, we report detailed experimental and numerical results for some SRR and MSSRR arrays to demonstrate the multi-band operation property of inhomogeneous MSSRR



Figure 4.6: Agilent 8720D vector network analyzer

arrays and the feasibility for their adaptive tuning. For this purpose, we mainly observe the transmission characteristics (i.e. magnitude of S_{21} scattering parameter spectra) of periodic array structures composed of MSSRR unit cells.

4.2.4.1 Single Layer Homogeneous SRR and MSSRR Arrays

In this sub-section, we investigate the transmission characteristics of homogeneous meta-material arrays which composed of only one layer of SRR or MSSRR unit cells along the propagation direction. Transmission characteristics as well as the photographs of the fabricated unit cells A, B and C are given in Figures 4.7, 4.8 and 4.9, respectively. Experimental results show that while the type A structure resonates at 9.48 GHz, the type B and type C structures resonate at 10.58 and 11.41 GHz, respectively. These results demonstrate that there is an appreciable shift in the resonance frequency (about 11.6 % for the type B structure and about 20.4 % for the type C structure with respect to the type A structure) due to the series capacitance effects caused by additional micro-splits [23, 131]. Herein, the simulation results show good agreement with the measurements.

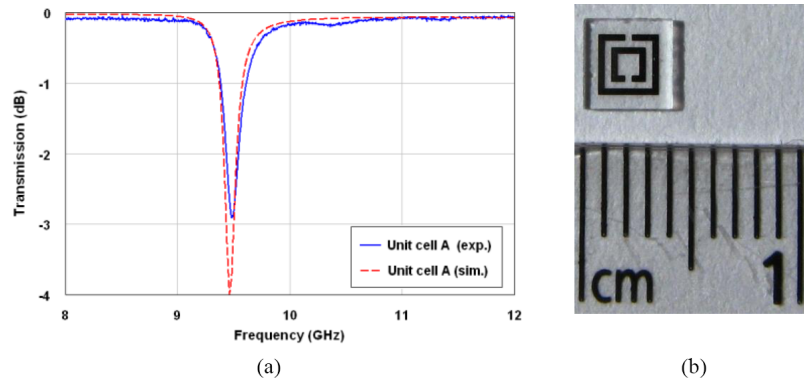


Figure 4.7: (a) Transmission characteristics of the type A SRR array. (b) Photograph of the actual resonator's unit cell.

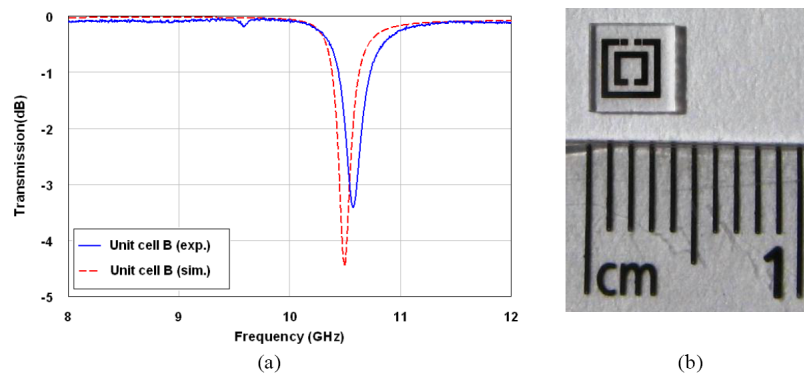


Figure 4.8: (a) Transmission characteristics of the type B MSSRR array. (b) Photograph of the actual resonator's unit cell.

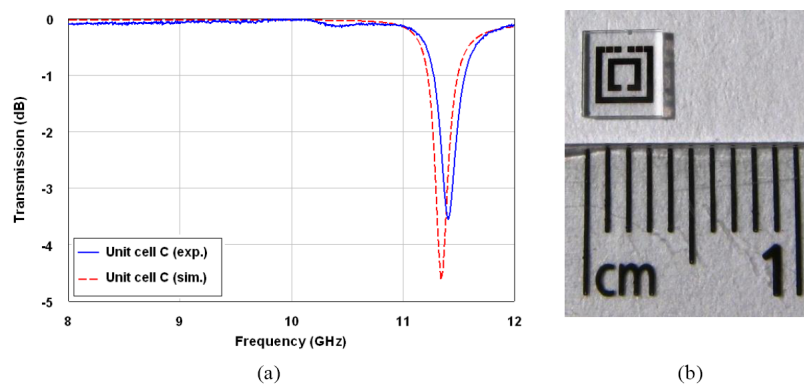


Figure 4.9: (a) Transmission characteristics of the type C MSSRR array. (b) Photograph of the actual resonator's unit cell.

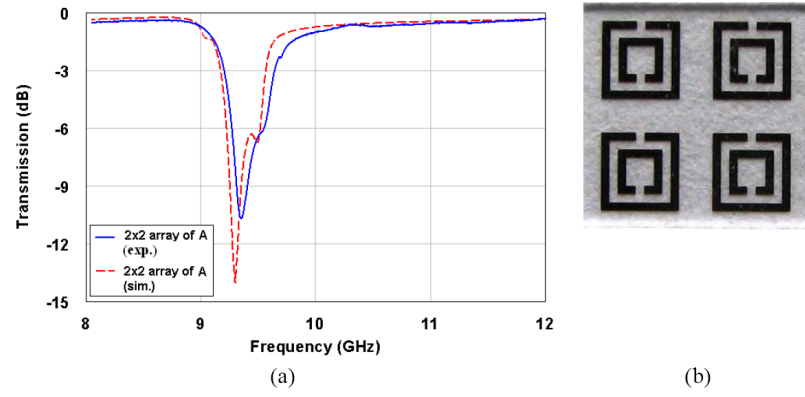


Figure 4.10: (a) Transmission characteristics of the resonator array composed of 2×2 super cells having type A unit cells. (b) Photograph of the actual resonator's super cell.

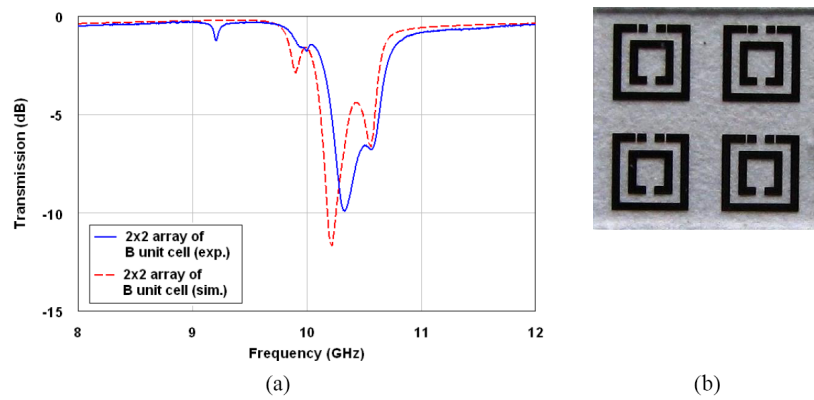


Figure 4.11: (a) Transmission characteristics of the resonator array composed of 2×2 super cells having type B unit cells. (b) Photograph of the actual resonator's super cell.

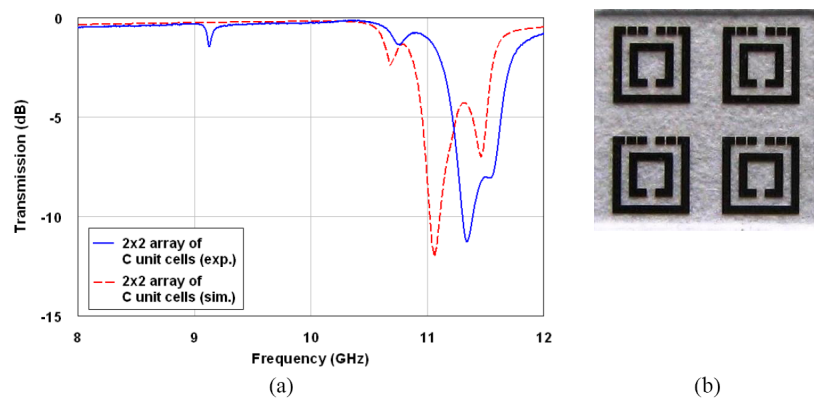


Figure 4.12: (a) Transmission characteristics of the resonator array composed of 2×2 super cells having type C unit cells. (b) Photograph of the actual resonator's super cell.

4.2.4.2 Dual-Layer Homogeneous Super Cell Arrays of SRRs or MSSRRs

In this subsection, we investigate the transmission characteristics of arrays formed by small-sized homogeneous super cell SRR or MSSRR arrays. Transmission characteristics and the photographs of 2×2 homogeneous super cell arrays, which consist of only one type of unit cells (either A, or B, or C) are given in Figures 4.10, 4.11 and 4.12, respectively. In these structures, we have two layers of unit cells along the propagation direction. It is important to emphasize that each super cell array structure is found to resonate in the vicinity of the resonance frequency of the corresponding unit cell array. However, unlike the unit cell arrays, these homogeneous super cell arrays display two resonance frequencies close to each other. This behavior can be explained by the strong coupling effects between neighboring unit cells along the propagation direction as also discussed in [131]. Moreover, a wider stop bandwidth and a lower transmission minimum occur in the transmission characteristics of these array structures.

4.2.4.3 Double-Layer and Triple-Layer Inhomogeneous Super Cell Arrays of SRRs and MSSRRs

In this sub-section, we investigate the transmission characteristics of metamaterial arrays composed of three different inhomogeneous super cell arrays of SRRs and MSSRRs, which display dual-band and triple-band operations. The first super cell array consists of two unit cells of type B in the first column (layer) and two unit cells of type A in the second column (layer) in the direction of propagation. The simulated and measured transmission characteristics for the resonator formed by this super cell are given in Figure 4.13(a) showing two distinct resonance frequencies; the lower one belongs to the pair of type A resonators and the higher one belongs to the type B resonators. The photograph of the super cell of this array is also given in Figure 4.13(b). Similarly, the second inhomogeneous super cell array shown in Figure 4.14 consists of two unit cells of type C in the first layer and two unit cells of type A in the second layer. Again, the simulated and measured transmission characteristics given in Figure 4.14(a) show two distinct resonance frequencies, one belongs to the pair of type A resonators and the other belongs to pair of type C resonators.

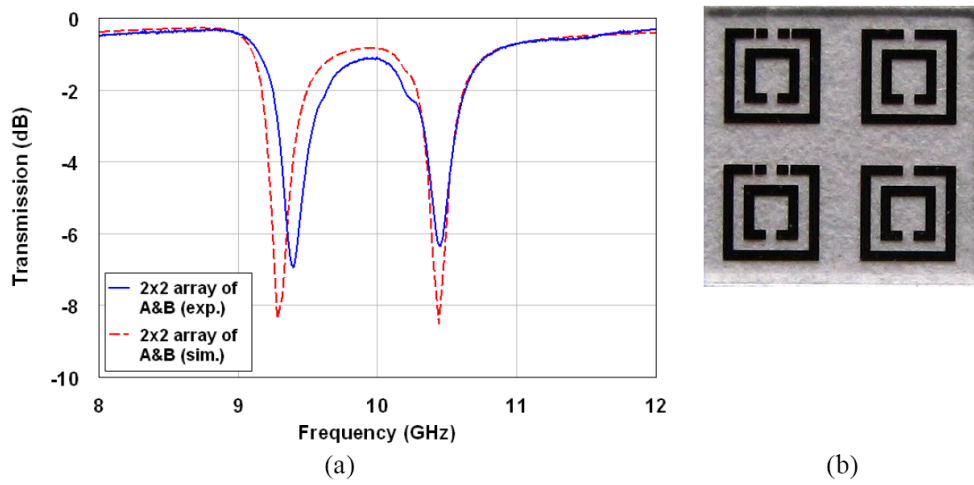


Figure 4.13: (a) Transmission characteristics of the dual band resonator array composed of 2×2 inhomogeneous super cells having type A (in column 2) and type B (in column 1) unit cells. (b) Photograph of the actual resonator's super cell.

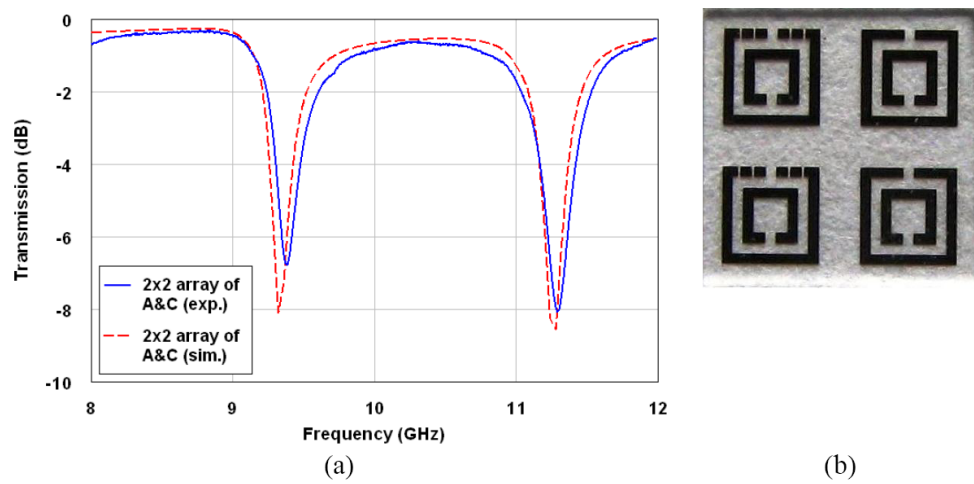


Figure 4.14: (a) Transmission characteristics of the dual band resonator array composed of 2×2 inhomogeneous super cells having type A (in column 2) and type B in (column 1) unit cells. (b) Photograph of the actual resonator's super cell.

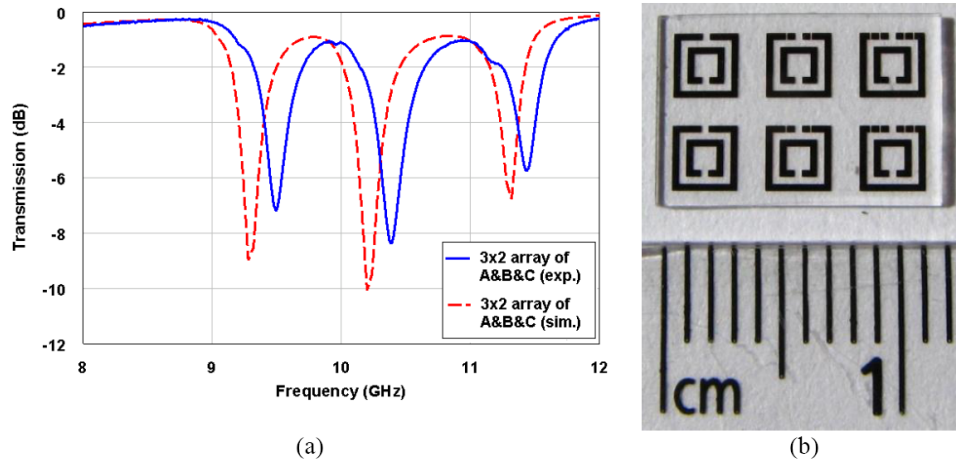


Figure 4.15: (a) Transmission characteristics of the triple-band resonator array of 3×2 inhomogeneous super cells having type A (in column 1), type B (in column 2) and type C (in column 3) unit cells. (b) Photograph of the actual resonator's super cell.

Lastly, we design and fabricate a 3×2 inhomogeneous super cell array which consists of type A (in column 1), type B (in column 2) and type C (in column 3) unit cells. Figure 4.15 shows the transmission characteristics and the photograph of this array. As expected, the transmission spectra shown in Figure 4.15(a) has three different resonant frequencies due to three different types of unit cells.

4.2.4.4 Switching for Adaptive Tuning of Multi-Band Operation

So far in this study, we have demonstrated the possibility of double-band and triple-band magnetic resonator operations using inhomogeneous micro-split SRR super cell arrays. Adaptive tuning of the resonance frequencies in such multi-band design applications is possible if the switching states of the micro-splits in the selected columns of the MSSRR arrays can be efficiently controlled. For better visualization, Figure 4.16 shows the schematic view of the switching representation for the unit cell C. Herein, S_1 , S_2 , S_3 , and S_4 are the switches that are placed across the micro-splits of the structure. It is clear that, the unit cell B can be realized for the closed-down states of the switches S_1 and S_4 , and also the unit cell A can be realized for the closed-down states of all four switches S_1 , S_2 , S_3 , and S_4 . In this paper, ideal closed-down switching states of the micro-splits are simulated by metalization for a simplified proof of concept. However, we intend to realize the suggested adaptively tunable MSSRR

design by using electrostatically actuated RF MEMS switches fabricated in the facilities of the METU MEMS Center [136] as a future work.

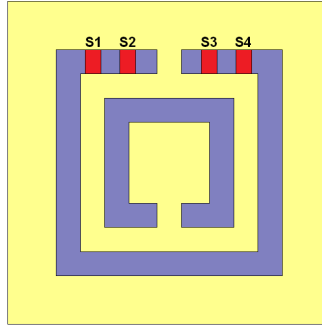


Figure 4.16: Schematic view of the switching representation for type C resonator.

4.2.5 An Alternative Triple-Band Metamaterial Design with Smaller Electrical Size

The 3×2 inhomogeneous super cell shown in Figure 4.15 provides a successful design for a triple-band magnetic resonator. However, the length of the resulting composite cell (composed of A, B and C type SRR cells) along the propagation direction is close to a half wavelength at the highest resonance frequency. Therefore, the interpretation of an array composed of such composite super cells as a homogeneous metamaterial medium is questionable. Certain techniques for better miniaturization could be applied to this composite cell design to shift its resonance frequencies to lower values while keeping the overall composite cell size the same. In literature, there are several useful studies on miniaturized metamaterial structures to provide a better effective medium approach. A simple and useful technique is to increase the dielectric constant of the substrate [13, 78]. Increasing the relative permittivity of the substrate increases the total effective capacitance, hence decreases the resonance frequency and the electrical size of the structure. Another approach proposes the use of broad-side coupling for miniaturization purpose [13, 16, 18] as it is also addressed in Chapter 3 of this dissertation. Lastly, increasing the number of internal rings in multiple SRR and double-sided multiple SRR unit cells becomes quite useful to obtain miniaturized metamaterial structures [15, 16, 20]. This approach is also discussed in Chapter 3.

Although the above mentioned techniques are valid and applicable to our composite unit cell structure shown in Figure 4.15(b), we can still propose an alternative composite cell arrange-

ment with reduced physical dimensions. Figure 4.17 shows the schematic representation and dimensions for this new composite unit cell. Herein, type A, type B, and type C structures are positioned along the z direction to form a composite cubic cell, with the side length of 4 mm. The magnitude and phase spectra of the complex scattering parameters S_{21} and S_{11} (simulated by HFSS using the previously specified design parameters and the waveguide setup shown in Figure 4.5) are plotted in Figure 4.18(a) and Figure 4.18(b), respectively, for this new composite cell. Locations of the transmission minima seen in Figure 4.18(a) reveals that this alternative structure provides a triple-band operation at almost the same resonance frequencies as the electrically larger unit cell described earlier. In conclusion, the electrical size of this new three-band composite cell is one third of the electrical size of the former three-band design. The ratio of the maximum physical cell dimension to the wavelength at the highest frequency is close to seven. Hence, retrieval of the effective medium parameters (ϵ_{eff}) and (μ_{eff}) from the complex scattering parameters [35] is meaningful. Real and imaginary parts of the effective permittivity and the effective permeability are plotted in Figure 4.19(a) and Figure 4.19(b), respectively. Real part of the effective permittivity stays in positive values while the real part of the effective permeability becomes negative at the resonance frequencies, as expected.

4.3 Single Loop Resonator: A Novel Dual-Band Magnetic Metamaterial Structure

Recently, dual-band [86, 133, 134] and multi-band [23] metamaterials with negative permeability values are reported in literature by using combinations of two or more different metamaterial unit cells. The single loop resonator (SLR) structure introduced in this part of the dissertation, on the other hand, provides three closely located resonance frequencies in the X-band without the use of any composite cell topology. As the name implies, the SLR unit cell is made of a single loop of conducting strip printed over a dielectric substrate with the special winding geometry shown in Figure 4.20. Complex scattering parameters (S -parameters) and hence the reflection and transmission spectra of this SLR topology are numerically computed using both Ansoft HFSS software and CST Microwave Studio (MWS) software, which make use of different numerical methods to obtain full-wave electromagnetic solutions. Fig-

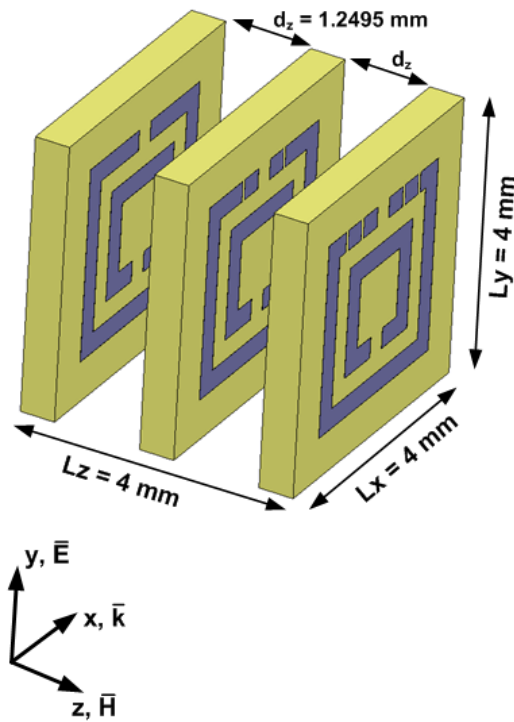


Figure 4.17: Schematic representation and dimensions for the alternative electrically small composite unit cell providing three-band operation.

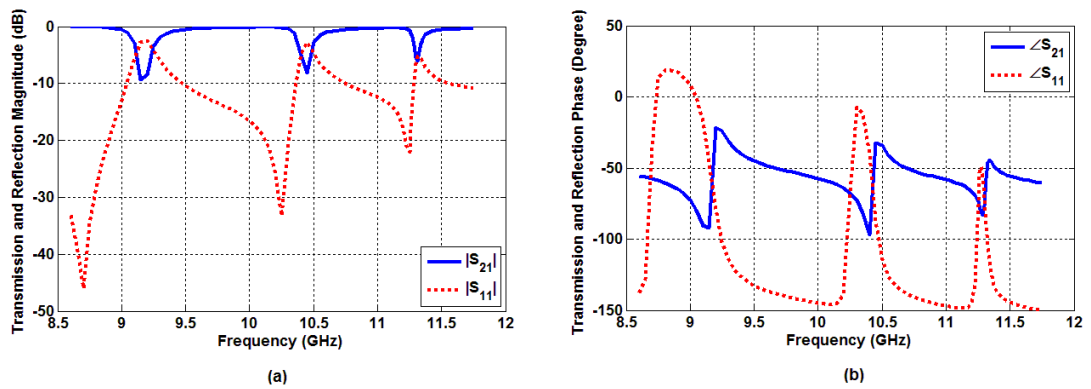


Figure 4.18: Transmission and reflection characteristics for the composite cell shown in Figure 4.17. (a) Magnitude plots, (b) phase plots.

Figure 4.21 shows the simulation setup to obtain complex S -parameters. These S -parameters are needed not only for estimating the resonance frequencies of this novel structure but also for the retrieval of the associated effective medium parameters μ_{eff} and ϵ_{eff} .

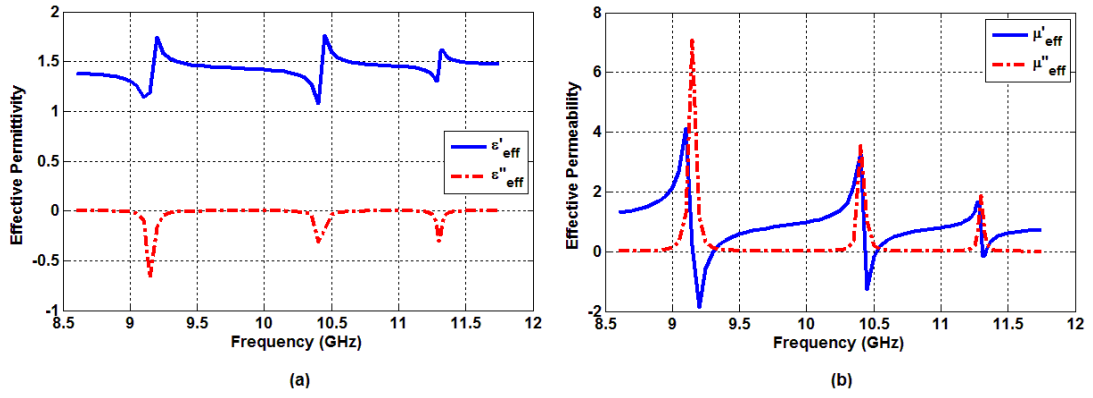


Figure 4.19: Effective medium parameters for the metamaterial resonator array composed of the composite cell shown in Figure 4.17 using $e^{j\omega t}$ time dependence. (a) Complex effective permittivity $\epsilon_{eff} = \epsilon'_{eff} - j\epsilon''_{eff}$, (b) complex effective permeability $\mu_{eff} = \mu'_{eff} - j\mu''_{eff}$.

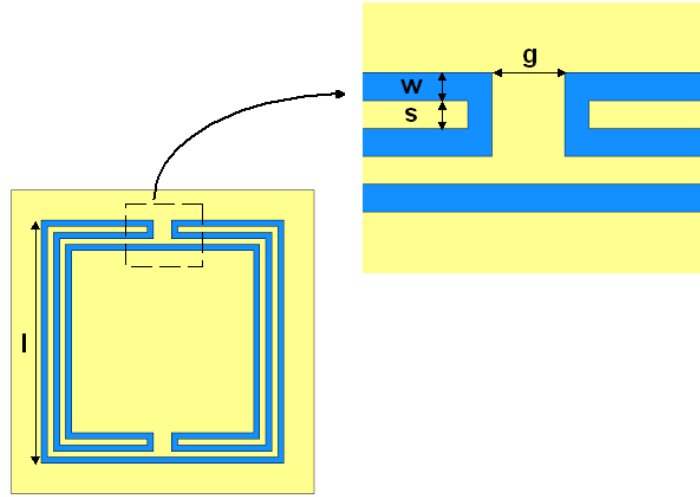


Figure 4.20: Schematic view of Single Loop Resonator unit cell

4.3.1 Design and Simulations

Geometry of the proposed SLR unit cell is described in Figure 4.20 together with its design parameters and the details of electromagnetic excitation. This square shaped SLR unit cell is designed with copper lines of thickness $t_{copper} = 0.03$ mm, side length $l = 4$ mm, gap width $g = 0.3$ mm, line width $w = 0.1$ mm and separation distance between two neighboring copper lines $s = 0.1$ mm. This SLR pattern is printed over a square shaped Rogers RO3003(tm) substrate, which has the dielectric constant $\epsilon_r = 3$, dielectric loss-tangent $\tan \delta_c = 0.0013$, side

length $L = 5$ mm and thickness $d = 0.5$ mm.

In simulations, the SLR unit cell is placed within a waveguide structure and excited by an electromagnetic wave with propagation vector (\vec{k}) along the x axis, electric field vector (\vec{E}) along the y axis and magnetic field vector (\vec{H}) along the z axis, as shown in Figure 4.21. Accordingly, the walls perpendicular to y axis are modeled to be PEC boundaries, the walls perpendicular to z axis are modeled to be PMC boundaries, and lastly the walls perpendicular to x axis are modeled to be the input/output ports [74].

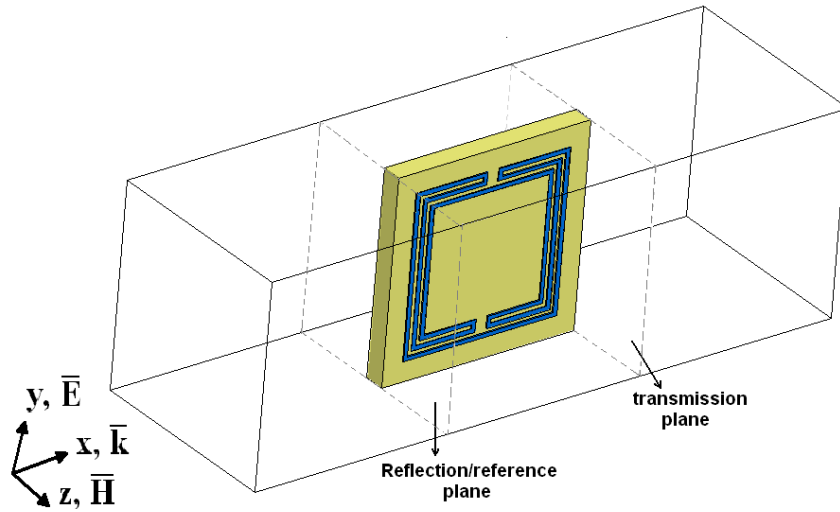
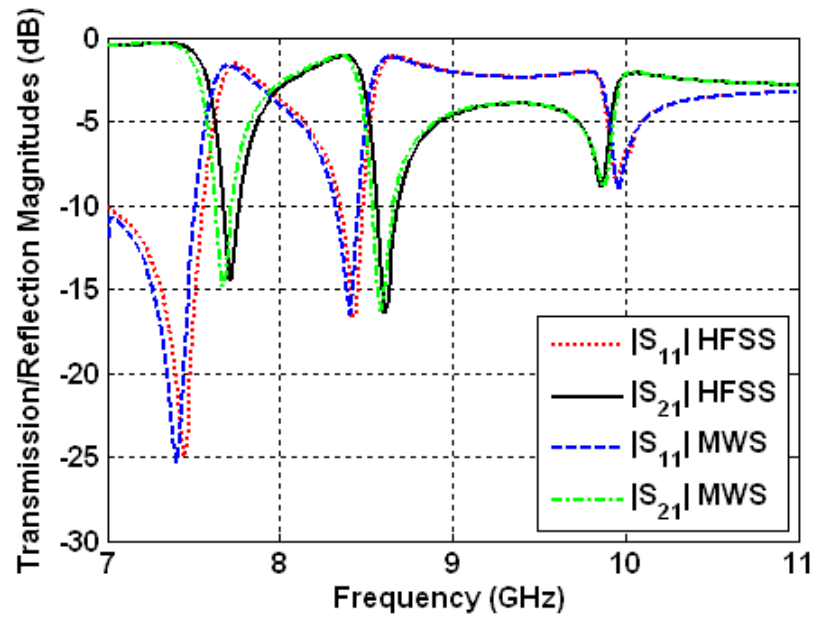


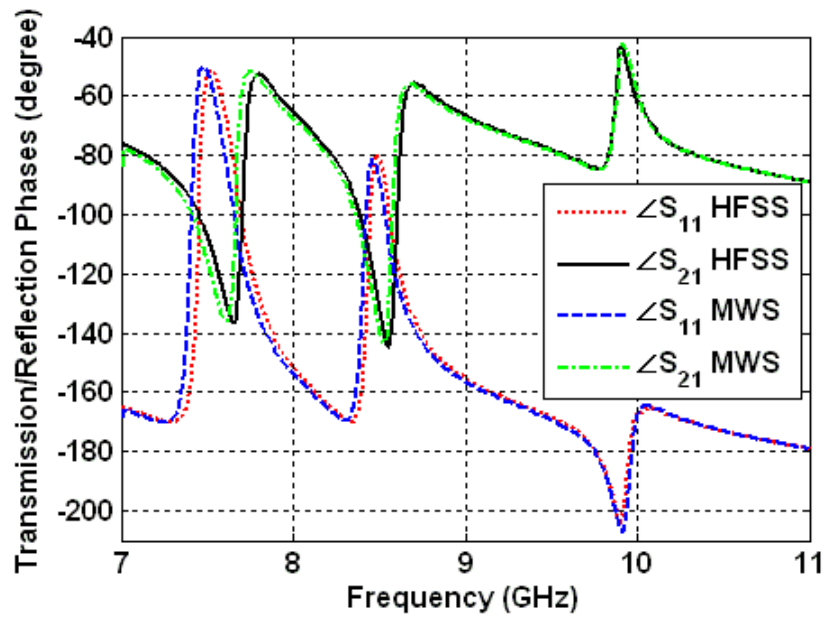
Figure 4.21: Simulation setup

4.3.2 Results

Magnitude and phase functions for the complex transmission (S_{21}) and complex reflection (S_{11}) parameters of the SLR array structure are computed by two different electromagnetic solvers, the HFSS and the MWS, with perfect agreement as shown in Figure 4.22(a) and Figure 4.22(b). It is seen in Figure 4.21 that the SLR structure resonates at three closely spaced frequencies, which are 7.72 GHz, 8.60 GHz, and 9.86 GHz. The third resonance at 9.86 GHz is observed to be the weakest of all. Moreover, Figure 4.23 shows the HFSS simulation results for the current distributions on the SLR unit cell structure at each resonance frequencies. This figure shows that current flows in the inner and outer rings of the SLR are in



(a) Magnitude spectra.



(b) Phase spectra.

Figure 4.22: Transmission and reflection characteristics of the SLR array.

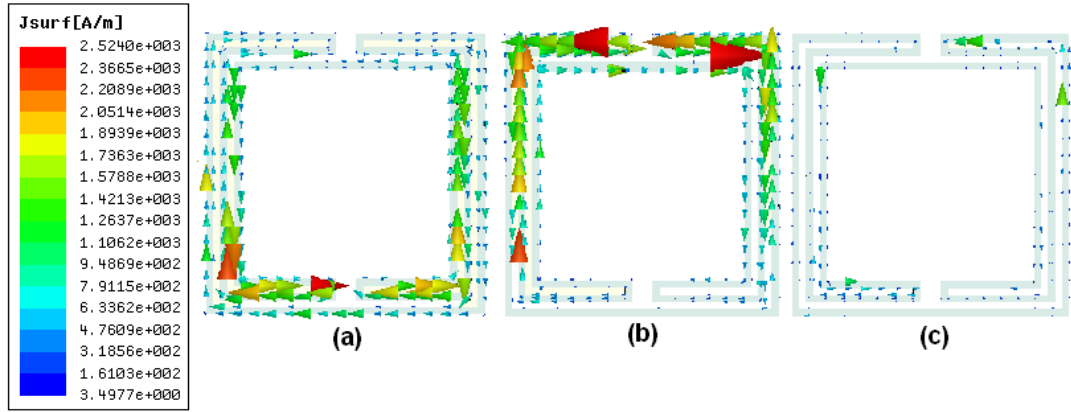
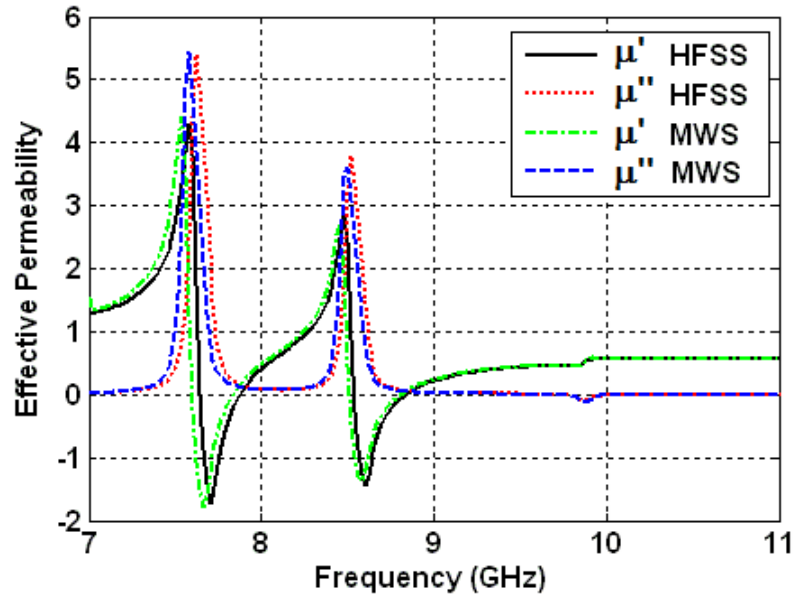


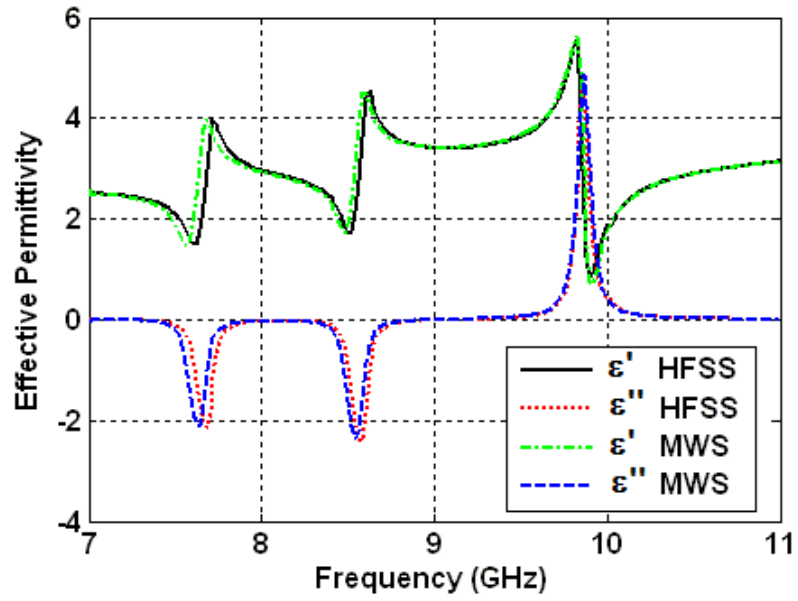
Figure 4.23: Current distribution on the SLR unit cell at each resonance frequency. (a) At 7.72 GHz, (b) at 8.60 GHz, (c) at 9.86 GHz.

opposite directions, unlike those in the SRR and SR structures, because of the special winding geometry of the SLR. The third resonance, which is shown to be the weakest one in Figure 4.22(a), has the weakest surface current distributions along its arms.

Next, the effective medium parameters, (μ_{eff}) and (ϵ_{eff}) , of the SLR structure are retrieved from the simulated complex S_{21} and S_{11} parameters by using the procedure given in [35] and plotted in Figure 4.24. Real part of the effective relative permeability is demonstrated to be negative over two separate frequency bands, from 7.64 to 7.88 GHz and from 8.53 to 8.84 GHz in Figure 4.24(a), corresponding to the first two magnetic resonances of the SLR. Real part of the effective relative permittivity never becomes negative as shown in Figure 4.24(b) although it gets closer to the zero level around the electrical resonance frequency of 9.86 GHz.



(a) Effective permeability



(b) Effective permittivity

Figure 4.24: Complex effective medium parameters of the SLR structure. $\mu_{eff} = \mu'_{eff} - j\mu''_{eff}$ and $\epsilon_{eff} = \epsilon'_{eff} - j\epsilon''_{eff}$ using $e^{j\omega t}$ time dependence.

CHAPTER 5

FREQUENCY-TUNABLE METAMATERIALS USING BROADSIDE COUPLED AND GAP TO GAP ORIENTED SPLIT RING RESONATORS: DESIGN, FABRICATION AND CHARACTERIZATION IN TERAHERTZ REGION

5.1 Introduction

There are various approaches reported in metamaterial literature for tuning purposes as mentioned in Section 1.1.4. However, the structural tunability approaches based on near-field interactions, which is the main interest of this part of the dissertation, have been reported very recently [24, 137, 138, 139]. In more detail, Wang et al. proposed a tunability method in microwave region for the magnetically excited BC-SRR structure having two layers placed perpendicular to the \vec{H} field direction [137]. In that study, the idea was to shift one layer relative to the other very slightly to change the resonance frequency mainly because of a small change in the total capacitance of the structure without disturbing the mutual inductance term. In [138] Powell et al. investigated the tunability in microwave region for both BC-SRR arrays and gap-to-gap oriented SRR arrays under again magnetic excitation. They demonstrated that BC-SRR arrays provided much more sensitivity in terms of tunability with respect to the gap-to-gap oriented SRR arrays. A similar study was also conducted in [139] for only BC-SRR arrays. In both [138] and [139], the frequency tunability was obtained by shifting one layer horizontally along the wave vector \vec{k} direction with respect to the other. In 2010, we extended this study to terahertz region for electrically excited BC-SRR structures [24].

In this part of dissertation, three kinds of two-layered SRR arrays in THz region are designed, fabricated, and characterized under electrical excitation with specific lateral shift amounts (i.e.

no-shift ($0 \mu\text{m}$), $5 \mu\text{m}$, $10 \mu\text{m}$, $15 \mu\text{m}$, $20 \mu\text{m}$, $30 \mu\text{m}$) between their layers in the specific directions (i.e. vertical or horizontal). These three topologies are vertically and horizontally shifted versions of BC-SRRs and the vertically shifted version of the gap-to-gap oriented SRR arrays. The schematic views and for the BC-SRR and the gap-to-gap oriented SRR are given in Figure 5.1(a) and (b), respectively. In all three topologies, the layers are placed perpendicular to the propagation direction, vertical direction is parallel to the incident \vec{E} field and horizontal direction is parallel to the incident \vec{H} field. Each topology is composed of same-sized SRR unit cells with the periodicity of $58 \mu\text{m}$. For characterization, the transmission spectra (i.e. $|S_{21}|$) of the SRR topologies are computed by using CST Microwave Studio (MWS), and these results are verified experimentally by using terahertz time-domain spectroscopy (THz-TDS). Among all our three designs, the best tunability results have been observed for our vertically shifted BC-SRR topology, which promises a maximum value of 663 GHz absolute shift (i.e. 51 % of the no-shift frequency) in experiments. Absolute shift of 720 GHz (i.e. 53 %) is computed in simulations for $30 \mu\text{m}$ vertical shift case. This result is very significant because it is the best ever tunability result reported in literature. Besides, horizontally shifted BC-SRR and vertically shifted gap-to-gap oriented SRR designs produce 270 GHz (i.e. 20 %) and 138 GHz (i.e. 15 %) maximum frequency shifts in experiments, respectively, which are also quite satisfactory values for many applications. The contributions of this part of the dissertation to the metamaterial literature can be summarized as follows:

- The coupled two-layer SRR structures reported in this study are designed and fabricated in terahertz region. All, the previous designs for structural tuning [137, 138, 139] were reported as microwave region applications.
- The structures of this study are excited electrically, rather than magnetically. We want to emphasize here that it is an important point to demonstrate the structural tunability under electrical excitation for THz metamaterial applications, since they have attracted a great interest recently [24, 102, 115, 140, 141, 142, 143, 144, 145].
- It has been demonstrated both numerically and experimentally that vertical shifting mechanism provides broader operational bandwidths which may be useful in broadband metamaterial applications. It has also been shown that gap-to-gap oriented topology promises much broader bandwidths than BC-SRR topology in vertical shifting mechanism.

- The tunability of BC-SRR is investigated for both vertical and horizontal shifted cases. It is demonstrated that our newly proposed vertically shifted case provides much higher tunability (maximum 51 % tunability for vertically shifted case and maximum 20 % tunability for horizontally shifted case).

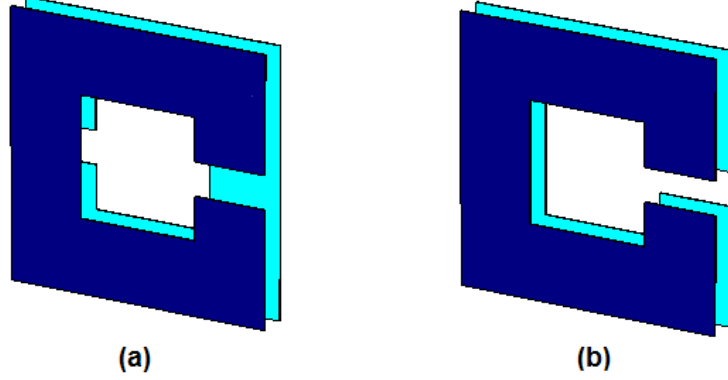


Figure 5.1: Schematic views of (a) BC-SRR and (b) gap-to-gap oriented structures.

5.2 Design, Fabrication, and Characterization

5.2.1 Design

In this study, all our designed structures are composed of square shaped SRR unit cells having the same physical dimensions. The schematic views, the related parameters, and the excitations are given in Figure 5.2. Herein, while Figure 5.2(a) is giving us the top view, Figure 5.2(b) gives the perspective view for the BC-SRR structure with no-shift. The square shaped unit cell has the periodicity $P = 58 \mu\text{m}$, metalization side-length $l = 40 \mu\text{m}$, metalization width $w = 11 \mu\text{m}$, gap width $g = 5 \mu\text{m}$, metal thickness $t_{metal} = 0.2 \mu\text{m}$, substrate thickness (i.e. distance between neighboring rings along z direction) $t_{sub} = 5 \mu\text{m}$, and superstrate thickness $t_{super} = 5 \mu\text{m}$. Herein, the substrate and the superstrates are made of thin-films of polyimide (PI-5878G, HD Microsystems TM) with the relative permittivity $\epsilon_r = 2.88$ and the dielectric loss-tangent $\tan \delta_c = 0.0313$. The metalization are made of golden strip lines with the electric conductivity $\sigma_{gold} = 40.9 \times 10^6 \text{ S/m}$.

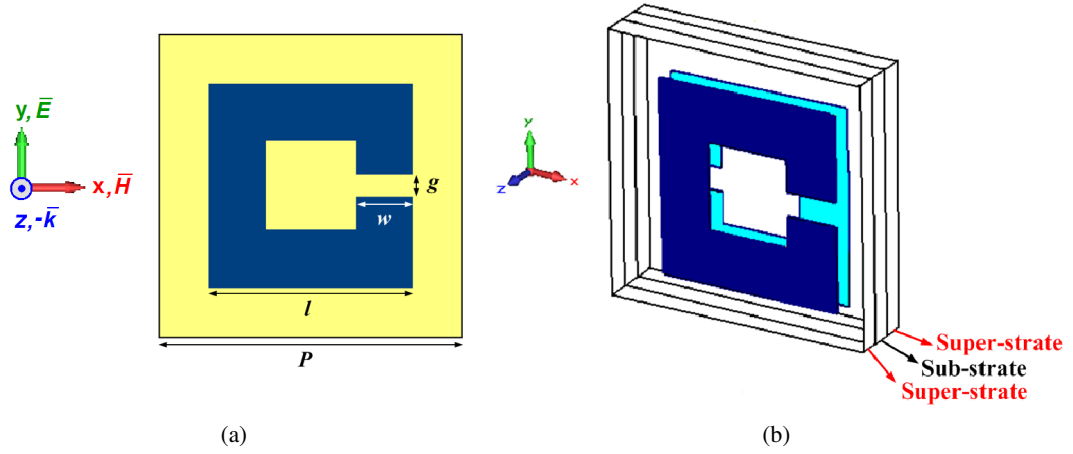


Figure 5.2: Schematic view, dimensions, and excitation for a single SRR, which forms BC-SRR or gap-to-gap oriented structure. $P = 58 \mu\text{m}$, $l = 40 \mu\text{m}$, $w = 11 \mu\text{m}$, $g = 5 \mu\text{m}$, substrate thickness (t_{sub}) = $5 \mu\text{m}$, and superstrate thickness (t_{super}) = $5 \mu\text{m}$. (a) Top view. (b) Transparent perspective view for the BC-SRR case with no-shift.

5.2.2 Fabrication

The structures are fabricated by conventional photolithographic methods. For all structures, $5 \mu\text{m}$ of polyimide is spin-coated as our first superstrate and then 200-nm thick gold with a 10 nm thick adhesion layer of titanium is deposited on a resist layer (S1813, Shipley) and patterned to form a planar array of SRR structures on $5\text{-}\mu\text{m}$ thick polyimide superstrate structure. After that, another $5\text{-}\mu\text{m}$ thick polyimide layer is coated on the SRR array as the substrate. Then second planar array of SRR layer is patterned to form a BC-SRR or gap-to-gap oriented SRR structure. Finally, a $5\text{-}\mu\text{m}$ thick polyimide is coated on metamaterials as the second superstrate (see Figure 5.2(b)). The optical microscope photographs of the fabricated structures are given in Figures 5.6, 5.12, and 5.17. These are vertically shifted BC-SRR array, horizontally shifted BC-SRR array, and vertically shifted gap-to-gap oriented SRR array, respectively.

5.2.3 Characterization

In this study, the designed and fabricated structures are characterized (i.e., the $|S_{21}|$ versus frequency data are obtained) both numerically and experimentally. For this purpose, numerical computations are performed by using the frequency domain solver of CST MWS under unit cell boundary conditions (UC-BCs). Herein, the UC-BCs are applied along the planes

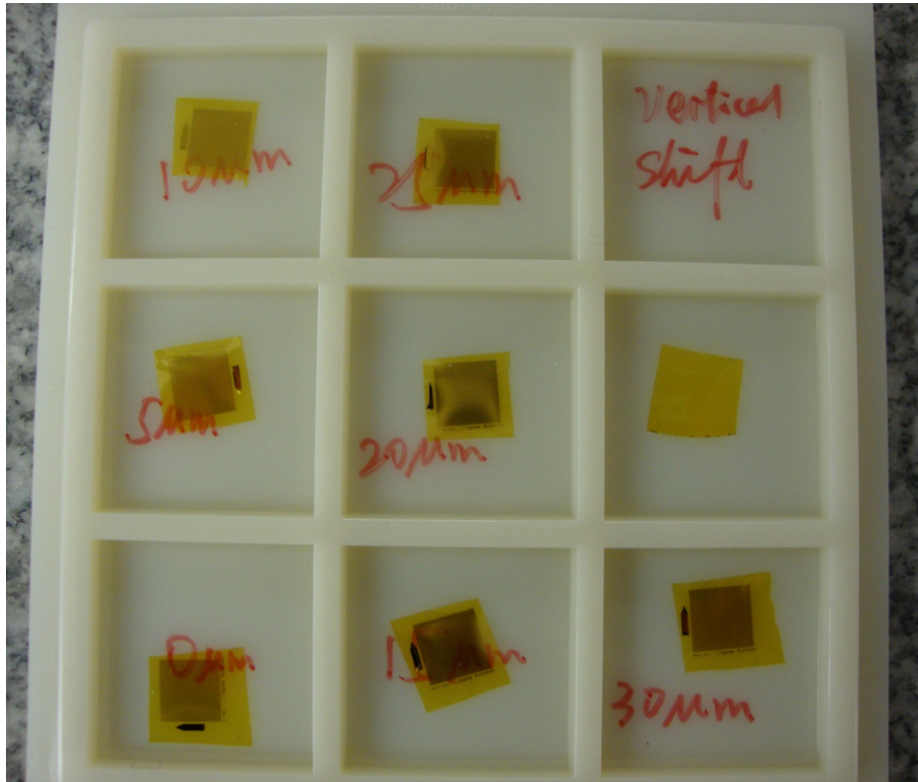


Figure 5.3: A photograph of the fabricated metamaterial arrays.

perpendicular to x and y axes to provide periodicity along the corresponding axis directions. On the other hand, terahertz time-domain spectroscopy (THz-TDS) is used for the experimental characterization. The THz-TDS setup is shown in Figure 5.4. In both simulations and experiments, each structure is excited by a TEM wave with propagation vector (\vec{k}) along the negative z axis, electric field intensity vector (\vec{E}) along the y axis, and magnetic field intensity vector (\vec{H}) along the x axis as shown in Figure 5.2. The simulation outputs are used for the extraction of effective medium parameters. The details of this procedure are given in Section 5.3.

5.3 Effective Medium Parameters

In this part, the method for the extraction of the effective medium parameters together with an approach for the verification of the extraction results will be discussed. Herein, effective medium parameters are simply ϵ and μ . The outputs of the parameter retrieval process will be

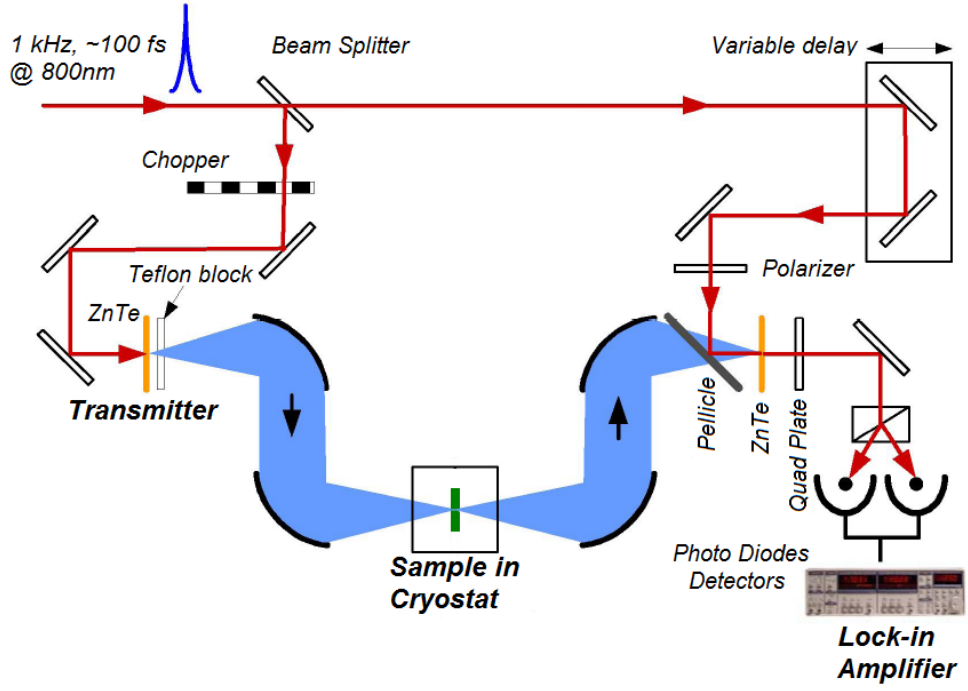


Figure 5.4: THz-TDS setup for metamaterial experimental characterization.

shown in Section 5.4.

5.3.1 Extraction of Effective Medium Parameters

For the extraction of the effective medium parameters, the method described in [36] is implemented in MATLAB. This method is based on the calculation of effective medium refractive index (n_{eff}) and intrinsic impedance (z_{eff}) using computed/measured complex scattering parameters S_{21} and S_{11} . The extractions of n_{eff} and z_{eff} from S_{21} and S_{11} are done by using the Equations (5.1) and (5.2), respectively.

$$n_{eff} = \frac{1}{kd} \arccos \left[\frac{1}{2S_{21}} (1 - S_{11}^2 + S_{21}^2) \right] \quad (5.1)$$

$$z_{eff} = \sqrt{\frac{(1 + S_{11})^2 - S_{21}^2}{(1 - S_{11})^2 - S_{21}^2}} \quad (5.2)$$

To be able to extract ϵ_{eff} and μ_{eff} , Equations (5.3) and (5.4) are used, respectively.

$$\epsilon_{eff} = \frac{n_{eff}}{z_{eff}} \quad (5.3)$$

$$\mu_{eff} = n_{eff} z_{eff} \quad (5.4)$$

5.3.2 An Approach For the Verification of Effective Medium Parameters

In this study, the results for μ_{eff} and ϵ_{eff} are verified with the procedure described as follows:

Step 1: First, complex S_{11} and S_{21} values are obtained by using a full wave electromagnetic simulation software.

Step 2: Using these complex S_{11} and S_{21} values, the effective medium parameters are extracted, as usual. Up to this point, the procedure is the same as described in Section 5.3.1.

Step 3: Then, extracted μ_{eff} and ϵ_{eff} values are used to define a new homogeneous medium having $\mu = \mu_0 \mu_{eff}$ and $\epsilon = \epsilon_0 \epsilon_{eff}$. To do that:

- The extracted relative permittivity values are fitted to the Lorentz model which is given in equation 5.5. Herein, Lorentz model formulation for permittivity is used since the structures in this study are excited electrically. After the fitting procedure, the Lorentz model parameters; epsilon infinity value ϵ_{∞} , epsilon static value ϵ_{static} , resonance frequency ω_0 , and damping factor Γ are obtained. Herein, the real μ_{eff} value ($\text{Im}\{\mu_{eff}\} = 0$) is used and it is set to unity. Hence magnetic resonant behavior is not expected since the structures are excited electrically and all structures in the design are inherently non-magnetic.
- Lastly, those Lorentz model parameters (i.e. ϵ_{∞} , ϵ_{static} , ω_0 , Γ) are used as the inputs of transmission/reflection (T/R) plotter program. This program has been implemented in MATLAB by A. Strikwerda at Boston University based on the formulation in reference [146]. As the outputs of T/R plotter, S_{11} and S_{21} graphs are obtained. It is significant that T/R plotter is not a must to obtain transmission and reflection characteristics. CST MWS has the capability of defining a dispersive medium based on the Lorentz model. Thus, S_{11} and S_{21} characteristics of this Lorentz type dispersive medium can be easily

obtained by using CST MWS. However, it will take much more time than that of T/R plotter.

$$\epsilon(\omega) = \epsilon_{\infty} + \frac{(\epsilon_{static} - \epsilon_{\infty})\omega_0^2}{(\omega_0^2 - \omega^2) + j\omega\Gamma} \quad (5.5)$$

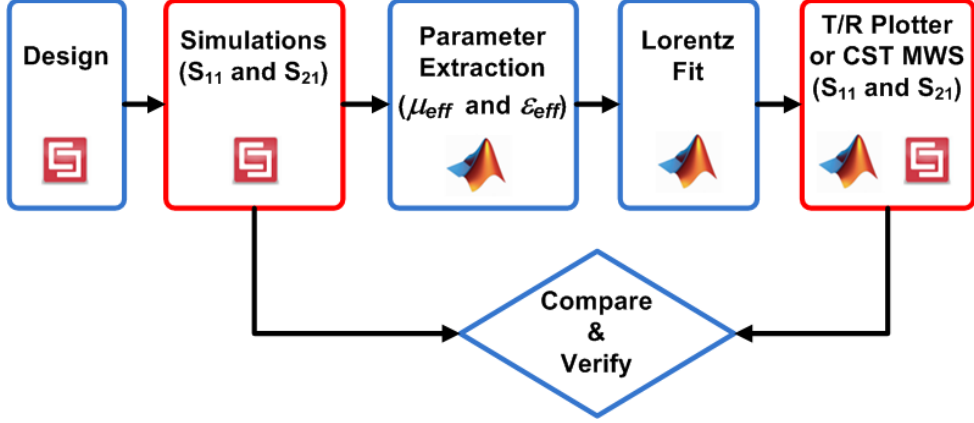


Figure 5.5: Flow chart for the verification of effective medium parameters.

5.4 Results

The optical microscope pictures of the vertically shifted BC-SRR designs for different shift amounts and their corresponding $|S_{21}|$ plots are given in Figures 5.6 and 5.7, respectively. Herein, while Figure 5.7(a) is showing the simulation results, Figure 5.7(b) demonstrates the experimental ones. As we increase the shift amount from zero to $30 \mu\text{m}$, the resonance frequency of the array structure decreases dramatically from 1.351 THz to 0.631 THz in simulations and from 1.304 THz to 0.641 THz in experiments. These shift amounts correspond to a 720 GHz absolute and 53 % percentage shift in simulation results and 663 GHz absolute and 51 % percentage shift in experimental results. This is the highest shift amount in literature for SRR based metamaterial structures up-to-date.

For a further investigation, the extracted effective medium parameters ϵ_{eff} and μ_{eff} for vertically shifted BC-SRR structures are presented for different shift amounts in Figure 5.8. These

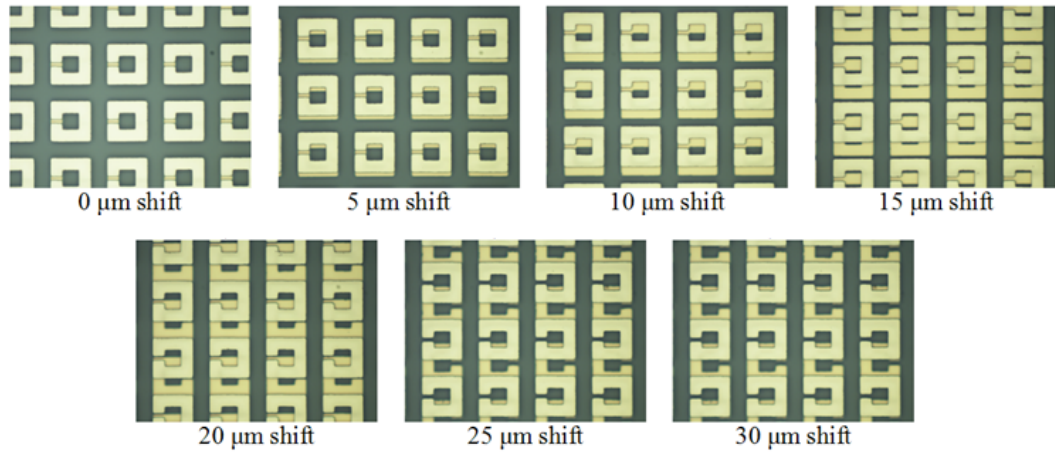


Figure 5.6: Optical microscope pictures of BC-SRR structures shifted along vertical direction for 0 μm (no-shift), 5 μm , 10 μm , 15 μm , 20 μm , 25 μm , and 30 μm .

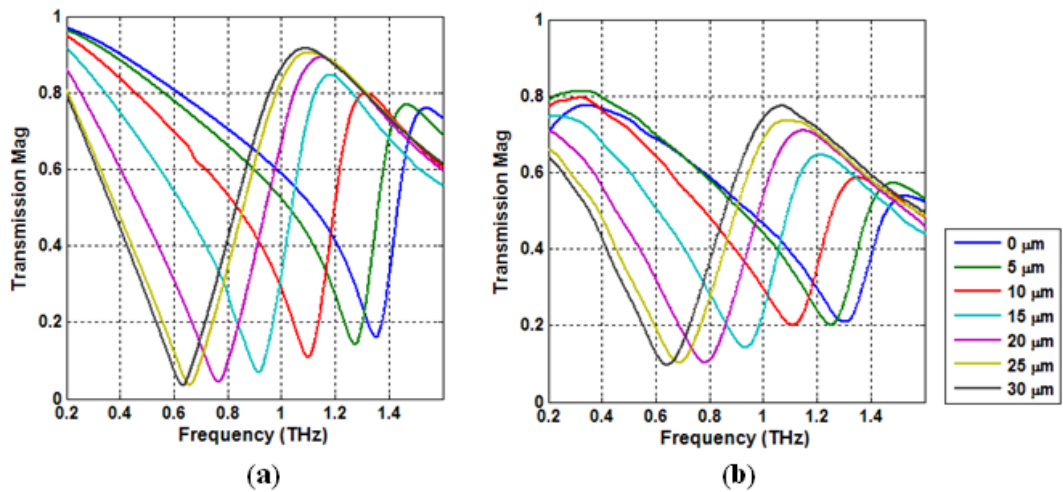
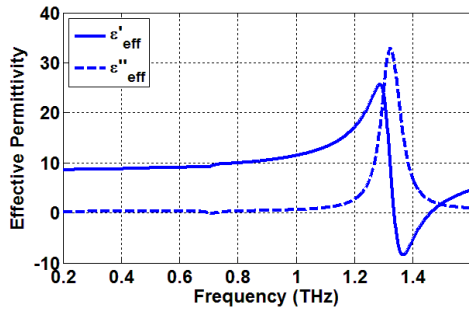


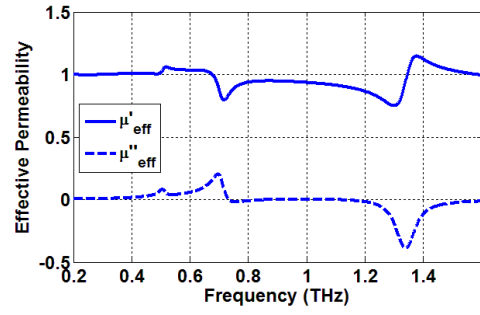
Figure 5.7: Transmission magnitudes vs frequency of BC-SRR structures shifted along vertical direction for 0 μm , 5 μm , 10 μm , 15 μm , 20 μm , 25 μm , and 30 μm . (a) Simulation and (b) experimental results.

graphs show that all vertically shifted versions of the BC-SRR show Lorentz type dielectric dispersion behaviors around their resonance frequencies and also relatively narrow epsilon negative (ENG) regions. On the other hand, the real parts of μ_{eff} plots take values around unity and imaginary parts take values around zero. However, an unexpected fluctuation is observed in μ_{eff} graphs of each shifted version just around the resonance frequency. In other words, a magnetic response around the purely electrical resonance is not expected. These artifacts are explained by spatial dispersion phenomena and these fluctuations are called anti-resonant behaviors [37, 147, 148]. In more detail; the extraction procedure is done under the assumption of a homogeneous medium. However, although the SRR based unit cells are electrically small compared to the free space wavelength, we are still far from constructing an *ideal* homogeneous medium. So, being an effective medium, but not being an ideal one causes these anti-resonant effects. Thus, electrically smaller structures are much preferable ones to achieve much better homogenization [13, 15, 16, 18, 20, 23, 37, 76, 147, 148]. Smaller the electrical size, the better homogenization will be. Recently, Liu et al. proposed a method for parameter extraction to include the effects of the spatial dispersion [37]. In this method, the effects of spatial dispersion are also taken into account. Using this procedure, effective medium parameters can also be extracted. As the examples, the results for the BC-SRR structure shifted along vertical direction for 20 μm and 30 μm are shown in Figure 5.9. In the permeability graphs, the anti-resonant effects clearly disappeared.

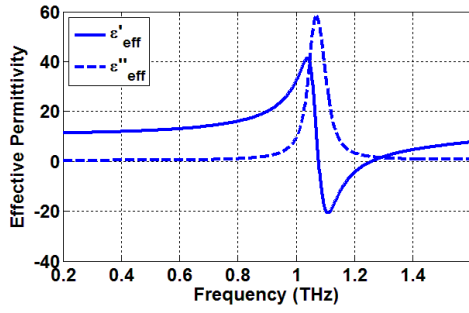
To verify the results given in Figure 5.8, the procedure described in Section 5.3.2 and Figure 5.5 is followed. As the part of this verification, each ϵ_{eff} graph shown in Figure 5.8 is fitted to the Lorentz model given in Equation (5.5) and corresponding Lorentz parameters are extracted in order to obtain transmission characteristics. The fitted curves together with the extracted effective medium parameters are plotted on the same graph for better comparison and given in Figure 5.10. It is clear that extracted and fitted curves show a very good agreement. As the decision stage of the verification, transmission characteristics are plotted for different shift amounts (i.e. 0 μm , 10 μm , 20 μm , and 30 μm) using their corresponding Lorentz model parameters as the input for T/R plotter (or CST MWS) and the outputs are presented in Figure 5.11(b). Figure 5.11(a) reports the simulation results previously given in Figure 5.7 for an easier comparison. Thus, Figure 5.11 verifies that the extracted effective medium parameters are consistent.



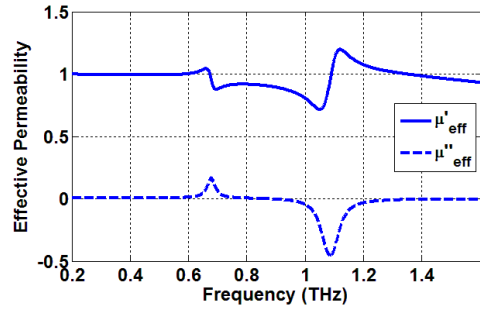
(a) 0 μm shift (no-shift)



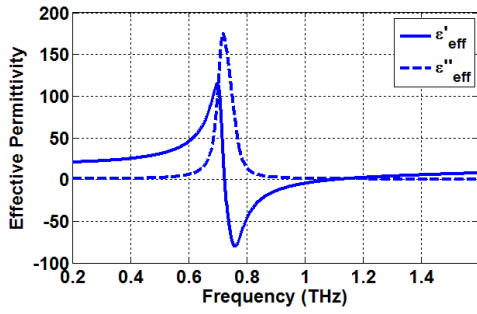
(b) 0 μm shift (no-shift)



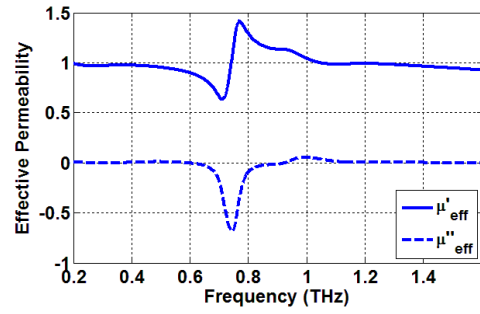
(c) 10 μm shift



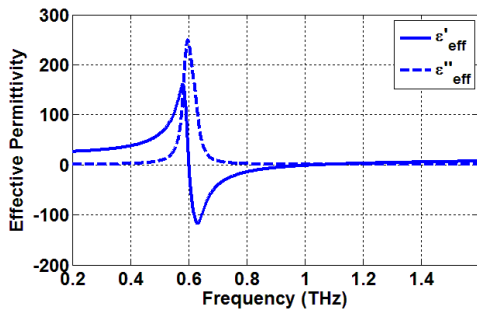
(d) 10 μm shift



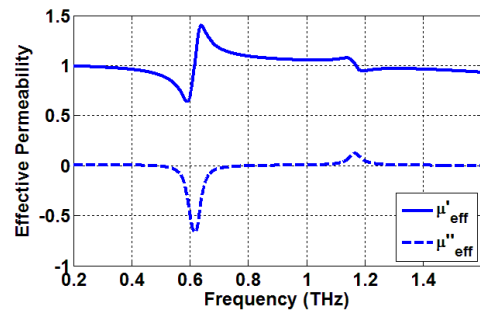
(e) 20 μm shift



(f) 20 μm shift



(g) 30 μm shift



(h) 30 μm shift

Figure 5.8: Effective permittivity ϵ_{eff} and effective permeability μ_{eff} graphs of BC-SRR structure shifted along vertical direction for 0 μm , 10 μm , 20 μm , and 30 μm .

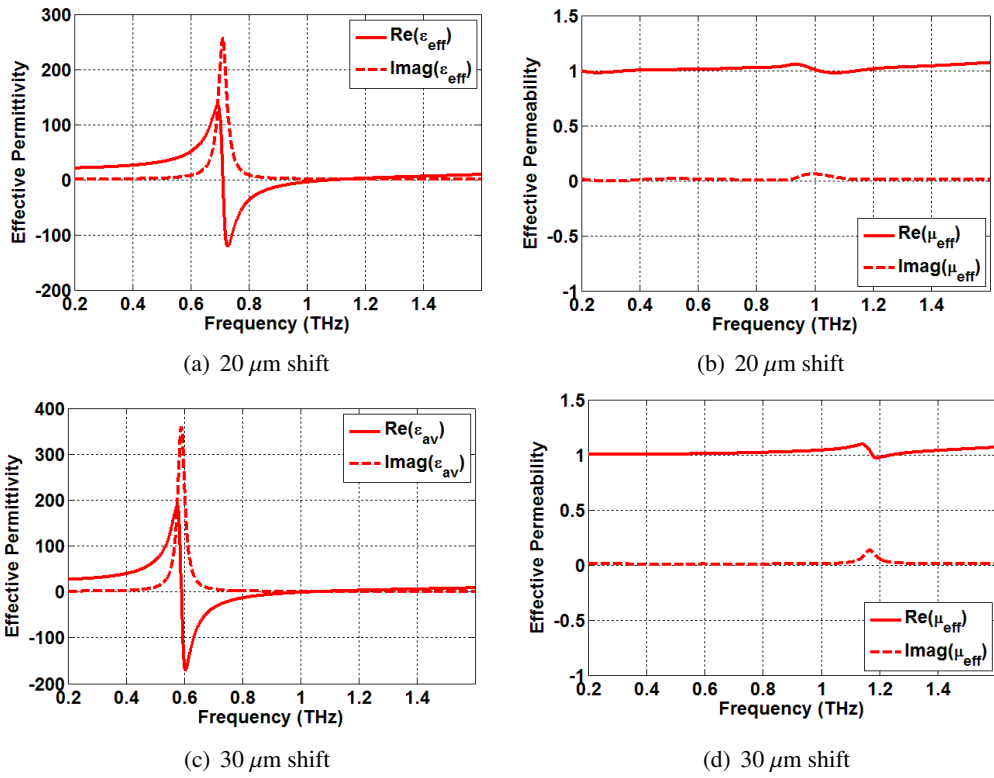


Figure 5.9: Effective average permittivity ϵ_{av} and effective average permeability μ_{eff} graphs of BC-SRR structure shifted along vertical direction for 20 μm and 30 μm as the demonstrations of the anti-resonant effects removal.

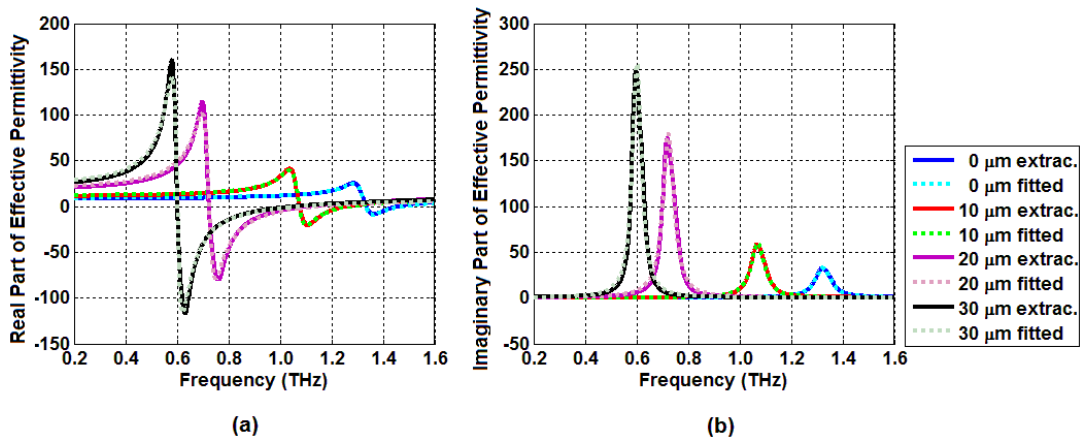


Figure 5.10: Extracted and fitted effective permittivity values of vertically shifted BC-SRR structure for μm , 10 μm , 20 μm , and 30 μm shifts. (a) Real and (b) imaginary parts.

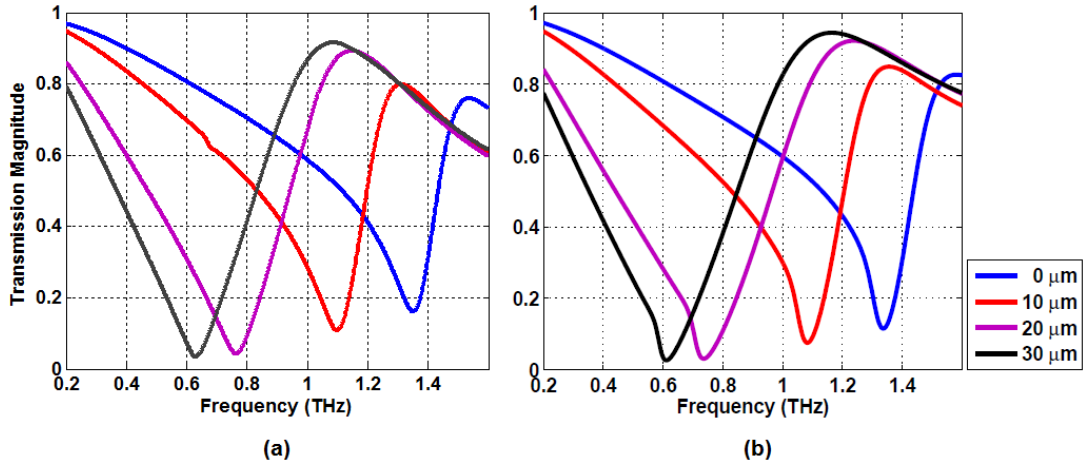


Figure 5.11: Verification of effective medium parameters for vertically shifted BC-SRR structure. (a) Experimental transmission characteristics. (b) Transmission characteristics obtained through fitted effective medium parameters.

Figures 5.12 and 5.13 show the optical microscope pictures of horizontally shifted BC-SRR designs and their corresponding characterization results, respectively. Herein, Figure 5.13(a) shows the simulation results and Figure 5.13(b) shows the experimental ones. As we increase the shift amount from $5 \mu\text{m}$ to $30 \mu\text{m}$, the resonance frequency of the structure decreases dramatically from 1.376 THz to 1.100 THz in simulations and from 1.328 THz to 1.058 THz in experiments. These shift amounts correspond to a 276 GHz absolute and 20% percentage shift in simulations and 270 GHz absolute and 20% percentage shifts in experiments. Different than the vertically shifted BC-SRR case, there is a slight increase in the frequency (i.e. from 1.358 THz to 1.376 THz in simulations and from 1.304 THz to 1.328 THz in experiments) as we increase the amount of shift from $0 \mu\text{m}$ to $5 \mu\text{m}$. This small blue-shift (i.e. increase in frequency) is supposed to be mainly the effect of small capacitive interactions between overlapping SRR structures and it will be discussed in more detail in Section 5.5.

For horizontally shifted BC-SRR structure, the extracted effective medium parameters are given in Figure 5.14. These graphs show Lorentz type dielectric dispersion behavior around their resonance frequencies and also relatively narrow epsilon negative (ENG) regions, just like vertically shifted cases. On the other hand, the real parts of μ_{eff} plots take values around unity and imaginary parts take values around zero. The anti-resonant effects in μ_{eff} graphs are also observed here.

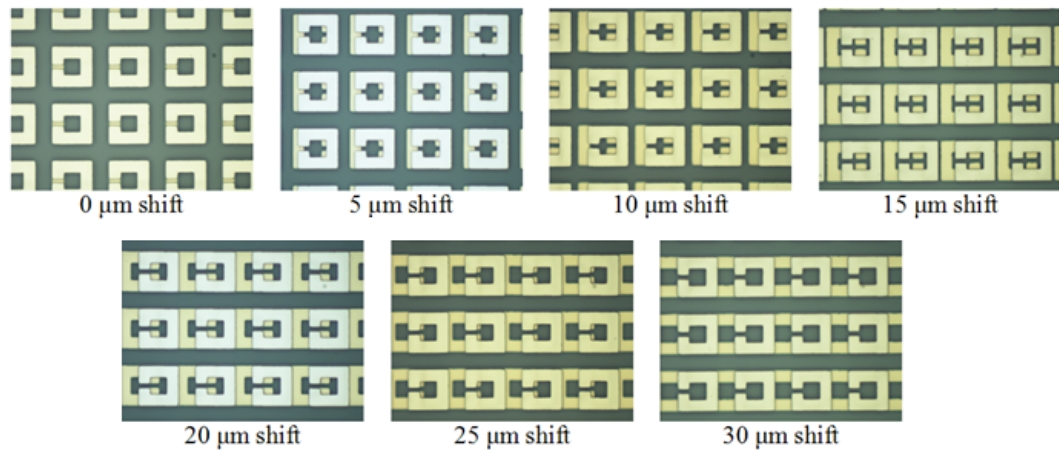


Figure 5.12: Optical microscope pictures of BC-SRR structures shifted along horizontal direction for 0 μm (no-shift), 5 μm , 10 μm , 15 μm , 20 μm , 25 μm , and 30 μm .

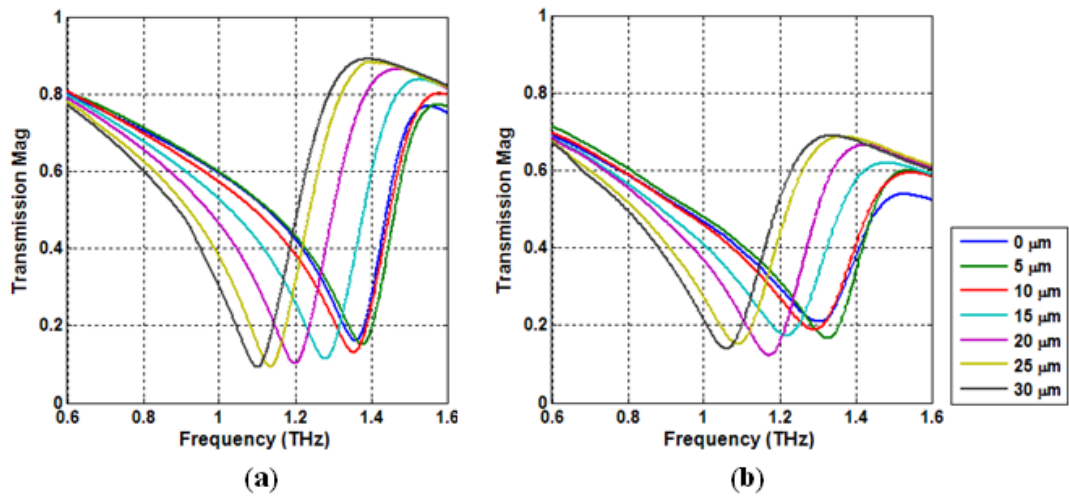


Figure 5.13: Transmission magnitudes vs frequency of BC-SRR structures shifted along horizontal direction for 0 μm , 5 μm , 10 μm , 15 μm , 20 μm , 25 μm , and 30 μm . (a) Simulation and (b) experimental results.

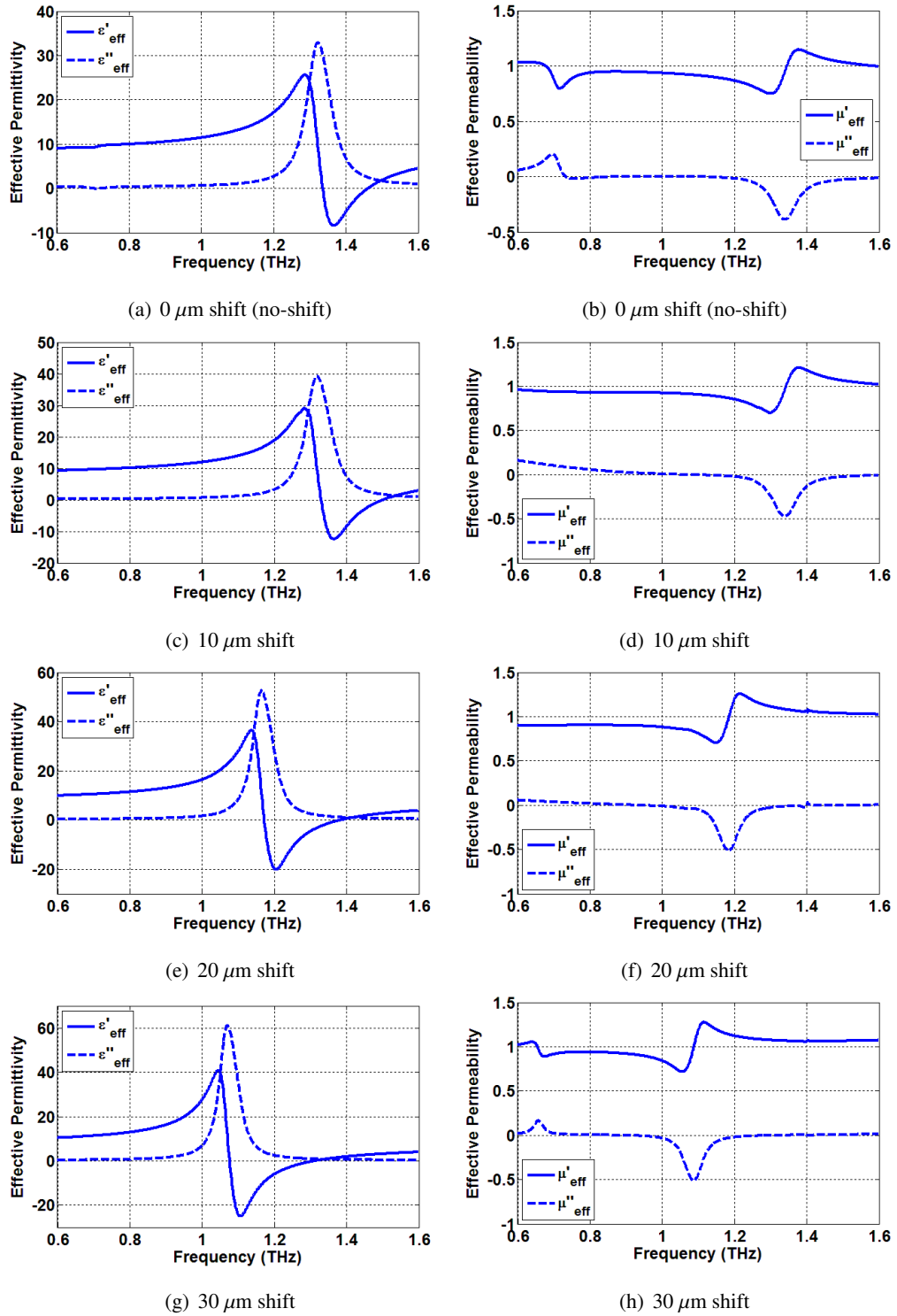


Figure 5.14: Effective permittivity ϵ_{eff} and effective permeability μ_{eff} graphs of BC-SRR structure shifted along horizontal direction for $0 \mu\text{m}$, $10 \mu\text{m}$, $20 \mu\text{m}$, and $30 \mu\text{m}$.

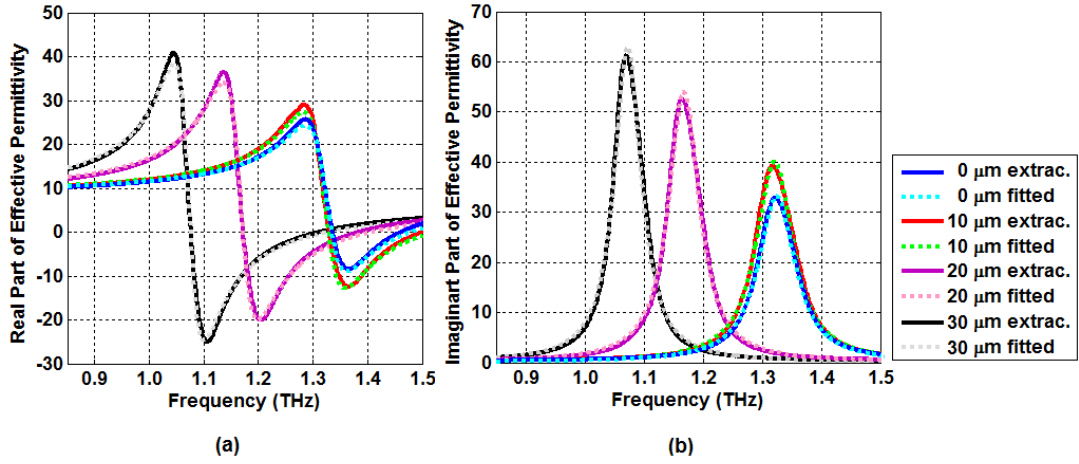


Figure 5.15: Extracted and fitted effective permittivity values of vertically shifted BC-SRR structure for μm , $10 \mu\text{m}$, $20 \mu\text{m}$, and $30 \mu\text{m}$ shifts. (a) Real and (b) imaginary parts.

For the verification of those results given in Figure 5.14, each graph is fitted again to the Lorentz model and fitting results are shown in Figure 5.15. The figures present that extracted and fitted curves show a very good agreement.

As the last stage of the verification for horizontally shifted BC-SRR, transmission characteristics are obtained for $0 \mu\text{m}$, $10 \mu\text{m}$, $20 \mu\text{m}$, and $30 \mu\text{m}$ using their corresponding Lorentz model parameters as the input for T/R plotter (or CST MWS) and the outputs are presented in Figure 5.16(b). Figure 5.16(a) shows the simulation results for an easier comparison. As a result, Figure 5.16 verifies the extracted effective medium parameters.

Figures 5.17 and 5.18 show the optical microscope pictures of gap-to-gap oriented SRR arrays shifted along vertical direction and their corresponding characterization results, respectively. Herein, while Figure 5.17(a) is presenting the simulation results, Figure 5.17(b) shows the experimental ones. As we increase the shift amount from $0 \mu\text{m}$ to $30 \mu\text{m}$, the resonance frequency of the structure decreases from 0.899 THz to 0.761 THz , which corresponds to a 138 GHz absolute and 15% percentage shift.

For the verification of those results given in Figure 5.19, each graph is fitted again to the Lorentz model and fitting results are given in Figure 5.20. The figures present that extracted

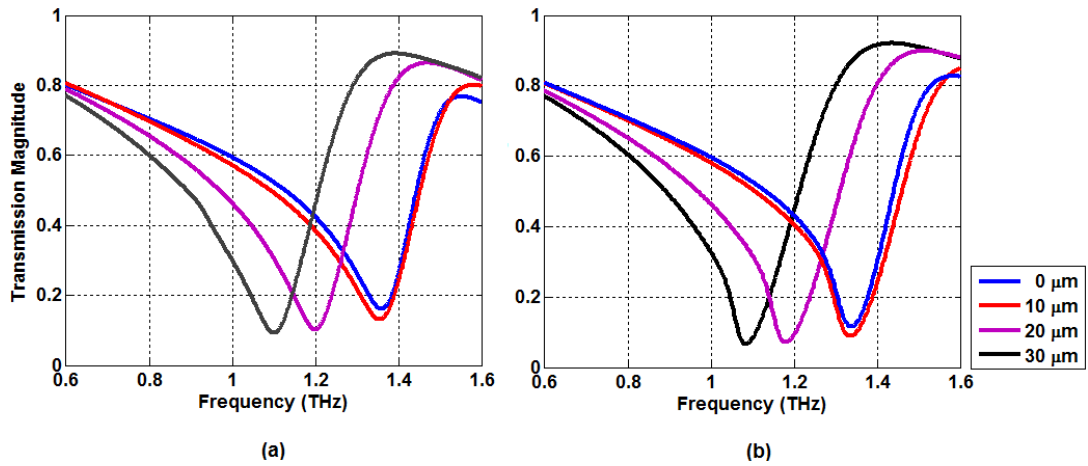


Figure 5.16: Verification of effective medium parameters for horizontally shifted BC-SRR structure. (a) Experimental transmission characteristics. (b) Transmission characteristics obtained through fitted effective medium parameters.

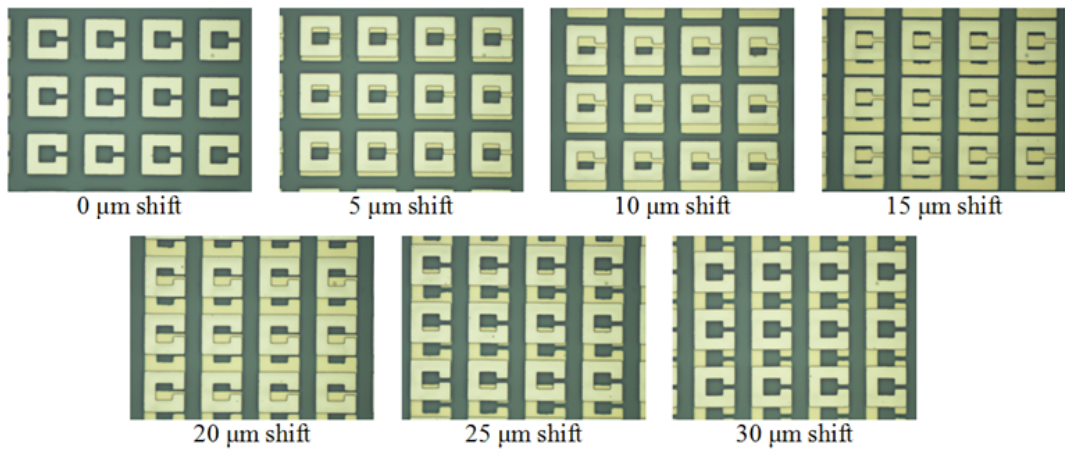


Figure 5.17: Optical microscope pictures of some specific gap-to-gap oriented structures shifted along vertical direction for 0 μm (no-shift), 5 μm , 10 μm , 15 μm , 20 μm , 25 μm , and 30 μm .

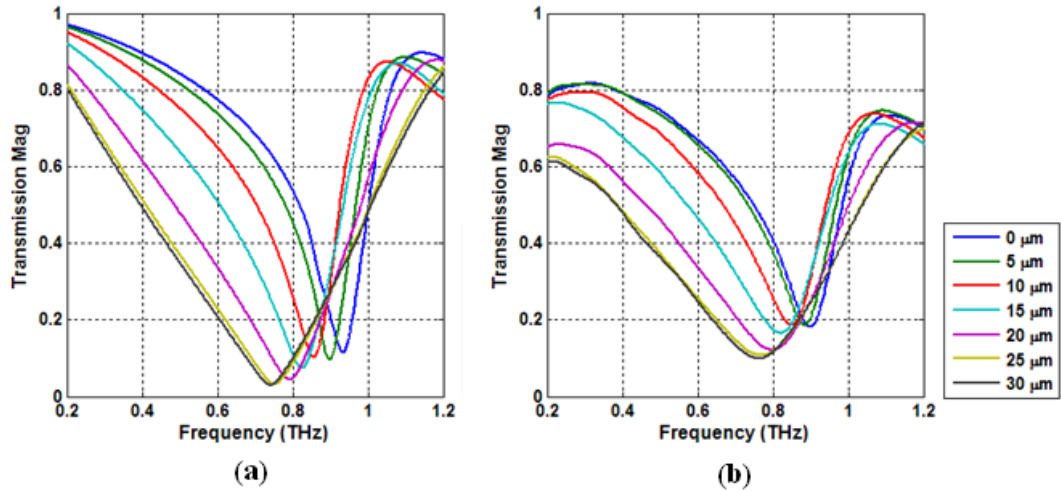


Figure 5.18: Transmission magnitudes vs frequency for gap-to-gap oriented structures shifted along vertical direction for $0\ \mu\text{m}$, $5\ \mu\text{m}$, $10\ \mu\text{m}$, $15\ \mu\text{m}$, $20\ \mu\text{m}$, $25\ \mu\text{m}$, and $30\ \mu\text{m}$. (a) Simulation and (b) experimental results.

and fitted curves show a very good agreement.

As the last stage of the verification, transmission characteristics are obtained for $0\ \mu\text{m}$, $10\ \mu\text{m}$, $20\ \mu\text{m}$, and $30\ \mu\text{m}$ using their corresponding Lorentz model parameters as the input for T/R plotter (or CST MWS) and the outputs are presented in Figure 5.21(b). Figure 5.21(a) shows the simulation results for an easier comparison. As a result, Figure 5.21 verifies the extracted effective medium parameters.

5.5 Discussion

The schematic views of the surface charge distributions and their corresponding surface current flows for the BC-SRR and gap-to-gap oriented SRR structures under normal incidence with the electrical excitation are given in Figure 5.22. In these plots, the surface charge distributions and surface current flows are demonstrated to provide an insight about the mutual capacitive and inductive effects between two neighboring rings in two layers, respectively.

Let us start with discussing inductive coupling effects in BC-SRR structure, thus let us consider the current flows in Figure 5.22(a). It is clear in the figure that the surface currents flow

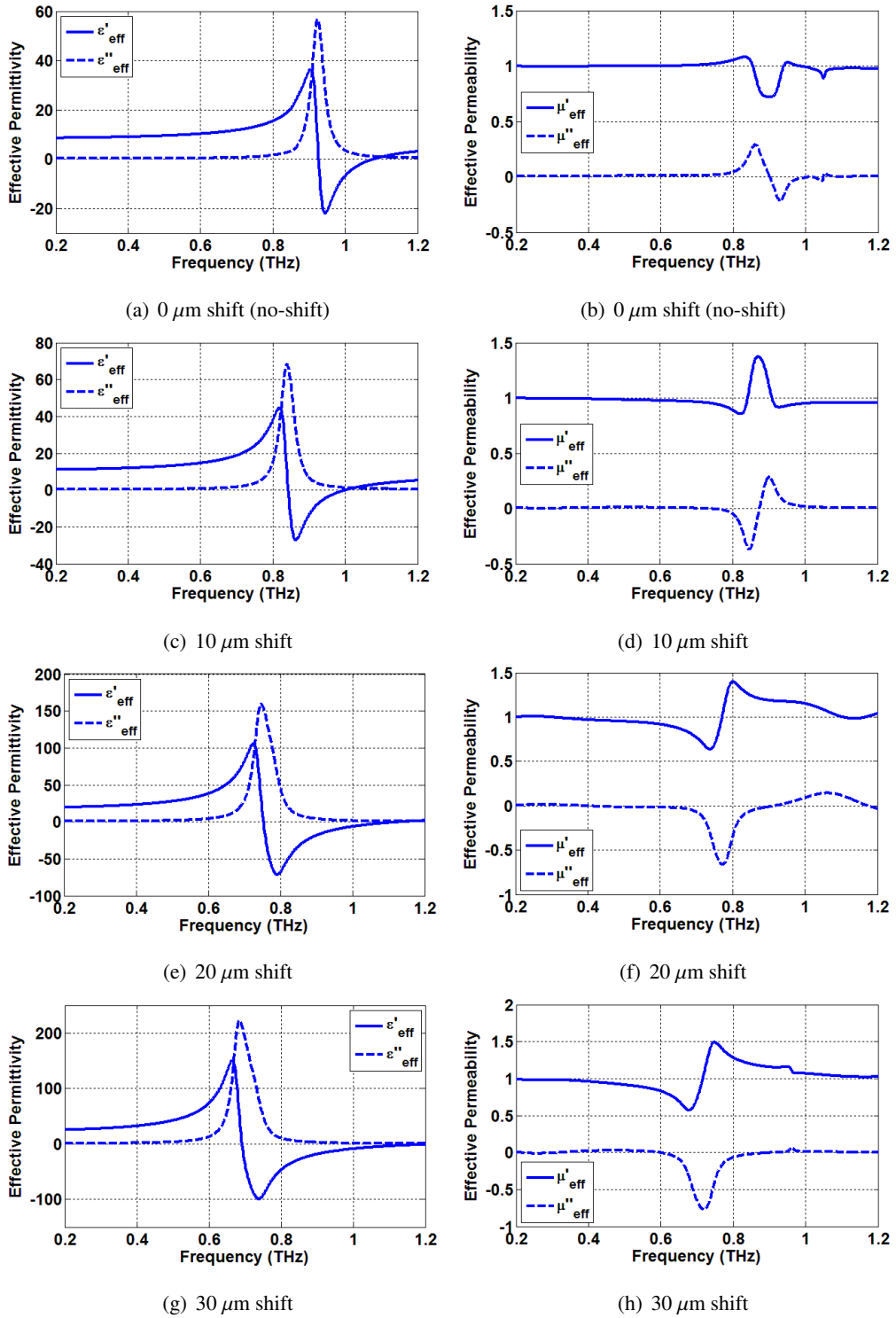


Figure 5.19: Effective permittivity ϵ_{eff} and effective permeability μ_{eff} graphs of gap-to-gap SRR structure shifted along vertical direction for $0 \mu\text{m}$, $10 \mu\text{m}$, $20 \mu\text{m}$, and $30 \mu\text{m}$.

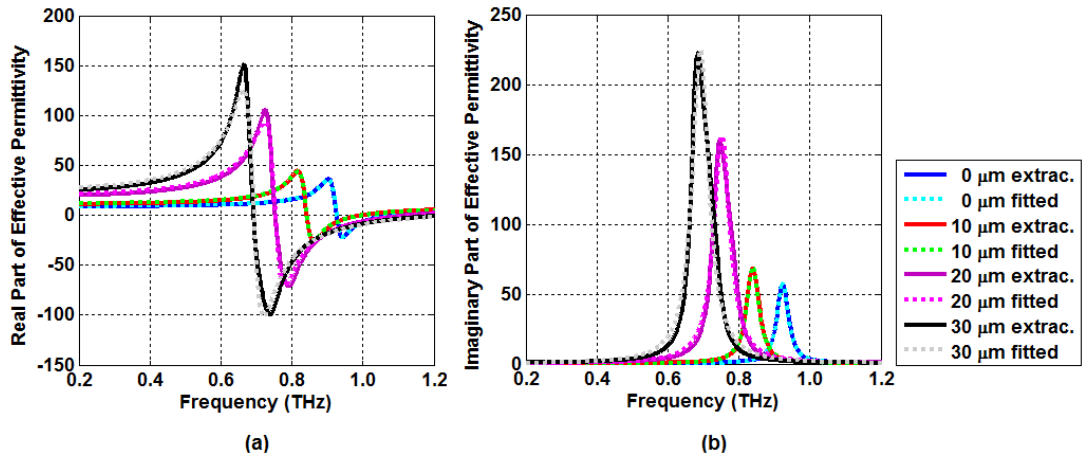


Figure 5.20: Extracted and fitted effective permittivity values of vertically shifted gap-to-gap oriented SRR structure for μm , 10 μm , 20 μm , and 30 μm shifts. (a) Real and (b) imaginary parts.

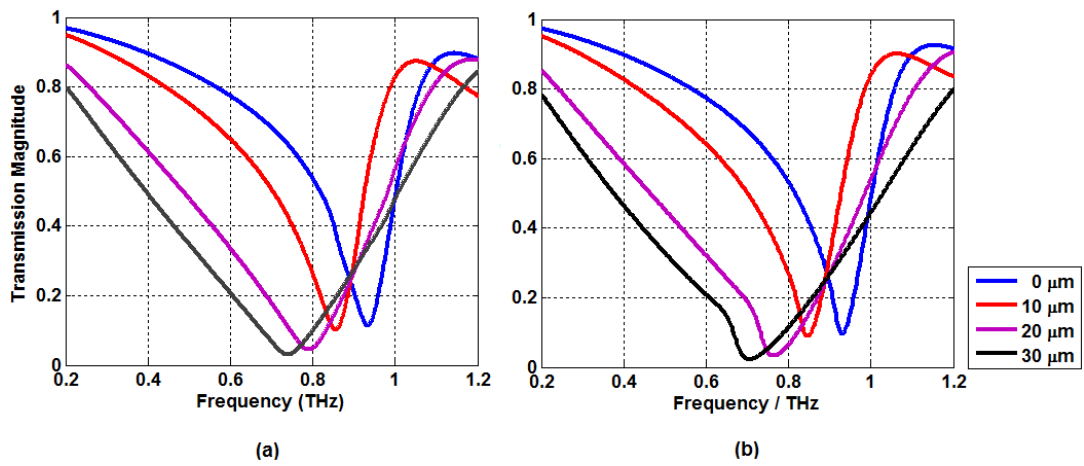


Figure 5.21: Verification of effective medium parameters for horizontally shifted BC-SRR structure. (a) Experimental transmission characteristics. (b) Transmission characteristics obtained through fitted effective medium parameters.

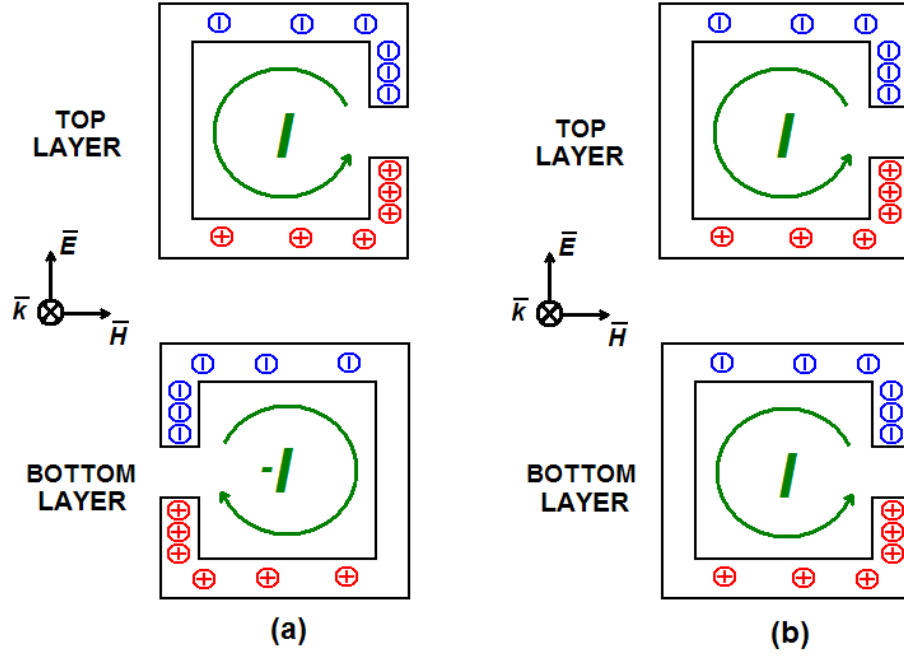


Figure 5.22: Schematic views of the surface charge distributions and their associated surface current distributions for (a) BC-SRR and (b) gap-to-gap oriented SRR structures.

in opposite direction with respect to each other between top and bottom layers. These opposite current flows result with a mutual inductance (L_{mutual}) with negative sign. For this case we can empirically define the total inductance as $L_{total} = L_{self} - L_{mutual}$. As we increase the shift amount from $0 \mu\text{m}$ to $30 \mu\text{m}$, the overlapping areas between neighboring rings and also the absolute values of L_{mutual} are going to decrease. For the electrically excited BC-SRR structure, the shift, whether it is in vertical or in horizontal direction (see Figures 5.6 and 5.12), will result with an increase in total inductance (L_{total}). Similarly, if we consider the inductive coupling effects in gap-to-gap oriented structure, we should have a look at the current flows in Figure 5.22(b). This time, the surface currents flow in the same direction in both layers. These current flows having the same direction will result with a mutual inductance (L_{mutual}) with positive sign. For this case we can empirically define the total inductance as $L_{total} = L_{self} + L_{mutual}$, which decreases with the increasing shift amount.

Now, let us discuss the capacitive coupling effects, thus let us consider the surface charge distribution on Figures 5.22(a) and 5.22(b) for BC-SRR and gap-to-gap oriented SRR structures, respectively. For the vertically shifted BC-SRR structure, the capacitive coupling becomes more important than that of the horizontally shifted version, because positive and negative

charged arms become much closer with the help of shift. In the case of horizontal shift, the neighboring rings in two layers always have the charge distribution with the same sign, thus the capacitive coupling is thought to be weaker. Although, both vertically and horizontally shifted BC-SRR structures have the same inductive coupling mechanism as it is described above, the stronger capacitive coupling in the vertically shifted version makes it much more sensitive to the amount of lateral shifts in terms of resonance frequency (see Figures 5.7 and 5.13). Moreover, we can estimate that, a similar capacitive coupling mechanism to the vertically shifted BC-SRR will be effective for the gap-to-gap oriented SRR structure with vertical shifts. For this case, as we increase the shift amount, positive and negative charged arms will get closer and the structure will introduce a relatively stronger capacitive coupling. Although, the gap-to-gap oriented SRR structure with vertical shifts has a decreasing inductive coupling as we increase the amount of shift, a dominant increasing capacitive effect helps us to explain the relatively small decrease in the resonance frequency.

It may be significant to note here that, there are also mutual capacitive and inductive coupling effects among the unit cells in the same layer, however they are not considered here as our tuning mechanism highly depends on the couplings among the elements in two different layers.

Lastly, we want to discuss the small blue-shift, which is observed in Figure 5.13 from $0 \mu\text{m}$ to $5 \mu\text{m}$ shifts. This unexpected small shift is observed to be mainly the effect of small capacitive interactions between overlapping SRR structures. This observation is validated by our supporting simulation results given in Figure 5.23(c) for the BC-SRR structures that are shifted horizontally in the opposite direction. The pictures of two cases for $5 \mu\text{m}$ shift amounts in opposite directions are given in Figure 5.23(a) and Figure 5.23(b), respectively for a better visualization. Herein, Figure 5.23(a) is the optical microscope picture of the fabricated structure, whereas Figure 5.23(b) is the schematic view. The simulation results in Figure 5.23(c) show that as we increase the shift from $0 \mu\text{m}$ to $5 \mu\text{m}$, the resonance frequency decreases slowly from 1.358 THz to 1.335 THz, different than Figure 5.13. In fact, in both cases, the overlapping areas of the neighboring rings are clearly the same and so for current distributions; hence the mutual inductances between two layers are expected to be identical. Depending on the supporting information, the blue-shift observed in Figure 5.13 is supposed to be mainly the effect of small capacitive interactions.

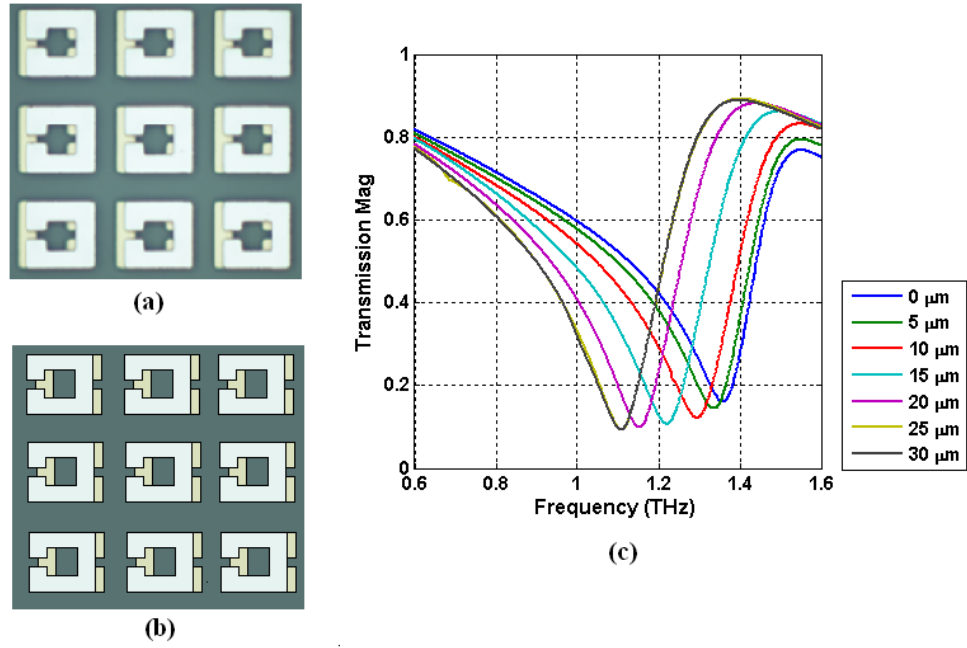


Figure 5.23: (a) Optical microscope picture of fabricated BC-SRR structure horizontally shifted for $5 \mu\text{m}$. (b) Schematic view of BC-SRR structure horizontally shifted in opposite direction for $5 \mu\text{m}$. (c) Simulation results for BC-SRR structures horizontally shifted in opposite direction for $0 \mu\text{m}$, $5 \mu\text{m}$, $10 \mu\text{m}$, $15 \mu\text{m}$, $20 \mu\text{m}$, $25 \mu\text{m}$, and $30 \mu\text{m}$.

In summary, we have demonstrated the use of tunable metamaterial designs based on near-field coupling effects between two different layers. We have designed, fabricated, and characterized vertically and horizontally shifted versions of BC-SRR structures together with the vertically shifted gap-to-gap oriented SRR structure. Among all our three designs, the superior tunability results have been observed for the vertically shifted BC-SRR design, which promises 663 GHz absolute shift (i.e. 51 %) in experiments. Besides, horizontally shifted BC-SRR and vertically shifted gap-to-gap oriented SRR designs experimentally promises 270 GHz (i.e. 20 %) and 138 GHz (i.e. 15 %) maximum shifts, respectively. These results demonstrate the use of structural tunability in THz region and may pave the way for further tunable metamaterial applications.

CHAPTER 6

METAMATERIAL SENSOR APPLICATIONS USING BROADSIDE-COUPLED SRR AND V-SHAPED RESONATOR STRUCTURES

6.1 Introduction

Resonance frequencies of the metamaterial resonator structures are very sensitive to the changes in capacitive and inductive effects since their fundamental resonance behavior can be modeled by an LC resonant circuit. This property makes them a natural candidate for metamaterial sensor applications. The capacitive effects are basically dependent on the substrate parameters (i.e. permittivity and thickness) and the topology. For example, for the conventional two-ring SRR topology, the gaps on the rings and separation between the rings provide capacitive effects as the functions of substrate thickness and permittivity. On the other hand, the inductive effects are mainly determined by the dimensions of metallic inclusions and their positions with respect to each other. It is important to note that the type of excitation has also a significant effect on both capacitance and inductance terms.

There are only a few reported studies on metamaterial sensor applications in literature. The first study is reported by Ishimaru et al. in 2005. They proposed an optical surface plasmon resonance (SPR) sensor application in microwave region using metamaterials [149]. In 2008, an application of SPR sensor in THz region was given by Arbabi et al. [150]. Also in 2008, Ekmekci et al. proposed a metamaterial sensor model based on the use of double-sided SRR (DSRR) structure for microwave region [109]. In 2010, Melik et al. experimentally demonstrated an RF-MEMS and nested SRR based wireless strain measurement setup [151]. Lastly, He et al. presented a thin-layer sensor with tip-shaped SRR for microwave regime

[152]. Thin-layer sensors are important especially for chemistry and biology to identify the presence, amounts or concentrations of substances [152].

In this study, we propose two different metamaterial sensor models based on two different double-sided topologies:

In the first part, we demonstrate the feasibility of using the BC-SRR type metamaterial structure for pressure, temperature and concentration sensor applications in microwave and terahertz regions. In fact, the ordinary SRR can also be used for such sensor applications. However, double-sided designs (i.e. BC-SRR and DSRR) were demonstrated in Chapter 3 and [13, 64] to promise much better sensitivities to the changes in substrate thicknesses than the conventional SRR. For the microwave region sensor design, we prefer to excite the BC-SRR magnetically. Due to the BC-SRR's special geometry, its resonance frequency under magnetic excitation shows much better sensitivity to the changes in substrate parameters (i.e. thickness and permittivity) as compared to the resonance frequency observed under electric excitation [24, 104]. Since the metamaterial structures are frequency scalable, this sensor design will still be valid in terahertz region. However, due to the experimental difficulty of providing magnetic excitation in terahertz region, the structures are most generally excited electrically [99]. Hence, an electrically excited version of the BC-SRR based sensor model is also presented here for THz metamaterial applications as a novel contribution on this area.

In the second part of this chapter, we demonstrate the use of V-shaped metamaterial structure for a pressure sensor application. V-shaped resonator is a double-sided structure which was introduced by Ekmekci et al. in 2007 as a novel metamaterial resonator [67, 107, 111]. Due to its special geometry, shifting one layer in lateral direction while keeping the other constant, the structure promises a significant shift in resonance frequency.

6.2 BC-SRR Based Metamaterial Sensor Applications

6.2.1 Behavior of the Ordinary BC-SRR Structure Under Magnetic and Electric Excitation

Before directly going into the BC-SRR based sensor model, it will be meaningful to understand the behavior of the conventional BC-SRR structure under magnetic and electric exci-

tations. Thus, we design and simulate the BC-SRR structure for different values of substrate thickness and permittivity under magnetic and electric excitations. The design parameters and also the schematic views of BC-SRR structures under magnetic and electric excitations are shown in Figure 6.1(a), (b) and (c), respectively. For the square shaped unit-cell, the structure has periodicity $P = 5$ mm, metal side length $l = 3.5$ mm, gap width $g = 0.3$ mm, metal width $w = 0.5$ mm and metal thickness $t_m = 0.03$ mm. Herein, the substrate thickness t_{sub} and substrate relative permittivity ϵ_r are chosen as variables, whereas the substrate dielectric loss-tangent $\tan \delta_c = 0.003$. The metalization is made of copper with the conductivity $\sigma = 58 \times 10^6$ S/m.

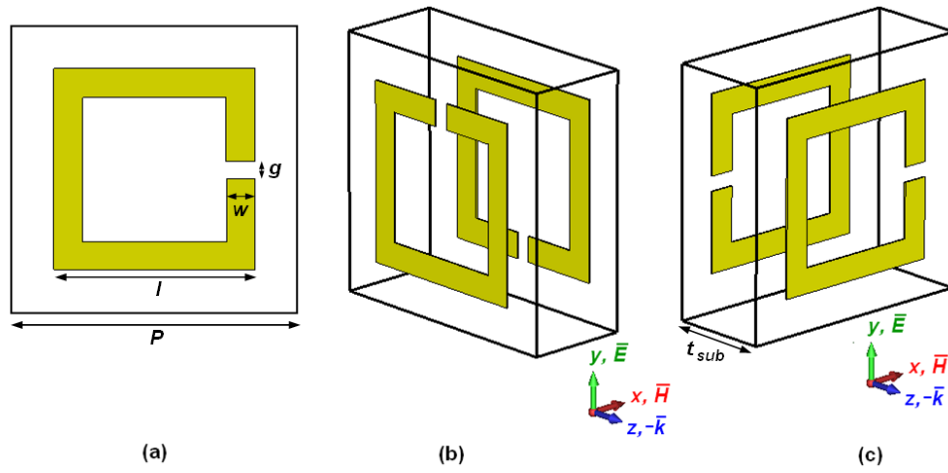
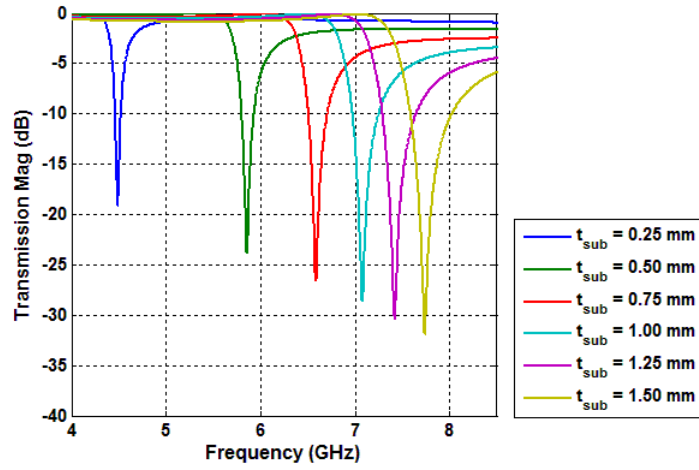


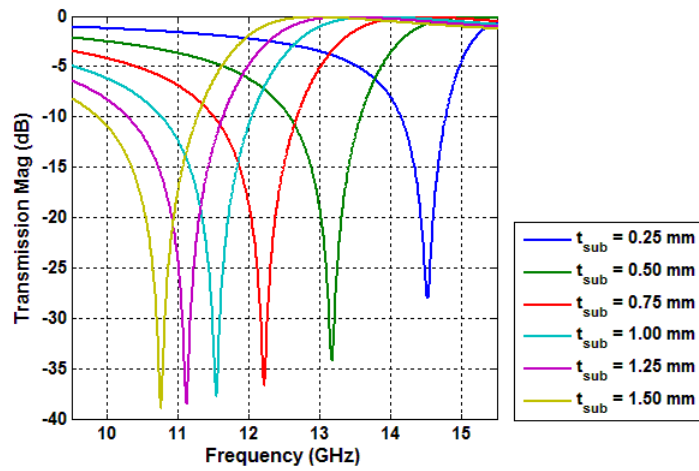
Figure 6.1: Schematic views of BC-SRR structure. (a) Top view with design parameters. (b) Magnetic excitation. (c) Electric excitation.

Transmission characteristics of the BC-SRR arrays are computed by using CST Microwave Studio using unit-cell boundary conditions (UC-BC) which provide periodicity along x and y directions. The structures are excited by an electromagnetic wave with the propagation vector \vec{k} along z direction, electric field vector \vec{E} along y direction, and magnetic field vector \vec{H} along x direction.

Figure 6.2 shows the computed transmission characteristics for a constant substrate permittivity at $\epsilon_r = 3$ and different values of substrate thickness under magnetic and electrical excitations. As we increase the substrate thickness t_{sub} from 0.25 mm to 1.50 mm, the resonance frequency of the magnetically excited BC-SRR increases from 4.49 to 7.79 GHz (i.e. 74 percent change), whereas the resonance frequency decreases from 14.52 GHz to 10.76 GHz (i.e. 26 % change) for the electrically excited BC-SRR case. For both cases, the rate of change



(a)

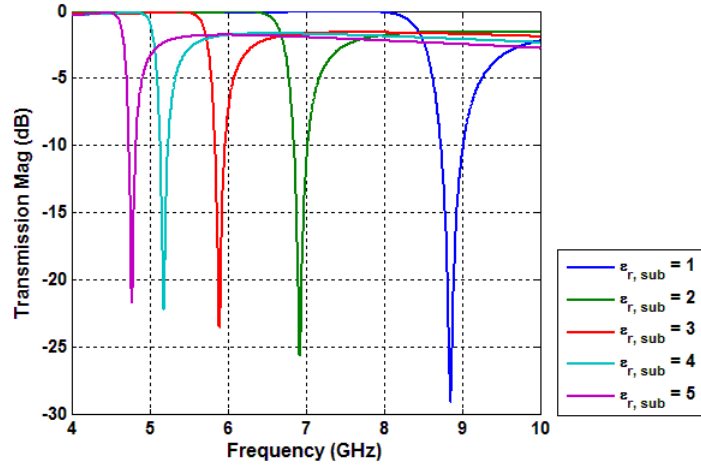


(b)

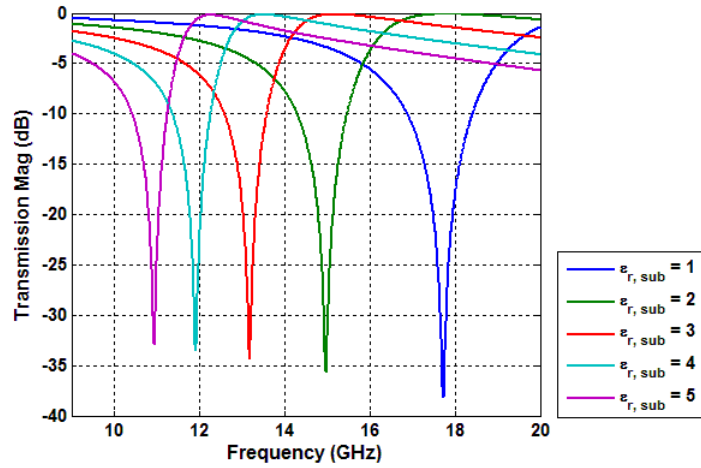
Figure 6.2: Effects of substrate thickness t_{sub} on the resonance frequency of BC-SRR under (a) magnetic and (b) electric excitations.

of resonance is much higher at lower t_{sub} values. These results also show that, magnetically excited BC-SRR is much more sensitive to the changes in substrate thicknesses than the electrically excited BC-SRR.

Figure 6.3 shows the computed transmission characteristics for a constant substrate thickness at $t_{sub} = 0.5$ mm and for different values of substrate permittivity under magnetic and electrical excitations. As we increase the substrate relative permittivity ϵ_r from 1 to 5, the resonance frequency of the magnetically excited BC-SRR decreases from 8.85 to 4.77 GHz (i.e. 46 % change), whereas the resonance frequency decreases from 17.72 GHz to 10.94 GHz (i.e. 38



(a)



(b)

Figure 6.3: Effects of relative permittivity of substrate ϵ_r on the resonance frequency of BC-SRR under (a) magnetic and (b) electric excitations.

% change) for the electrically excited BC-SRR case. For both cases, the frequency shifts are more significant for lower ϵ_r values. These results show that, magnetically excited BC-SRR is more sensitive to the changes in substrate thicknesses than the electrically excited BC-SRR.

6.2.2 Electromagnetic Response of BC-SRR Under Magnetic and Electric Excitation

To gain insight into the electromagnetic response of BC-SRR structure, we qualitatively examine the current and charge distributions of the top and bottom layers of a single unit cell under electrical and magnetic excitation. In the following, we consider exclusively the *LC*

resonance of the structure where $w_0 = 1 / \sqrt{L_{total}C_{total}}$ (i.e. not the higher frequency dipolar resonances). Figure 6.4(a) shows that under magnetic excitation, the surface currents of the top and bottom layers are in the same direction. This results in a mutual inductance (L_{mut}) with a positive sign yielding a total inductance $L_{total} = L_{self} + L_{mut}$. For electrical excitation (Figure 6.4b), the surface currents are in opposite directions meaning that L_{mut} is negative resulting in a total inductance $L_{total} = L_{self} - L_{mut}$. Similarly, the surface charge distribution and subsequent mutual capacitance depends on the excitation conditions. For magnetic excitation, positive and negative charges between the two layers overlap resulting in a significant mutual capacitance. In contrast, for electrical excitation, negative charges overlap with negative and positive charges overlap with positive between the two layers yielding a much weaker or negligible mutual capacitance.

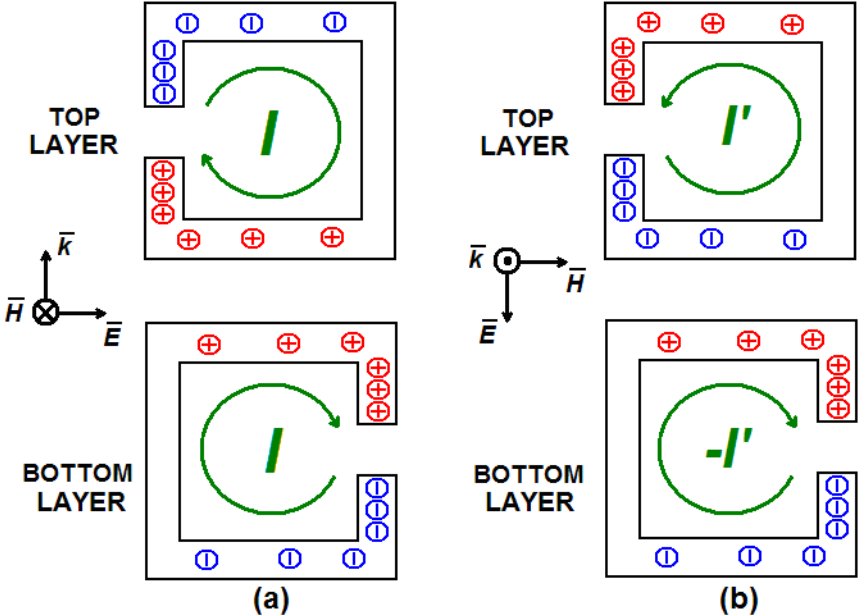


Figure 6.4: Schematic views of the surface charge distributions and their corresponding surface current distributions for (a) magnetically and (b) electrically excited BC-SRR structures. The top and bottom layers are shown displaced for clarity.

6.2.3 BC-SRR Based Sensor Model

The proposed BC-SRR based sensor model is shown in Figure 6.5. Herein, Figure 6.5(a) shows the perspective view of the model together with two excitation techniques and Figure 6.5(b) shows the side view. In this model, the BC-SRR structure is composed of two identical

single ring SRR structures printed on two different substrates where each substrate having relative permittivity ϵ_{sub} and substrate thickness d_s . These two substrates are separated from each other by an inter-layer dielectric with the variable thickness of d_i and variable relative permittivity of ϵ_{int} . If we choose $d_i = 0$, then the structure will converge to an ordinary BC-SRR having substrate thickness of $2d_s$.

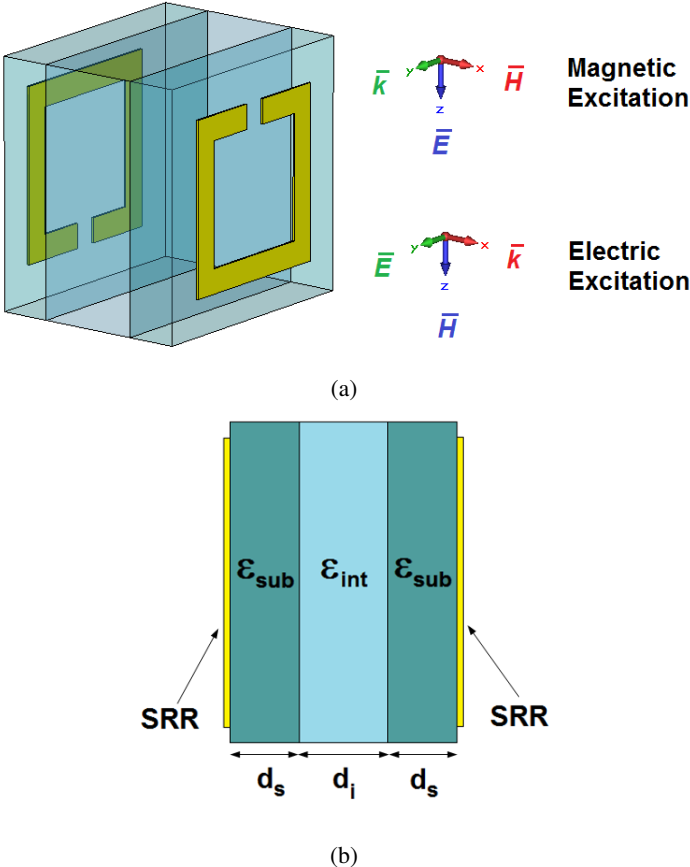


Figure 6.5: Schematic view of BC-SRR based sensor. (a) Perspective view and the directions of the vector fields for magnetic and electric excitations. (b) Side view.

6.2.4 BC-SRR Based Sensor for Microwave Region Using Magnetic Excitation

For the microwave region applications, BC-SRR sensor model is excited magnetically as shown in Figure 6.5(a). For the square shaped unit cell, the structure has periodicity $P = 5$ mm, metal side length $l = 3.5$ mm, gap width $g = 0.5$ mm, metal width $w = 0.5$ mm and metal thickness $t_m = 0.03$ mm. The substrate permittivity and thickness are set to $\epsilon_{sub} = 4.5$ and $d_s = 0.25$ mm, respectively. Interlayer permittivity ϵ_{int} and interlayer thickness d_i are the variables.

The metalization is made of copper with the conductivity $\sigma = 58 \times 10^6$ S/m.

Figure 6.6 shows the simulation results for the BC-SRR based metamaterial sensor under magnetic excitation in microwave region. In these simulations, the interlayer thicknesses d_i are changed from 0 mm (i.e. ordinary BC-SRR) to 1.4 mm with 0.1 mm incremental steps. Besides, the interlayer permittivity values ϵ_{int} are changed from 1 to 5 with 1 incremental steps. Being consistent with the results shown in Chapter 3 and [13, 104], the resonance frequency of the structure increases as d_i increases. The increase in the resonance frequency is clearly more dramatic for the interlayer thicknesses lower than 0.2 mm. In other words, the sensor is most sensitive to the changes in d_i which are lower than 0.2 mm. Moreover, the resonance frequency of the structure decreases as ϵ_{int} values increase. The decrease in the resonance frequency is largest from $\epsilon_{int} = 1$ to $\epsilon_{int} = 2$. In other words, the sensor is most sensitive to the changes in ϵ_{int} which are in between 1 and 2. The sensitivity of the sensor decreases as both d_i and ϵ_{int} increases.

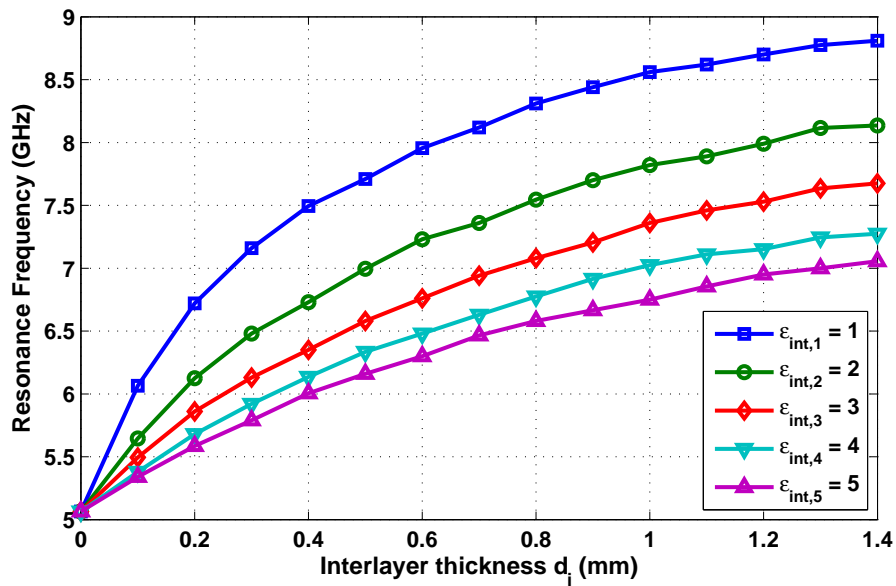


Figure 6.6: Effects of the interlayer thickness (d_i) and permittivity (ϵ_{int}) on the resonance frequency of BC-SRR based metamaterial sensor under magnetic excitation in microwave region.

6.2.5 BC-SRR Based Sensor for Terahertz Region Using Electric Excitation

For the terahertz region applications, BC-SRR sensor model is excited electrically as shown in Figure 6.5(a). For the square shaped unit cell, the structure has periodicity $P = 50 \mu\text{m}$, metal side length $l = 40 \mu\text{m}$, gap width $g = 3 \mu\text{m}$, metal width $w = 3 \mu\text{m}$ and metal thickness $t_m = 0.3 \mu\text{m}$. The substrate permittivity and thickness are set to $\epsilon_{sub} = 2.88$ and $d_s = 1 \mu\text{m}$, respectively. Interlayer permittivity ϵ_{int} and interlayer thickness d_i are the variables. The metalization is made by means of gold with the conductivity $\sigma = 45.2 \times 10^6 \text{ S/m}$.

Figure 6.7 shows the simulation results for the BC-SRR based metamaterial sensor under electric excitation in terahertz region. In these simulations, the interlayer thicknesses d_i are changed from $0 \mu\text{m}$ (i.e. ordinary BC-SRR) to $20 \mu\text{m}$ with $1 \mu\text{m}$ incremental steps. Besides, the interlayer permittivity values ϵ_{int} are chosen as 1, 3, 6, 9, and 12. Herein, the resonance frequency of the structure decreases as d_i increases as it is explained in Section 6.2.2. The decrease in the resonance frequency is clearly more dramatic for the interlayer thicknesses lower than $2 \mu\text{m}$. In other words, the sensor is most sensitive to the changes in d_i which are lower than $2 \mu\text{m}$. Moreover, the resonance frequency of the structure decreases as ϵ_{int} values increase. The decrease in the resonance frequency is largest from $\epsilon_{int} = 1$ to $\epsilon_{int} = 2$. In other words, the sensor is most sensitive to the changes in ϵ_{int} which are in between 1 and 2. The sensitivity of the sensor decreases as both d_i and ϵ_{int} increases.

6.3 A V-Shaped Resonator Based Pressure Sensor Application

In this part, we propose a novel metamaterial pressure sensor which consist of V-shaped resonator structures. The principle of operation is based on the inductive and capacitive coupling between two V-shaped structures which form a double-sided structure as shown in Figure 6.8. Herein, the aim is to measure an applied pressure by observing the changes in the resonance frequency. The design parameters of the V-shaped unit cell is shown in Figure 6.9. The unit cell structure has periodicity $P = 6 \text{ mm}$, metal width $w = 0.3 \text{ mm}$, metal thickness $t_m = 0.035 \text{ mm}$, substrate thickness $t_{sub} = 0.25 \text{ mm}$, substrate relative permittivity $\epsilon_r = 4.5$, and substrate loss-tangent $\tan \delta_c = 0.003$. The other design parameters are; $d_1 = 1.2 \text{ mm}$, $d_2 = 1.575736 \text{ mm}$, $d_3 = 2 \text{ mm}$, $d_4 = 1.075736 \text{ mm}$.

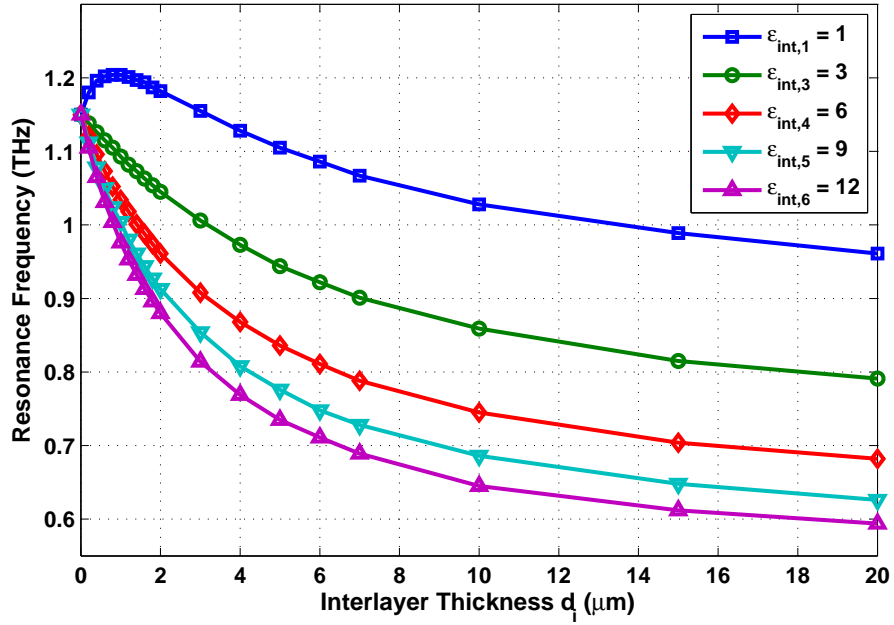


Figure 6.7: Effects of the interlayer thickness (d_i) and permittivity (ϵ_{int}) on the resonance frequency of BC-SRR based metamaterial sensor under electric excitation in terahertz region.

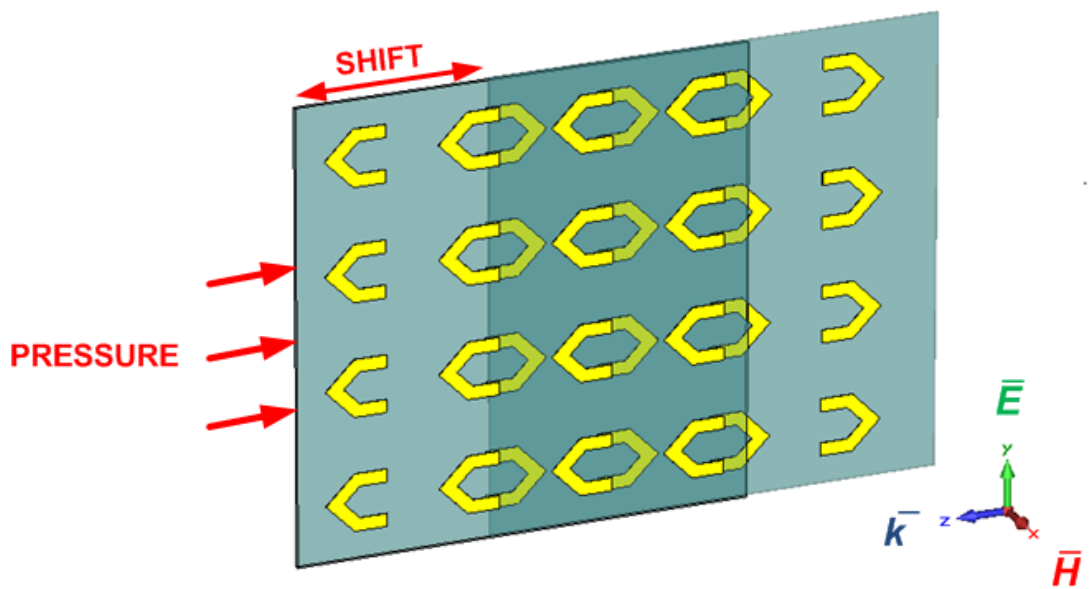


Figure 6.8: Schematic representation for the mechanism of V-shaped resonator based sensor application.

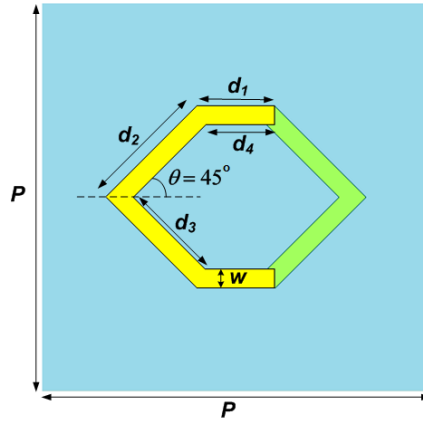


Figure 6.9: Design parameters of the V-shaped unit cell structure.

As the proof of concept, we shift one layer with respect to the other for $l_{shift} = 0, 0.2, 0.4, 0.6, 0.8, 1.0, 1.2, 1.4$ mm and compute their corresponding transmission characteristics which are given in Figure 6.10. For a better visualization, Figure 6.11 shows the schematic views of the unit cell topologies at $l_{shift} = 0, 0.4, 0.8, 1.2, 1.6$ mm. According to these results, resonance frequency of the V-shaped array increases from 9.95 GHz to 15.39 GHz, as we increase l_{shift} from 0 to 1.4 mm which corresponds to 55 % frequency shift.

6.4 Discussion

In this study, we have designed and simulated two different metamaterial sensor models based on the BC-SRR and V-shaped resonator topologies. The simulation results have shown that:

- BC-SRR topology can be used as a pressure sensor, by observing the changes in the resonance frequency resulting from the changes in the interlayer thickness.
- BC-SRR topology can be used as a temperature, humidity, or concentration sensor, by observing the changes in the resonance frequency resulting from the changes in the permittivity of the interlayer.
- V-shaped topology can be used as a pressure sensor, by observing the changes in the resonance frequency related to the changes of lateral shift amounts l_{shift} .

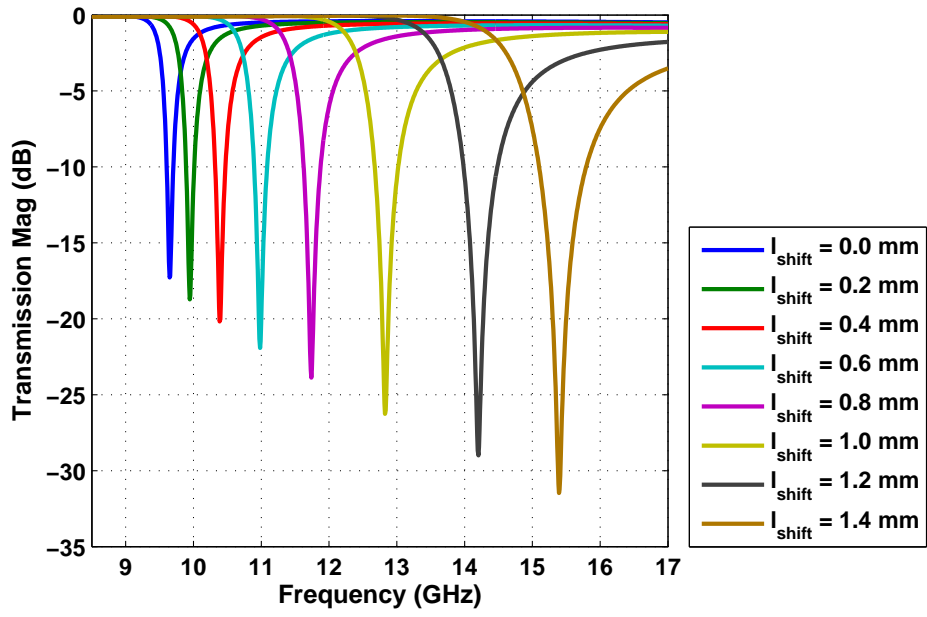


Figure 6.10: Transmission spectra of the V-sensor for different shift values.

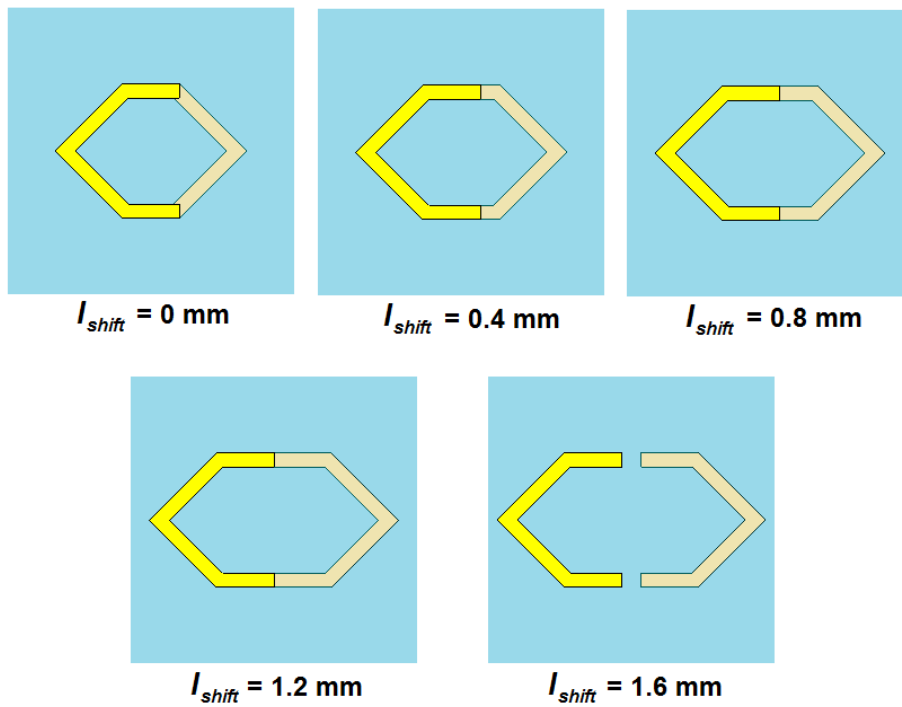


Figure 6.11: V-Sensor topologies for different lateral shift amounts.

CHAPTER 7

CONCLUSION AND FUTURE WORKS

This dissertation presents the results for the design, fabrication and characterization of novel metamaterial topologies in microwave and terahertz region. Based on the outline of the thesis, the basic conclusions can be summarized as follows:

In the first part of this Chapter 3, we have proposed a new μ -negative (MNG) metamaterial structure, the double-sided SRR (DSRR), which combines the topological properties of the previously suggested BC-SRR and the conventional SRR to reduce the resonance frequency (i.e. to reduce the electrical size) for a given set of unit cell dimensions. In other words, the DSRR structure is able to provide better miniaturization in RF design applications. The suggested DSRR topology has also been demonstrated as having a much wider half power resonance bandwidth as compared to the conventional SRR structure. The bandwidth performance of the DSRR cell approaches to that of the BC-SRR cell as the separation between the inner and outer rings increases. Full-wave electromagnetic simulations by HFSS have also demonstrated that the depth of the resonance curve increases as the substrate gets thicker. Finally, the combination of the DSRR cell and a conducting strip has shown to provide a left-handed metamaterial behavior, as expected. A simple equivalent circuit model is also proposed and verified to approximately describe the relation between substrate parameters (substrate thickness and substrate relative permittivity) and the resonance frequency. One international journal paper [13], one international conference paper [64] and one national conference paper [76] have been published based on this study.

In the second part of Chapter 3, electrically-small multi-ring magnetic resonators are investigated. It has already been shown in literature that multiple SRR (MSRR) structures and spiral resonators (SR) with large number of rings provide better miniaturization [12, 15, 16, 17, 18]

as compared to the conventional SRRs. Improved double-sided versions of these resonator topologies are suggested as novel contributions of this dissertation study. The simulation results for MSRR, double-sided MSRR, SR, double-sided SR, U-Spiral resonator (USR), and double-sided USR having various N numbers have been presented and the effects of both increasing N and doubling the resonator structure have been demonstrated. For example, increasing N from 2 to 6 for the MSRR, SR, USR, DMSRR, DSR, and DUSR structures caused their electrical size and resonance frequency values changed to 75 %, 38 %, 52 %, 76 %, 27 %, and 31 % of their initial values, respectively. Besides, doubling a six-turn MSRR, a six-turn SR, and a six-ring USR reduced their electrical size (u) and resonance frequency (f_0) values to 76 %, 52 %, and 35 % of their initial values, respectively. Here it is important to note that all these structures have the same unit cell size. Among all the structures investigated in this part, the electrically largest resonator is the two-turn MSRR (i.e. the conventional two-ring SRR) with $u = \lambda_0 / 12$ and $f_0 = 2.24$ GHz while the electrically smallest one is the six-turn DUSR with $u = \lambda_0 / 133$ and $f_0 = 0.20$ GHz. In other words, the double-sided U-type spiral resonator (DUSR) with $N = 6$ turns has an electrical size which is only 9 percent of the electrical size of the multi Split Ring Resonator (MSRR) with $N = 2$ turns, although both structures have the same physical cell size. One international conference paper has been published based on this study [16] and a manuscript is under preparation to be submitted to an international journal.

In the first part of Chapter 4, we have proposed the micro-split SRR (MSSRR) type unit cell array structures to be used for multi-band and tunable metamaterial design. The on/off state of the extremely narrow additional splits of MSSRRs can be efficiently controlled in microwave frequencies by proper switching techniques such as the RF MEMS switching technique. We have demonstrated that the resonance frequency of a MSSRR array can be easily increased by additional micro-splits which effectively reduce the equivalent capacitance of the SRR unit cell. Next, we have investigated the transmission properties of the double layer and triple layer homogeneous or inhomogeneous MSSRR arrays to demonstrate the feasibility of multiple frequency band metamaterial designs. For this purpose, dual-band and triple-band resonator structures have been designed, simulated, constructed and experimentally tested over the X-band microwave frequencies with quite satisfactory agreement between simulations and measurements. Also, an electrically smaller triple-band composite MSSRR super cell is designed and simulated. The effective permittivity and effective permeability parameters are retrieved for this design revealing the presence of magnetic resonances at the resonance

frequencies around 9.4 GHz, 10.5 GHz and 11.4 GHz, as expected. One international journal paper [23], two international conference papers [103, 106], and one national conference paper [110] have been published based on this study.

In the second part of Chapter 4, based on the simulation results obtained by two different full-wave electromagnetic solvers (Ansoft HFSS and CST MWS), the novel single loop resonator (SLR) structure proposed in this study is demonstrated to have three distinct resonance frequencies in microwave region. The structure is shown to have negative permeability over two closely located but distinct bands in the vicinity of its magnetic resonance frequencies. Therefore, the SLR topology lends itself as a useful alternative to the well-known SRR and SR structures especially when an electrically small dual-band magnetic resonator operation is needed. One international journal paper [74], and one international conference paper [105] have been published based on these results.

In Chapter 5, some frequency tunable metamaterial designs at terahertz (THz) frequencies using broadside-coupled SRR (BC-SRR) and gap-to-gap SRR arrays are presented. In those designs frequency tuning, arising from changes in near field coupling, is obtained by in-plane horizontal or vertical displacements of the two SRR layers. For electrical excitation, the resonance frequency continuously redshifts as a function of displacement. The maximum frequency shift occurs for displacement of half a unit cell, with vertical displacement of BC-SRR array resulting in a shift of 663 GHz (51 % of the resonance frequency) and horizontal displacement yielding a shift of 270 GHz (20 % of the resonance frequency), experimentally. Additionally, a maximum shift of 138 GHz (i.e. 15 %) for vertically shifted gap-to-gap SRR design is obtained both numerically and experimentally. Moreover, significant differences observed in the tuning results of BC-SRR and gap-to-gap SRR arrays due to the use of different excitation techniques (electrical excitation versus magnetic excitation) are discussed. An international conference paper has already been published based on this study. There is also an international journal manuscript written on this topic, which is currently in peer-review process and its basic content is available as an internet archive file [24]. Also there is another manuscript in preparation to be submitted to an international journal.

Finally in Chapter 6, the use of BC-SRR metamaterial topology sensors is suggested for pressure, temperature, humidity, and concentration sensor applications. Feasibility of such sensors are demonstrated by numerical simulations for both microwave and terahertz regions

using magnetic and electric excitations, respectively. Also, the novel V-Shaped resonator structure is introduced and suggested for pressure sensor applications. One international and three national conference papers have already been published based on this study. There are also two manuscripts in preparation to be submitted to international journals.

As future work research topics:

- Circuit modeling of BC-SRR and gap-to-gap oriented arrays considering the capacitive and inductive coupling effects among neighboring unit cells.
- Realization of the metamaterial sensor applications using BC-SRR structure.
- Realization of the metamaterial pressure sensor application using V-shaped resonator structure.

Following the completion of this dissertation study, the BC-SRR based and V-shaped resonator based sensor topologies will be realized as future work. Also, the equivalent circuit models for BC-SRR and gap-to-gap oriented SRR arrays will be developed by including the capacitive and inductive coupling effects among neighboring unit cells into the resonance models.

REFERENCES

- [1] V. G. Veselago, "The electrodynamics of substances with simultaneously negative values of ϵ and μ ," *Sov. Phys. Usp.*, vol. 10, no. 4, pp. 509–514, 1968.
- [2] J. B. Pendry, A. J. Holden, W. J. Stewart, and I. Youngs, "Extremely low frequency plasmons in metallic mesostructures," *Phys. Rev. Lett.*, vol. 76, no. 25, pp. 4773–4776, 1996.
- [3] J. B. Pendry, A. J. Holden, D. J. Robbins, and W. J. Stewart, "Low frequency plasmons in thin-wire structures," *J.Phys.:Condens. Matter*, vol. 10, pp. 4785–4809, 1998.
- [4] J. B. Pendry, A. J. Holden, D. J. Robbins, and W. J. Stewart, "Magnetism from conductors and enhanced nonlinear phenomena," *IEEE Trans. Microwave Theory Tech.*, vol. 47, no. 11, pp. 2075–2084, 1999.
- [5] D. R. Smith, W. J. Padilla, D. C. Vier, S. C. Nemat-Nasser, and S. Schultz, "Composite medium with simultaneously negative permeability and permittivity," *Phys. Rev. Lett.*, vol. 84, no. 18, pp. 4184–4187, 2000.
- [6] R. A. Shelby, D. R. Smith, and S. Schultz, "Experimental verification of a negative index of refraction," *Science*, vol. 292, pp. 77–79, 2001.
- [7] D. R. Smith and N. Kroll, "Negative refractive index in left handed materials," *Phys. Rev. Lett.*, vol. 85, no. 14, pp. 2933–2936, 2000.
- [8] D. R. Smith, D. Schurig, and J. B. Pendry, "Negative refraction of modulated electromagnetic waves," *Appl. Phys. Lett.*, vol. 81, no. 15, pp. 2713–2715, 2002.
- [9] G. Shvets, "Photonic approach to making a material with a negative index of refraction," *Phys. Rev. B*, vol. 67, p. 035109, 2003.
- [10] J. B. Pendry and D. R. Smith, "Reversing light with negative refraction," *Phys. Today*, pp. 37–43, June 2004.
- [11] R. Marqués, F. Medina, and R. Rafii-El-Idrissi, "Role of bianisotropy in negative permeability and left-handed metamaterials," *Phys. Rev. B*, vol. 65, p. 14440, 2002.
- [12] F. Bilotti, A. Toscano, L. Vegni, K. Aydin, K. B. Alici, and E. Ozbay, "Equivalent-circuit models for the design of metamaterials based on artificial magnetic inclusions," *IEEE Trans. Microw. Theory Tech.*, vol. 55, no. 12, pp. 2865–2873, 2007.
- [13] E. Ekmekci and G. Turhan-Sayan, "Comparative investigation of resonance characteristics and electrical size of the double-sided SRR, BC-SRR, and conventional SRR type metamaterials for varying substrate parameters," *Prog. Electromagn. Res. B*, vol. 12, pp. 35–62, 2009.
- [14] J. D. Baena, R. Marqués, F. Medina, and J. Martel, "Artificial magnetic metamaterial design by using spiral resonators," *Phys. Rev. B*, vol. 69, p. 014402, 2004.

- [15] K. B. Alici, F. Bilotti, L. Vegni, and E. Ozbay, “Miniaturized negative permeability materials,” *Appl. Phys. Lett.*, vol. 91, p. 071121, 2007.
- [16] E. Ekmekci and G. Turhan-Sayan, “Reducing the electrical size of magnetic metamaterial resonators by geometrical modifications: A comparative study for single-sided and double-sided multiple SRR, spiral and U-spiral resonators,” in *Proc. IEEE AP-S International Symposium on Antennas and Propagation*, San Diego, CA, USA, July 2008.
- [17] F. Aznar, M. Gil, J. Bonache, J. García-García, and F. Martin, “Metamaterial transmission lines based on broad-side coupled spiral resonators,” *Electron. Lett.*, vol. 43, no. 9, pp. 530–532, 2007.
- [18] F. Aznar, J. García-García, M. Gil, J. Bonache, and F. Martin, “Strategies for the miniaturization of metamaterial resonators,” *Microw. Opt. Technol. Lett.*, vol. 50, no. 5, pp. 1263–1270, 2008.
- [19] J. D. Baena, J. Bonache, F. Martín, R. M. Sillero, F. Falcone, T. Lopetgi, M. A. G. Laso, J. García-García, I. Gil, M. F. Portillo, and M. Sorolla, “Equivalent-circuit models for split-ring resonators and complementary split-ring resonators coupled to planar transmission lines,” *IEEE Trans. Microw. Theory Tech.*, vol. 53, no. 4, pp. 1451–1461, 2005.
- [20] F. Bilotti, A. Toscano, and L. Vegni, “Design of spiral and multiple split-ring resonators for the realization of miniaturized metamaterial samples,” *IEEE Trans. Antennas Propag.*, vol. 55, no. 8, pp. 2258–2267, 2007.
- [21] T. J. Cui, H. F. Ma, R. Liu, B. Zhao, Q. Cheng, and J. Y. Chin, “A symmetrical circuit model describing all kinds of circuit metamaterials,” *Prog. Electromagn. Res. B*, vol. 5, pp. 63–76, 2008.
- [22] P. Yasar-Orten, E. Ekmekci, and G. Turhan-Sayan, “Equivalent circuit models for split-ring resonator arrays,” in *Proc. PIERS 2010 in Cambridge*, Cambridge, MA, USA, July 2010, pp. 534–537.
- [23] E. Ekmekci, K. Topalli, T. Akin, and G. Turhan-Sayan, “A tunable multi-band metamaterial design using micro-split SRR structures,” *Opt. Express*, vol. 17, no. 18, pp. 16 046–16 058, 2009.
- [24] E. Ekmekci, A. C. Strikwerda, K. Fan, X. Zhang, G. Turhan-Sayan, and R. D. Averitt, “Far-infrared frequency tunable metamaterials using broadside-coupled split ring resonators,” *arXiv:1008.2195v1 [physics.optics]*, 2010.
- [25] F. Zhang, Q. Zhao, W. Zhang, J. Sun, J. Zhou, and D. Lippens, “Voltage tunable short wire-pair type of metamaterial infiltrated by nematic liquid crystal,” *Appl. Phys. Lett.*, vol. 97, no. 13, p. 134103, 2010.
- [26] K. Aydin and E. Ozbay, “Capacitor-loaded split ring resonators as tunable metamaterial components,” *J. Appl. Phys.*, vol. 101, p. 024911, 2007.
- [27] D.-Y. Zou, A.-M. Jiang, and R.-X. Wu, “Ferromagnetic metamaterial with tunable negative index of refraction,” *J. Appl. Phys.*, vol. 107, p. 013507, 2010.

- [28] T. Hand and S. Cummer, “Characterization of tunable metamaterial elements using MEMS switches,” *IEEE Antennas Wirel. Propag. Lett.*, vol. 6, pp. 401–404, 2007.
- [29] H. T. Chen, J. F. O’Hara, A. K. Azad, A. J. Taylor, R. D. Averitt, D. Shrekenhamer, and W. J. Padilla, “Experimental demonstration of frequency agile terahertz metamaterials,” *Nat. Photonics*, vol. 2, no. 5, pp. 295–298, 2008.
- [30] K. A. Boulais, D. W. Rule, S. Simmons, F. Santiago, V. Gehman, K. Long, and A. Rayms-Keller, “Tunable split-ring resonator for metamaterials using photocopacitance of semi-insulating GaAs,” *Appl. Phys. Lett.*, vol. 93, p. 043518, 2008.
- [31] R. Marqués, F. Mesa, J. Martel, and F. Medina, “Comparative analysis of edge- and broadside-coupled split ring resonators for metamaterial design-theory and experiments,” *IEEE Trans. Antennas Propag.*, vol. 51, no. 10, pp. 2572–2581, 2003.
- [32] C. R. Simovski, P. A. Belov, and S. He, “Backward wave region and negative material parameters of a structure formed by lattices of wires and split-ring resonators,” *IEEE Trans. Antennas Propag.*, vol. 51, no. 10, pp. 2582–2591, 2003.
- [33] T. Koschny, L. Zhang, and C. M. Soukoulis, “Isotropic three-dimensional left-handed metamaterials,” *Phys. Rev. B*, vol. 71, p. 121103(R), 2005.
- [34] D. R. Smith, J. Gollub, J. J. Mock, W. J. Padilla, and D. Schurig, “Calculation and measurement of bianisotropy in a split ring resonator metamaterial,” *J. Appl. Phys.*, vol. 100, p. 024507, 2006.
- [35] D. K. Ghodgaonkar, V. V. Varadan, and V. K. Varadan, “Free-space measurement of complex permittivity and complex permeability of magnetic materials at microwave frequencies,” *IEEE Trans. Instrum. Meas.*, vol. 39, no. 2, pp. 387–394, 1990.
- [36] D. R. Smith, D. C. Vier, T. Koschny, and C. M. Soukoulis, “Electromagnetic parameter retrieval from inhomogeneous metamaterials,” *Phys. Rev. E*, vol. 71, p. 036617, 2005.
- [37] R. Liu, T. J. Cui, D. Huang, B. Zhao, and D. R. Smith, “Description and explanation of electromagnetic behaviors in artificial metamaterials based on effective medium theory,” *Phys. Rev. E*, vol. 76, p. 026606, 2007.
- [38] D. R. Smith, “Analytic expressions for the constitutive parameters of magnetoelectric metamaterials,” *Phys. Rev. E*, vol. 81, p. 036605, 2010.
- [39] R. Zhao, T. Koschny, and C. M. Soukoulis, “Chiral metamaterials: retrieval of the effective parameters with and without substrate,” *Opt. Express*, vol. 18, no. 14, pp. 14 553–14 567, 2010.
- [40] S. Larauche and D. R. Smith, “A retrieval method for nonlinear metamaterials,” *Opt. Commun.*, vol. 283, pp. 1621–1627, 2010.
- [41] J. B. Pendry, D. Schurig, and D. R. Smith, “Controlling electromagnetic fields,” *Science*, vol. 312, pp. 1780–1782, 2006.
- [42] D. Schurig, J. J. Mock, B. J. Justice, S. A. Cummer, J. B. Pendry, A. F. Starr, and D. R. Smith, “Metamaterial electromagnetic cloak at microwave frequencies,” *Science*, vol. 314, pp. 977–980, 2006.

- [43] B.-I. Popa and S. A. Cummer, “Design of layered transformation-optics devices of arbitrary shape,” *Phys. Rev. A*, vol. 82, no. 3, p. 033837, 2010.
- [44] O. Ozgun and M. Kuzuoglu, “Domain compression via anisotropic metamaterials designed by coordinate transformations,” *J. Comput. Phys.*, vol. 229, no. 3, pp. 921–932, 2010.
- [45] J. Renger, M. Kadic, G. Dupont, S. S. Acimović, S. Guenneau, R. Quidant, and S. Enoch, “Hidden progress: broadband plasmonic invisibility,” *Opt. Express*, vol. 18, no. 15, pp. 15 757–15 768, 2010.
- [46] E. Semouchkina, D. H. Werner, G. B. Semouchkin, and C. Pantano, “An infrared invisibility cloak composed of glass,” *Applied Physics Letters*, vol. 96, no. 23, p. 233503, 2010.
- [47] X. Wang, S. Qu, X. Wu, J. Wang, Z. Xu, and H. Ma, “Broadband three-dimensional diamond-shaped invisible cloaks composed of tetrahedral homogeneous blocks,” *J. Phys. D: Appl. Phys.*, vol. 43, no. 30, p. 305501, 2010.
- [48] J. B. Pendry, “Negative refraction makes a perfect lens,” *Phys. Rev. Lett.*, vol. 85, no. 18, pp. 3966–3969, 2000.
- [49] A. Grbic and G. V. Eleftheriades, “Subwavelength focusing using a negative-refractive-index transmission line lens,” *IEEE Antennas Wirel. Propag. Lett.*, vol. 2, pp. 186–189, 2003.
- [50] K. Aydin, I. Bulu, and E. Ozbay, “Subwavelength resolution with a negative-index metamaterial superlens,” *Appl. Phys. Lett.*, vol. 90, no. 25, p. 254102, 2007.
- [51] E. Ozbay, Z. Li, and K. Aydin, “Super-resolution imaging by one-dimensional, microwave left-handed metamaterials with an effective negative index,” *J. Phys. Condens. Matter*, vol. 20, p. 304216, 2008.
- [52] A. Iyer and G. Eleftheriades, “Free-space imaging beyond the diffraction limit using a Veselago-Pendry transmission-line metamaterial superlens,” *IEEE Trans. Antennas Propag.*, vol. 57, no. 6, pp. 1720–1727, 2009.
- [53] B. D. F. Casse, W. T. Lu, Y. J. Huang, E. Gultepe, L. Menon, and S. Sridhar, “Super-resolution imaging using a three-dimensional metamaterials nanolens,” *Appl. Phys. Lett.*, vol. 96, no. 2, p. 023114, 2010.
- [54] I. K. Kim and V. Varadan, “Electrically small, millimeter wave dual band meta-resonator antennas,” *IEEE Trans. Antennas Propag.*, vol. 58, no. 11, pp. 3458–3463, 2010.
- [55] P. Y. Chen and A. Alú, “Sub-wavelength elliptical patch antenna loaded with μ -negative metamaterials,” *IEEE Trans. Antennas Propag.*, vol. 58, no. 9, pp. 2909–2919, 2010.
- [56] S. Tricarico, F. Bilotti, and L. Vegni, “Multi-functional dipole antennas based on artificial magnetic metamaterials,” *IET Microw. Antennas Propag.*, vol. 4, no. 8, pp. 1026–1038, 2010.
- [57] G. V. Eleftheriades, O. Siddiqui, and A. K. Iyer, “Transmission line models for negative refractive index media and associated implementations without excess resonators,” *IEEE Microw. Wirel. Compon. Letters*, vol. 13, no. 2, pp. 51–53, 2003.

- [58] J. K. H. Wong, K. G. Balmain, and G. V. Eleftheriades, “Fields in planar anisotropic transmission-line metamaterials,” *IEEE Trans. Antennas Propag.*, vol. 54, no. 10, pp. 2742–2749, 2006.
- [59] C. Caloz and T. Itoh, *Electromagnetic Metamaterials: Transmission Line Theory and Microwave Applications*. New Jersey: Wiley-Interscience, 2006.
- [60] P. Gay-Balmaz and O. J. F. Martin, “Electromagnetic resonances in individual and coupled split-ring resonators,” *J. Appl. Phys.*, vol. 92, no. 5, pp. 2929–2936, 2002.
- [61] J. García-García, F. Martín, J. D. Baena, R. Marqués, and L. Jelinek, “On the resonances and polarizabilities of split ring resonators,” *J. Appl. Phys.*, vol. 98, p. 033103, 2005.
- [62] T. Weiland, R. Schuhmann, R. B. Gregor, C. G. Parazzoli, A. M. Vetter, D. R. Smith, D. C. Vier, and S. Schultz, “Ab initio numerical simulation of left-handed metamaterials: Comparison of calculation and experiments,” *J. Appl. Phys.*, vol. 90, no. 10, pp. 5419–5424, 2001.
- [63] K. Aydin, I. Bulu, K. Guven, M. Kafesaki, C. M. Soukoulis, and E. Ozbay, “Investigation of magnetic resonances for different split-ring resonator parameters,” *N. J. Phys.*, vol. 7, no. 168, pp. 1–15, 2005.
- [64] E. Ekmekci and G. Turhan-Sayan, “Sensitivity of the resonance characteristics of SRR and DSRR (Double-sided SRR) type metamaterials to the changes in substrate parameters and the usefulness of DSRR structure for reduced electrical size,” in *Proc. PIERS 2008 in Cambridge*, Cambridge, MA, USA, 2008, pp. 598–602.
- [65] B. Wu, B. Li, T. Su, and C.-H. Liang, “Equivalent-circuit analysis and lowpass filter design of split-ring resonator DGS,” *J. Electromagn. Waves and Appl.*, vol. 20, no. 14, pp. 1943–1953, 2006.
- [66] E. Ekmekci, K. Topalli, T. Akin, and G. Turhan-Sayan, “Effects of array dimensions on the resonance characteristics of srr type metamaterial arrays with small sizes: Simulations and experiments,” in *Proc. PIERS 2009 in Moscow, Russia*, August 2009, pp. 83–86.
- [67] E. Ekmekci and G. Turhan-Sayan, “Investigation of permittivity for a novel V-shaped metamaterial using simulated S-parameters,” in *Proc. International Conference on Electrical and Electronics Engineering ELECO, Bursa, Turkey*, 2007, pp. 251–254.
- [68] I. Bulu, H. Caglayan, and E. Ozbay, “Experimental demonstration of labyrinth-based left-handed metamaterials,” *Opt. Express*, vol. 13, no. 25, pp. 10 238–10 247, 2005.
- [69] E. Ozbay, I. Bulu, and H. Caglayan, “Transmission, reflection, and focusing properties of labyrinth based left-handed metamaterials,” *Phys. Status Solidi*, vol. 244, no. 4, pp. 1202–1210, 2007.
- [70] H. Chen, L. Ran, J. Huangfu, X. Zhang, K. Chen, and T. M. Grzegorzcyk, “Left-handed materials composed of only S-shaped resonators,” *Phys. Rev. E*, vol. 70, p. 057605, 2004.
- [71] H. S. Chen, L. X. Ran, J. T. Huangfu, X. M. Zhang, K. S. Chen, T. M. Grzegorzcyk, and J. A. Kong, “Magnetic properties of S-shaped split-ring resonators,” *Prog. Electromagn. Res.*, vol. 51, pp. 231–247, 2005.

- [72] B.-I. Wu, W. Wang, J. Pacheco, X. Chen, T. Grzegorzczuk, and J. A. Kong, "A study of using metamaterials as antenna substrate to enhance gain," *Prog. Electromagn. Res.*, vol. 51, pp. 295–328, 2005.
- [73] K. Aydin, Z. Li, M. Hudlička, S. A. Tretyakov, and E. Ozbay, "Transmission characteristics of bianisotropic metamaterials based on omega shaped metallic inclusions," *N. J. Phys.*, vol. 9, p. 326, 2007.
- [74] E. Ekmekci and G. Turhan-Sayan, "Single loop resonator: Dual-band magnetic metamaterial structure," *Electron. Lett.*, vol. 46, no. 5, pp. 324–325, 2010.
- [75] H. Zhao and T. J. Cui, "A double-spiral resonator structure to realize left-handed material with lower resonant frequency," *Microw. Opt. Technol. Lett.*, vol. 48, no. 5, pp. 923–926, 2006.
- [76] E. Ekmekci and G. Turhan-Sayan, "Çift taraflı yapı ile ayırık halkalı rezonatörün rezonans frekansının düşürülmesi," in *15.Yıl Mühendislik-Mimarlık Kongresi*, Isparta, Turkey, November 2007, pp. 36–40.
- [77] H. Chen, L. Ran, J. Huangfu, T. M. Grzegorzczuk, and J. A. Kong, "Equivalent circuit model for left-handed metamaterials," *J. Appl. Phys.*, vol. 100, p. 024915, 2006.
- [78] Z. Sheng and V. V. Varadan, "Tuning the effective properties of metamaterials by changing the substrate properties," *J. Appl. Phys.*, vol. 101, p. 014909, 2007.
- [79] Q. Zhao, L. Kang, B. Du, B. Li, J. Zhou, H. Tang, X. Liang, and B. Zhang, "Electrically tunable negative permeability metamaterials based on nematic liquid crystals," *Appl. Phys. Lett.*, vol. 90, p. 011112, 2007.
- [80] F. Zhang, L. Kang, Q. Zhao, J. Zhou, X. Zhao, and D. Lippens, "Magnetically tunable left handed metamaterials by liquid crystal orientation," *Opt. Express*, vol. 17, no. 6, pp. 4360–4366, 2009.
- [81] S. Xiao, U. K. Chettiar, A. V. Kildishev, V. Drachev, I. C. Khoo, and V. M. Shalaev, "Tunable magnetic response of metamaterials," *Appl. Phys. Lett.*, vol. 95, p. 033115, 2009.
- [82] A. Minovich, D. N. Neshev, D. A. Powell, I. V. Shadrivov, and Y. S. Kivshar, "Tunable fishnet metamaterials infiltrated by liquid crystals," *Appl. Phys. Lett.*, vol. 96, no. 19, p. 193103, 2010.
- [83] O. Reynet and O. Archer, "Voltage controlled metamaterial," *Appl. Phys. Lett.*, vol. 84, no. 7, pp. 1198–1200, 2004.
- [84] I. Gil, J. Bonache, J. García-García, and F. Martín, "Tunable metamaterial transmission lines based on varactor-loaded split-ring resonators," *IEEE Trans. Microw. Theory Tech.*, vol. 54, no. 6, pp. 2665–2674, 2006.
- [85] H. Chen, B. Wu, L. Ran, T. M. Grzegorzczuk, and J. A. Kong, "Controllable left-handed metamaterial and its application to steerable antenna," *Appl. Phys. Lett.*, vol. 89, p. 053509, 2006.
- [86] D. Wang, L. Ran, H. Chen, M. Mu, J. A. Kong, and B.-I. Wu, "Active left-handed material collaborated with microwave varactors," *Appl. Phys. Lett.*, vol. 91, p. 164101, 2007.

- [87] A. Vélez, J. Bonache, and F. Martín, “Varactor-loaded complementary split ring resonators (VLCSRR) and their application to tunable metamaterial transmission lines,” *IEEE Microw. Wirel. Compon. Letters*, vol. 18, no. 1, pp. 28–30, 2008.
- [88] L. Kang, Q. Zhao, H. Zhao, and J. Zhou, “Ferrite-based magnetically tunable left-handed metamaterial composed of SRRs and wires,” *Opt. Express*, vol. 16, no. 22, pp. 17 269–17 275, 2008.
- [89] G. He, R. xin Wu, Y. Poo, and P. Chen, “Magnetically tunable double-negative material composed of ferrite-dielectric and metallic mesh,” *J. Appl. Phys.*, vol. 107, no. 9, p. 093522, 2010.
- [90] L. Kang, Q. Zhao, H. Zhao, and J. Zhou, “Magnetically tunable negative permeability metamaterial composed by split ring resonators and ferrite rods,” *Opt. Express*, vol. 16, no. 12, pp. 8825–8834, 2008.
- [91] T. H. Hand and S. A. Cummer, “Frequency tunable electromagnetic metamaterial using ferroelectric loaded split rings,” *J. Appl. Phys.*, vol. 103, p. 066105, 2008.
- [92] M. Gil, C. Damm, A. Giere, M. Sazegar, J. B. amd R. Jakoby, and F. Martín, “Electrically tunable split-ring resonators at microwave frequencies based on barium-strontium-titanate thick films,” *Electron. Lett.*, vol. 45, no. 8, pp. 417–418, 2009.
- [93] J. Han, A. Lakhtakia, and C.-W. Qiu, “Terahertz metamaterials with semiconductor split-ring resonators for magnetostatic tunability,” *Opt. Express*, vol. 16, no. 19, pp. 14 390–14 396, 2008.
- [94] J. Han and A. Lakhtakia, “Semiconductor split ring resonators for thermally tunable terahertz metamaterials,” *J. Mod. Opt.*, vol. 56, no. 4, pp. 554–557, 2009.
- [95] I. Gil, F. Martín, X. Rottenberg, and W. D. Raedt, “Tunable stop-band filter at Q-band based on RF-MEMS metamaterials,” *Electron. Lett.*, vol. 43, no. 21, p. 1153, 2007.
- [96] X. Jun He, Y. Wang, J. Min Wang, and T.-L. Gui, “MEMS switches controlled multi-split ring resonator as a tunable metamaterial component,” *Microsyst. Technol.*, vol. 16, no. 11, pp. 1831–1837, 2010.
- [97] M. Tonouchi, “Cutting-edge terahertz technology,” *Nat. Photonics*, vol. 1, pp. 97–105, 2007.
- [98] G. P. Williams, “Filling the THz-gap high power sources and applications,” *Rep. Prog. Phys.*, vol. 69, pp. 301–326, 2006.
- [99] H. Tao, W. J. Padilla, X. Zhang, and R. D. Averitt, “Recent progress in electromagnetic metamaterial devices for terahertz applications,” *IEEE J. Sel. Top. Quantum Electron.*, 2010, accepted.
- [100] H. Tao, A. C. Strikwerda, K. Fan, C. M. Bingham, W. J. Padilla, X. Zhang, and R. D. Averitt, “Terahertz metamaterials on free-standing highly-flexible polyimide substrates,” *J. Phys. D. Appl. Phys.*, vol. 41, p. 232004, 2008.
- [101] C. M. Bingham, H. Tao, X. Liu, R. D. Averitt, X. Zhang, and W. J. Padilla, “Planar wallpaper group metamaterials for novel terahertz applications,” *Opt. Express*, vol. 16, no. 23, pp. 18 565–18 575, 2008.

- [102] H. Tao, A. C. Strikwerda, K. Fan, W. J. Padilla, X. Zhang, and R. D. Averitt, "Reconfigurable terahertz metamaterials," *Phys. Rev. Lett.*, vol. 103, p. 147401, 2009.
- [103] E. Ekmekci and G. Turhan-Sayan, "Use of SRR-based super-cells to obtain multiple resonances and broader frequency bands with negative effective permeability," in *Proc. IEEE AP-S International Symposium on Antennas and Propagation*, Toronto, ON, Canada, July 2010.
- [104] E. Ekmekci, R. D. Averitt, and G. Turhan-Sayan, "Effects of substrate parameters on the resonance frequency of double-sided SRR structures under two different excitations," in *Proc. PIERS 2010 in Cambridge, MA, USA*, July 2010, pp. 538–540.
- [105] E. Ekmekci and G. Turhan-Sayan, "A novel dual band metamaterial structure," in *Proc. PIERS 2009 in Moscow*, Moscow, Russia, August 2009.
- [106] E. Ekmekci, K. Topalli, T. Akin, and G. Turhan-Sayan, "A feasibility study for tunable metamaterial design using multi-split SRR structures and RF MEMS switching," in *Proc. IEEE AP-S International Symposium on Antennas and Propagation*, Charleston, SC., USA, June 2009.
- [107] E. Ekmekci and G. Turhan-Sayan, "V-Şekilli yapılarla yeni bir manyetik rezonatör uygulaması ve simülasyonu," in *IEEE 15. Sinyal İşleme ve İletişim Uygulamaları Kurultayı*, Eskişehir, Turkey, June 2007, pp. 751–753.
- [108] E. Ekmekci, K. Topalli, T. Akin, and G. Turhan-Sayan, "Ayrık halkalı rezonatörlerden oluşan metamateriyal dizi yapılarının deneysel olarak İncelenmesi," in *IEEE 17. Sinyal İşleme ve İletişim Uygulamaları Kurultayı*, Antalya, Turkey, April 2009, pp. 309–312.
- [109] E. Ekmekci and G. Turhan-Sayan, "Çift taraflı ayırık halkalı rezonatör yapısının metamateriyal sensör uygulamaları: Kuram ve benzetim," in *URSI-Türkiye 2008 4. Bilimsel Kongresi*, Antalya, Turkey, October 2008, pp. 62–65.
- [110] E. Ekmekci, K. Topalli, and G. Turhan-Sayan, "RF-MEMS anahtarlama tekniği ile AHR tipi metamalzemelerde manyetik rezonans frekansının adaptif biçimde ayarlanması," in *URSI-Türkiye 2008 4. Bilimsel Kongresi*, Antalya, Turkey, October 2008, pp. 106–109.
- [111] E. Ekmekci and G. Turhan-Sayan, "V-şekilli rezonatör ve iletken çubuklar kullanarak oluşturulan sol-elli yapının benzetimi, etkin ortam parametrelerinin çıkartılması ve rezonans frekansının kaydırılması," in *Elektrik Elektronik Bilgisayar Biyomedikal Mühendisliği 12. Ulusal Kongre ve Fuarı*, Eskişehir, Turkey, November 2007.
- [112] J. Pendry, "New electromagnetic materials emphasise the negative," *Physics World*, pp. 1–5, 2001.
- [113] D. R. Smith, D. C. Vier, N. Kroll, and S. Schultz, "Direct calculation of permeability and permittivity for a left-handed metamaterial," *Appl. Phys. Lett.*, vol. 77, no. 14, pp. 2246–2248, 2000.
- [114] G. Lubkowski, R. Schuhmann, and T. Weiland, "Extraction of effective metamaterial parameters by parameter fitting of dispersive models," *Microw. Opt. Technol. Lett.*, vol. 49, no. 2, pp. 285–288, 2007.

- [115] W. J. Padilla, A. J. Taylor, C. Highstrete, M. Lee, and R. D. Averitt, “Dynamical electric and magnetic metamaterial response at terahertz frequencies,” *Phys. Rev. Lett.*, vol. 96, p. 107401, 2006.
- [116] D. Schuring, J. J. Mock, and D. R. Smith, “Electric-field-coupled resonators for negative permittivity metamaterials,” *Appl. Phys. Lett.*, vol. 88, p. 041109, 2006.
- [117] R. Liu, A. Degiron, J. J. Mock, , and D. R. Smith, “Negative index material composed of electric and magnetic resonators,” *Appl. Phys. Lett.*, vol. 90, p. 263504, 2007.
- [118] S. Maslovski, P. Ikonen, I. Kolmakov, and S. Tretyakov, “Artificial magnetic materials based on the new magnetic particle: Metasolenoid,” *Prog. Electromagn. Res.*, vol. 54, pp. 61–81, 2005.
- [119] E. Shamonina, “Slow waves in magnetic metamaterials: history, fundamentals and applications,” *Phys. Stat. Sol. (b)*, vol. 245, no. 8, pp. 1471–1482, 2008.
- [120] R. A. Shelby, D. R. Smith, S. C. Nemat-Nasser, and S. Schultz, “Microwave transmission through a two-dimensional, isotropic, left-handed metamaterial,” *Appl. Phys. Lett.*, vol. 78, pp. 489–491, 2001.
- [121] K. Aydin, K. Guven, M. Kafesaki, L. Zhang, C. M. Soukoulis, and E. Ozbay, “Experimental observation of true left-handed transmission peaks in metamaterials,” *Opt. Lett.*, vol. 29, no. 22, pp. 2623–2625, 2004.
- [122] K. Aydin, K. Guven, C. M. Soukoulis, and E. Ozbay, “Observation of negative refraction and negative phase velocity in left-handed metamaterials,” *Appl. Phys. Lett.*, vol. 86, p. 124102, 2005.
- [123] M. Bayindir, K. Aydin, E. Ozbay, P. Markoš, and C. M. Soukoulis, “Transmission properties of composite metamaterials in free space,” *Appl. Phys. Lett.*, vol. 81, no. 1, pp. 120–122, 2002.
- [124] E. Ozbay, K. Aydin, E. Cubukcu, and M. Bayindir, “Transmission and reflection properties of composite double negative metamaterials in free space,” *IEEE Trans. Antennas Propag.*, vol. 51, no. 10, pp. 2592–2595, 2003.
- [125] T. Koschny, M. Kafesaki, E. N. Economou, and C. M. Soukoulis, “Effective medium theory of left-handed materials,” *Phys. Rev. Lett.*, vol. 93, no. 10, p. 107402, 2004.
- [126] N. Katsarakis, T. Koschny, M. Kafesaki, E. N. Economou, E. Ozbay, and C. M. Soukoulis, “Left- and right-handed transmission peaks near the magnetic resonance frequency in composite metamaterials,” *Phys. Rev. B*, vol. 70, p. 201101(R), 2004.
- [127] N. Katsarakis, T. Koschny, M. Kafesaki, E. N. Economou, and C. M. Soukoulis, “Electric coupling to the magnetic resonance of split ring resonators,” *Appl. Phys. Lett.*, vol. 84, no. 15, pp. 2943–2945, 2004.
- [128] N. Katsarakis, G. Konstantinidis, A. Kostopoulos, R. S. Penciu, T. F. Gundogdu, M. Kafesaki, and E. N. Economou, “Magnetic response of split-ring resonators in the far-infrared frequency regime,” *Opt. Lett.*, vol. 30, no. 11, pp. 1348–1350, 2005.
- [129] R. W. Ziolkowski, “Design, fabrication, and testing of double negative metamaterials,” *IEEE Trans. Antennas Propag.*, vol. 51, no. 7, pp. 1516–1529, 2003.

- [130] S. O'Brien, D. McPeake, S. A. Ramakrishna, and J. B. Pendry, "Near-infrared photonic band gaps and nonlinear effects in negative magnetic materials," *Phys. Rev. B*, vol. 69, p. 241101(R), 2004.
- [131] R. S. Penciu, K. Aydin, M. Kafesaki, T. Koschny, E. Ozbay, N. Economou, and C. M. Soukoulis, "Multi-gap individual and coupled split-ring resonator structures," *Opt. Express*, vol. 16, no. 22, pp. 18 131–18 144, 2008.
- [132] G. M. Rebeiz, *RF MEMS Theory, Design, and Technology*. NJ, USA: John Wiley & Sons, Hoboken, 2003.
- [133] D.-H. Kwon, D. H. Werner, A. V. Kildishev, and V. M. Schalev, "Near-infrared materials with dual-band negative-index characteristics," *Opt. Express*, vol. 15, no. 4, pp. 1647–1652, 2007.
- [134] Y. Yuan, C. Bingham, T. Tyler, S. Palit, T. H. Hand, W. J. Padilla, D. R. Smith, N. M. Jokerst, and S. A. Cummer, "Dual-band planar electric metamaterial in the terahertz regime," *Opt. Express*, vol. 16, no. 13, pp. 9746–9752, 2008.
- [135] A. B. Kaul, E. W. Wong, L. Epp, and B. D. Hunt, "Electromechanical carbon nanotube switches for high-frequency applications," *Nano Lett.*, vol. 6, no. 5, pp. 942–947, 2006.
- [136] K. Topalli, O. A. Civi, S. Demir, S. Koc, and T. Akin, "A monolithic phased array using 3-bit DMTL RF MEMS phase shifters," *IEEE Trans. Microw. Theory Tech.*, vol. 56, no. 2, pp. 270–277, 2008.
- [137] J. Wang, S. Qu, J. Zhang, H. Ma, Y. Yang, C. Gu, and X. Wu, "A tunable left-handed metamaterial based on modified broad-side coupled split-ring resonators," *Prog. Electromagn. Res. Lett.*, vol. 6, pp. 35–45, 2009.
- [138] D. A. Powell, M. Lapine, M. V. Gurkunov, I. V. Shadrivov, and Y. S. Kivshar, "Metamaterial tuning by manipulation of near-field interaction," *Phys. Rev. B*, vol. 82, p. 155128, 2010.
- [139] M. Lapine, D. Powell, M. Gurkunov, I. Shadrivov, R. Marques, and Y. Kivshar, "Structural tunability in metamaterials," *Appl. Phys. Lett.*, vol. 95, p. 084105, 2009.
- [140] H.-T. Chen, W. J. Padilla, J. M. O. Zide, A. C. Gossard, A. J. Taylor, and R. D. Averitt, "Active metamaterial devices," *Nature*, vol. 444, pp. 597–600, 2006.
- [141] H. O. Moser, J. A. Kong, L. K. Jian, H. S. Chen, G. Liu, M. Bahou, S. M. P. Kalaiselvi, S. M. Maniam, X. X. Cheng, B. I. Wu, P. D. Gu, A. Chen, S. P. Heussler, S. B. Mahmood, and L. Wen, "Free-standing THz electromagnetic metamaterials," *Opt. Express*, vol. 16, pp. 13 773–13 780, 2008.
- [142] H. Tao, C. M. Bingham, A. C. Strikwerda, D. Pilon, D. Shrekenhamer, N. I. Landy, K. Fan, X. Zhang, W. J. Padilla, and R. D. Averitt, "Highly flexible wide angle of incidence terahertz metamaterial absorber: Design, fabrication and characterization," *Phys. Rev. B*, vol. 78, p. 241103(R), 2008.
- [143] H. Tao, N. I. Landy, C. M. Bingham, X. Zhang, R. D. Averitt, and W. J. Padilla, "A metamaterial absorber for the terahertz regime: Design, fabrication and characterization," *Opt. Express*, vol. 16, pp. 7181–7188, 2008.

- [144] H.-T. Chen, W. J. Padilla, M. J. Cich, A. K. Azad, R. D. Averitt, and A. J. Taylor, "A metamaterial solid-state terahertz phase modulator," *Nat. Photonics*, vol. 3, pp. 148–151, 2009.
- [145] X. Liu, S. MacNaughton, D. B. Shrekenhamer, H. Tao, S. Selvarash, A. Totachawattana, R. D. Averitt, M. R. Dokmeci, S. Sonkusale, and W. J. Padilla, "Metamaterials on parylene thin film substrates: Design, fabrication and characterization at terahertz frequency," *Appl. Phys. Lett.*, vol. 96, p. 011906, 2010.
- [146] T. M. Grzegorzczuk, X. Chen, J. Pacheco, J. Chen, B.-I. Wu, and J. A. Kong, "Reflection coefficients and Goos-Hanchen shifts in anisotropic and bianisotropic left-handed metamaterials," *Prog. Electromagn. Res.*, vol. 51, pp. 83–113, 2005.
- [147] T. Koschny, P. Markos, D. R. Smith, and C. M. Soukoulis, "Resonant and antiresonant frequency dependence of the effective parameters of metamaterials," *Phys. Rev. E*, vol. 68, p. 065602(R), 2003.
- [148] D. R. Smith and J. B. Pendry, "Homogenization of metamaterials by field averaging (invited paper)," *J. Opt. Soc. Am. B*, vol. 23, no. 3, pp. 391–403, 2006.
- [149] A. Ishimaru, S. Jaruwatanadilok, and Y. Kuga, "Generalized surface plasmon resonance sensors using metamaterials and negative index materials," *Prog. Electromagn. Res.*, vol. 51, pp. 139–152, 2005.
- [150] A. Arbabi, A. Rohani, D. Saeedkia, and S. Safavi-Naeini, "A terahertz plasmonic metamaterial structure for near-field sensing applications," in *33rd International Conference on Infrared, Millimeter and Terahertz Waves (IRMMW-THz 2008)*, 2008, pp. 1–2.
- [151] R. Melik, E. Unal, N. Perkgoz, B. Santoni, D. Kamstock, C. Puttlitz, and H. Demir, "Nested metamaterials for wireless strain sensing," *IEEE J. Sel. Top. Quantum Electron.*, vol. 16, no. 2, pp. 450–458, 2010.
- [152] X.-j. He, Y. Wang, J.-m. Wang, and T.-l. Gui, "Thin-film sensor based tip-shaped split ring resonator metamaterial for microwave application," *Microsystem Technologies*, vol. 16, pp. 1735–1739, 2010.

VITA

PERSONAL INFORMATION

Surname, Name: Ekmekçi, Evren

Nationality: Turkish (TC)

Date and Place of Birth: 15 November 1980 , Ankara

Marital Status: Married

email: eekmekci@metu.edu.tr, evrenmekci@gmail.com

EDUCATION

Degree	Institution	Year of Graduation
BS	Süleyman Demirel University Electronics and Communication Eng.	2002
High School	İzmir Atatürk Lisesi, İzmir	1998

WORK EXPERIENCE

Year	Place	Enrollment
2002-present	METU Electrical and Electronics Engineering	Research Assistant
2009-2010	Boston University Physics Department Multifunctional Materials Laboratory	Visiting Researcher
2008-2009	ASELSAN, Behavioral Modeling of Asymmetrical IMD Distribution in Power Amplifiers	Researcher

PUBLICATIONS

International Refereed Journal Papers

1. **E. Ekmekci**, G. Turhan-Sayan, "Single Loop Resonator: Dual-band magnetic metamaterial structure," *Electronics Letters*, vol. 46, no. 5. 324-325, 2010.
2. **E. Ekmekci**, K. Topalli, T. Akin, G. Turhan-Sayan, "A Tunable Multi-Band Metamaterial Design Using Micro-Split SRR Structures," *Optics Express*, vol. 17, no. 18, 16046-16058, 2009.
3. **E. Ekmekci**, G. Turhan-Sayan, "Comparative Investigation of Resonance Characteristics and Electrical Size of The Double-Sided SRR, BC-SRR and Conventional SRR Type Metamaterials for Varying Substrate Parameters," *Progress In Electromagnetics Research B*, vol. 12, 35-62, 2009.

Pre-prints

1. **E. Ekmekci**, A. C. Strikwerda, K. Fan, X. Zhang, G. Turhan-Sayan, R. D. Averitt, "Frequency tunable metamaterials using broadside-coupled split ring resonators," arXiv: 1008.2195v1, 2010.

International Refereed Conference Papers

1. O. Turkmen, **E. Ekmekci**, G. Turhan-Sayan, "A New Multi-ring SRR Type Metamaterial Design with Multiple Magnetic Resonances," *Progress in Electromagnetic Research Symposium*, March 2011, Marrakesh, Morocco. (*accepted*)
2. **E. Ekmekci**, G. Turhan-Sayan, "Use of SRR-Based Super-Cells to Obtain Multiple Resonances and Broader Frequency Bands with Negative Effective Permeability," *IEEE AP-S International Symposium on Antennas and Propagation*, July 2010, Toronto, ON, Canada.
3. **E. Ekmekci**, R. D. Averitt, G. Turhan-Sayan, "Effects of Substrate Parameters on the Resonance Frequency of Double-Sided SRR Structures Under Two Different Excitations," *Progress in Electromagnetic Research Symposium*, July 2010, Cambridge, MA, USA.

4. T. T. Katilmis, **E. Ekmekci**, G. Turhan-Sayan, "Unsupervised Electromagnetic Target Classification by Self-Organizing Map Type Clustering," Progress in Electromagnetic Research Symposium, July 2010, Cambridge, MA, USA.
5. P. Yasar-Orten, **E. Ekmekci**, G. Turhan-Sayan, "Equivalent Circuit Models for Split-Ring Resonator Arrays," Progress in Electromagnetic Research Symposium, July 2010, Cambridge, MA, USA.
6. **E. Ekmekci**, G. Turhan-Sayan, "A Novel Dual-band Metamaterial Structure," Progress in Electromagnetic Research Symposium, August 2009, Moscow, Russia.
7. **E. Ekmekci**, K. Topalli, T. Akin, G. Turhan-Sayan, "Effects of Array Dimensions on the Resonance Characteristics of SRR Type Metamaterial Arrays with Small Sizes: Simulations and Experiments," Progress in Electromagnetic Research Symposium, August 2009, Moscow, Russia.
8. **E. Ekmekci**, K. Topalli, T. Akin, G. Turhan-Sayan, "A Feasibility Study for Tunable Metamaterial Design Using Multi-Split SRR Structures and RF MEMS Switching," IEEE International Symposium on Antennas and Propagation, June 2009, Charleston, SC., USA.
9. **E. Ekmekci**, G. Turhan-Sayan, "Reducing the Electrical Size of Magnetic Metamaterial Resonators by Geometrical Modifications: A Comparative Study for Single-Sided and Double-Sided Multiple SRR, Spiral and U-Spiral Resonators" IEEE International Symposium on Antennas and Propagation, July 2008, San Diego, USA.
10. M. Secmen, **E. Ekmekci**, G. Turhan-Sayan, "A Resonance Region Method for Recognition of Multiple Targets Using the MUSIC Algorithm and a Time Correlation Technique," IEEE International Symposium on Antennas and Propagation, July 2008, San Diego, USA.
11. **E. Ekmekci**, G. Turhan-Sayan, "Sensitivity of the Resonance Characteristics of SRR and DSRR (Double-Sided SRR) Type Metamaterials to the Changes in Substrate Parameters and the Usefulness of DSRR Structure for Reduced Electrical Size", Progress in Electromagnetic Research Symposium, pp. 598-602, July 2008, Cambridge, USA.
12. **E. Ekmekci**, G. Turhan-Sayan, "Investigation of Permittivity and Permeability for a Novel V-Shaped Metamaterial Using Simulated S-Parameters," 5th International Con-

ference on Electrical and Electronics Engineering, pp. 251-254, December 2007, Bursa, Turkey.

13. G. Turhan-Sayan, **E. Ekmekci**, "Target Pole Extraction from Transient Scattered Electromagnetic Data Using the Page and Wigner Distributions," Mediterranean Microwave Symposium 2006, pp. 129-132, September 2006, Genoa, Italy.

National Refereed Conference Papers (In Turkish)

1. **E. Ekmekçi**, K. Topallı, T. Akın, G. Turhan-Sayan, "Ayrık Halkalı Rezonatörlerden Oluşan Metamateryal Dizi Yapılarının Deneysel Olarak İncelenmesi," IEEE 17. Sinyal İşleme ve İletişim Uygulamaları Kurultayı, April 2009, Antalya, Turkey.
2. **E. Ekmekçi**, K. Topallı, T. Akın, G. Turhan-Sayan, "RF-MEMS Anahtarlama Tekniği ile AHR Tipi Metamalzemelerde Manyetik Rezonans Frekansının Adaptif Biçimde Ayarlanması," URSI-Türkiye 2008 4. Bilimsel Kongresi, pp. 106-109, October 2008, Antalya, Turkey.
3. **E. Ekmekçi**, G. Turhan-Sayan, "Çift Taraflı Ayrık Halkalı Rezonatör Yapısının Metamateryal Sensör Uygulamaları: Kuram ve Benzetim," URSI-Türkiye 2008 4. Bilimsel Kongresi, pp. 62-65, October 2008, Antalya, Turkey.
4. **E. Ekmekçi**, G. Turhan-Sayan, "V-Şekilli Rezonatör ve İletken Çubuklar Kullanarak Oluşturulan Sol-Elli Yapının Benzetimi, Etkin Ortam Parametrelerinin Çıkartılması ve Rezonans Frekansının Kaydırılması," Elektrik Elektronik Bilgisayar Biyomedikal Mühendisliği 12. Ulusal Kongre ve Fuarı, November 2007, Eskişehir, Turkey.
5. **E. Ekmekçi**, G. Turhan-Sayan, "Çift Taraflı Yapı ile Ayrık Halkalı Rezonatörün Rezonans Frekansının Düşürülmesi," 15. Yıl Mühendislik-Mimarlık Kongresi, Vol. 2, pp. 36-40, November 2007, Isparta, Turkey.
6. **E. Ekmekçi**, G. Turhan-Sayan, "V-Şekilli Yapılarla Yeni Bir Manyetik Rezonatör Uygulaması ve Simülasyonu," IEEE 15. Sinyal İşleme ve İletişim Uygulamaları Kurultayı, June 2007, Eskişehir, Turkey.
7. M. Seçmen, **E. Ekmekçi**, G. Turhan-Sayan, "Kaynaştırılmış MUSIC Tayf Matrisleri ile Elektromanyetik Hedef Tanıma Yönteminin Eksik Frekans Verilerine Uygulanması

ve Performans Analizi," IEEE 15. Sinyal İşleme ve İletişim Uygulamaları Kurultayı, June 2007, Eskişehir, Turkey.

8. G. Turhan-Sayan, **E. Ekmekçi**, "Geç-zamanlı Elektromanyetik Saçınım Verilerinden Page ve Wigner Dağılımları Kullanarak Hedef Sistem Kutuplarının Çıkarımı," URSI-Türkiye 2006 3. Bilimsel Kongresi, pp.61-63, September 2006, Ankara, Turkey.